

Old Dominion University

ODU Digital Commons

---

Computational Modeling & Simulation  
Engineering Theses & Dissertations

Computational Modeling & Simulation  
Engineering

---

Spring 2017

# Development of an Atlas-Based Segmentation of Cranial Nerves Using Shape-Aware Discrete Deformable Models for Neurosurgical Planning and Simulation

Sharmin Sultana  
*Old Dominion University*

Follow this and additional works at: [https://digitalcommons.odu.edu/msve\\_etds](https://digitalcommons.odu.edu/msve_etds)



Part of the [Bioelectrical and Neuroengineering Commons](#)

---

## Recommended Citation

Sultana, Sharmin. "Development of an Atlas-Based Segmentation of Cranial Nerves Using Shape-Aware Discrete Deformable Models for Neurosurgical Planning and Simulation" (2017). Doctor of Philosophy (PhD), Dissertation, Computational Modeling & Simulation Engineering, Old Dominion University, DOI: 10.25777/m30g-bw21  
[https://digitalcommons.odu.edu/msve\\_etds/6](https://digitalcommons.odu.edu/msve_etds/6)

This Dissertation is brought to you for free and open access by the Computational Modeling & Simulation Engineering at ODU Digital Commons. It has been accepted for inclusion in Computational Modeling & Simulation Engineering Theses & Dissertations by an authorized administrator of ODU Digital Commons. For more information, please contact [digitalcommons@odu.edu](mailto:digitalcommons@odu.edu).

**DEVELOPMENT OF AN ATLAS-BASED SEGMENTATION OF CRANIAL NERVES  
USING SHAPE-AWARE DISCRETE DEFORMABLE MODELS FOR  
NEUROSURGICAL PLANNING AND SIMULATION**

by

Sharmin Sultana  
B.S. December 2007, University of Dhaka  
M.S. May 2009, University of Dhaka

A Dissertation Submitted to the Faculty of  
Old Dominion University in Partial Fulfillment of the  
Requirements for the Degree of

DOCTOR OF PHILOSOPHY  
MODELING AND SIMULATION

OLD DOMINION UNIVERSITY  
May 2017

Approved by:

Michel A. Audette (Director)

Rick Mckenzie (Member)

Yuzhong Shen (Member)

Jiang Li (Member)

Benjamin Gilles (Member)

## ABSTRACT

### DEVELOPMENT OF AN ATLAS-BASED SEGMENTATION OF CRANIAL NERVES USING SHAPE-AWARE DISCRETE DEFORMABLE MODELS FOR NEUROSURGICAL PLANNING AND SIMULATION

Sharmin Sultana

Old Dominion University, 2017

Director: Dr. Michel A. Audette

Twelve pairs of cranial nerves arise from the brain or brainstem and control our sensory functions such as vision, hearing, smell and taste as well as several motor functions to the head and neck including facial expressions and eye movement. Often, these cranial nerves are difficult to detect in MRI data, and thus represent problems in neurosurgery planning and simulation, due to their thin anatomical structure, in the face of low imaging resolution as well as image artifacts. As a result, they may be at risk in neurosurgical procedures around the skull base, which might have dire consequences such as the loss of eyesight or hearing and facial paralysis. Consequently, it is of great importance to clearly delineate cranial nerves in medical images for avoidance in the planning of neurosurgical procedures and for targeting in the treatment of cranial nerve disorders. In this research, we propose to develop a digital atlas methodology that will be used to segment the cranial nerves from patient image data. The atlas will be created from high-resolution MRI data based on a discrete deformable contour model called *1-Simplex mesh*. Each of the cranial nerves will be modeled using its centerline and radius information where the centerline is estimated in a semi-automatic approach by finding a shortest path between two user-defined end points. The cranial nerve atlas is then made more robust by integrating a Statistical Shape Model so that the atlas can identify and segment nerves from images characterized by artifacts or low resolution. To the best of our knowledge, no such digital atlas methodology exists for segmenting nerves cranial nerves from MRI data. Therefore, our proposed system has important benefits to the neurosurgical community.

Copyright, 2017, by Sharmin Sultana, All Rights Reserved.

## ACKNOWLEDGMENTS

First, I would like to thank GOD almighty for the wisdom he bestowed upon me, the strength, patience and good health to finish my doctoral dissertation.

I would like to express my sincere gratitude to my advisor Dr. Michel Audette for his continuous support, invaluable advice and guidance throughout my PhD study. Besides my advisor, I would like to thank the rest of my dissertation committee members Dr. Benjamin Gilles, Dr. Rick Mckenzie, Dr. Yuzhong Shen and Dr. Jiang Li for their time, patience and valuable opinion.

I would like to acknowledge my friends and fellow lab mates for their encouragement and support. Thanks to my friend and colleague Tanweer for his endless patience in proof-reading my publications and dissertation manuscript.

Last but not the least, I would like to thank my family: my beloved parents and sisters for supporting me spiritually despite the distance. Finally, this work would never have been possible without the unconditional love, support and trust of my husband Mozaffor who is always by my side whenever I needed.

## TABLE OF CONTENTS

	Page
LIST OF TABLES.....	vii
LIST OF FIGURES.....	viii
Chapter	
1. INTRODUCTION .....	1
1.1 Problem.....	4
1.2 Proposed Solution.....	7
1.3 Anticipated Contributions.....	9
1.4 Deformable Representation of Cranial Nerves.....	11
1.5 Organization.....	11
2. ANATOMY AND IMAGING .....	12
2.1 Anatomy of Cranial Nerves .....	12
2.2 Image Acquisition of the Cranial Nerves .....	17
2.3 Conclusion .....	21
3. BACKGROUND .....	23
3.1 Deformable Models in Segmentation .....	23
3.2 Segmentation of Curvilinear Structures.....	31
3.3 Nerve Segmentation.....	38
3.4 Survey of Statistical Shape Models .....	44
3.5 Shape Representation and Model Construction.....	46
3.6 Registration in Medical Imaging .....	50
3.7 Conclusion .....	56
4. CENTERLINE EXTRACTION AND SURFACE MODELING .....	57
4.1 Centerline Identification .....	58
4.2 Nerve Surface Generation.....	64
4.3 Results.....	67
4.4 Validation.....	78
4.5 Conclusion .....	88
5. SHAPE-AWARE DEFORMABLE CONTOUR ATLAS.....	90
5.1 Statistical Shape Models .....	90
5.2 Shape Correspondence and Model Construction.....	92
5.3 Computation of Strong Shape Priors .....	96
5.4 Segmentation using SSM.....	98
5.5 Evaluation of SSM.....	102
5.6 Validation using Synthetic Data .....	103

Chapter	Page
5.7 Validation Using Patient Data .....	111
5.8 Conclusion .....	138
6. CONCLUSIONS AND FUTURE WORKS .....	140
6.1 Discussion .....	140
6.2 Limitations and Future Works .....	141
REFERENCES .....	144
VITA .....	156

## LIST OF TABLES

Table	Page
1. Cranial nerves, origins, functions and openings .....	14
2. Different patterns in 3-D image based on eigenvalues of Hessian. ....	33
3. Quantitative validation of the medial axis extraction method for synthetic datasets.....	78
4. Quantitative validation of the medial axis extraction method for the MRI dataset .....	80
5. Quantitative validation of boundary surfaces of cranial nerves.....	88
6. Quantitative validation of Segmentation using helix SSM.....	109
7. Generality and Specificity error for CNV to CNVIII .....	120
8. Specificity and Generality errors of lower cranial nerves. ....	128
9. Segmentation results without shape information of fully visible dataset with respect to the ground truth .....	130
10. Segmentation results using shape-based atlas of fully visible dataset.....	132
11. Segmentation results of the partially visible dataset.....	133



## LIST OF FIGURES

Figure	Page
1. Twelve pair cranial nerves and their motor and sensory connectivity with different body components..	3
2. Vulnerability of cranial nerves in neurosurgical procedures.	3
3. Electrophysiological monitoring of CN IX during tumor surgery..	6
4. The Olfactory (I) and Optic (II) Nerve.	13
5. Depiction of brainstem, along with nerves II to XII [33].	16
6. Cranial Openings..	17
7. Spin-echo pulse sequence..	19
8. Simplified classification of deformable models	25
9. Simplex Meshes..	28
10. At locations centered within tubular structures the eigenvector ( $v_1$ ) corresponding to the smallest eigenvalue ( $\lambda_1$ ) of the Hessian matrix is along the vessel direction and the other eigenvectors $v_2$ and $v_3$ span the cross-sectional plane..	33
11. Metrication error.	36
12. MRA of a brain slice showing blood vessels and veins.....	39
13. Diffusion Tensor representation	42
14. Centerline Extraction Pipeline.	58
15. 1-Simplex geometry.....	61
16. A step by step segmentation process of a synthetic nerve surface.	65
17. 2-Simplex mesh surface segmentation.....	67
18. Results of arc-shaped tubular digital phantom.....	69
19. Results of sinusoidal digital phantom..	70
20. 3D helix-shaped digital tubular phantom results.	71

Figure	Page
21. Centerlines of cranial nerves (CNIII to CNVI) from MR patient data. ....	72
22. Centerlines of cranial nerves (CNVII to CNXII) from MR patient data. ....	73
23. 3D segmentation of cranial nerves III to V .....	75
24. 3D segmentation of cranial nerves III to VI.. ....	76
25. 3D segmentation of cranial nerves VII to XII. ....	77
26. Visualization of CNIII w.r.t. the ground truth. ....	79
27. Validation of oculomotor nerves (CNIII).. ....	82
28. Validation of abducens nerves (CNV).. ....	83
29. Validation of trigeminal nerves (CN VI).. ....	84
30. Validation of vestibulocochlear nerves (CN VIII).. ....	85
31. Validation of vagus nerves (CN X).. ....	86
32. Validation of accessory nerves (CNXI). ....	87
33. Point Distribution on a sphere using particle positing.. ....	95
34. Flow chart of SSM construction and SSM-based Segmentation. ....	100
35. Shape Alignment and Shape Correspondence of the Helix model. ....	104
36. Modes of variation of the helix SSM. ....	106
37. Compactness, Specificity and Generality of the helix SSM. ....	107
38. Volume rendering of the Synthetic images. ....	109
39. Centerline Segmentation with and without shape priors ....	110
40. Depiction of the Housdorff Distance (HD) for the corrupted volume. ....	111
41. SSM of left and right CNIII.. ....	114
42. SSM of the combined CNIII; SSM of the combined CNIII.. ....	115
43. Modes of Variation of Combined CNIII. ....	116

Figure	Page
44. SSM of CNIV. ....	117
45. Modes of Variation of CNIV. ....	117
46. SSM of CNV.....	118
47. SSM of CNVI. ....	119
48. Modes of Variation of CNV (a) and CNVI (b).....	120
49. SSM of CNVII. ....	121
50. SSM of CNVIII.....	122
51. Modes of Variation of CNVII.....	123
52. Modes of Variation of CNVIII. ....	123
53. SSM of CNIX. ....	124
54. Modes of Variation of CNIX. ....	125
55. SSM of CNX.....	125
56. Modes of Variation of CNX. ....	126
57. SSM of CNXI. ....	126
58. Modes of Variation CNXI. ....	127
59. Modes of Variation of CNX. ....	127
60. SSM of CNXII. ....	127
61. Modes of Variation of CNXII.....	128
62. Centerline computation of CNXII where vesselness filtering fails to capture tubularity information properly. ....	131
63. Graphical comparison of segmentation algorithm with and without SSM using partially visible dataset.....	134
64. Centerline segmentation of CNIV from the corrupted dataset. ....	135
65. Centerline segmentation of CNX from the noisy dataset .....	136

Figure	Page
66. Segmentation of CNXII from noisy data. ....	137

## CHAPTER 1

### INTRODUCTION

Twelve pairs of cranial nerves arise from the brain or brainstem, exit through the cranial foramina and innervate various parts of the head and neck, as shown in Fig. 1. These cranial nerves control our sensory functions such as vision, hearing, smell and taste as well as several motor functions to the head and neck including facial expressions, eye movement, etc. These nerves are often at risk in neurosurgical procedures as depicted in Fig. 2. During neurosurgery, a single incorrect and injurious maneuver to a cranial nerve can result in a lifelong penalty such as the loss of eyesight, hearing or facial paralysis<sup>1</sup>.

Cancer is the second leading cause of death in the US, after cardiovascular disease, with 585,720 deaths in 2014; there were 1,665,540 new cancer diagnoses in the US that year [1]. Metastatic brain tumors occur in about 30% of cancer patients [2]. Also, according to the Central Brain Tumor Registry of the US (CBTRUS), in 2015 the total number of incidents of all primary malignant and non-malignant brain and central nervous system tumors is 356,858, of which 117,023 were malignant [3]. Many of these cases occur at the base of the brain close to cranial nerves, which clearly are at risk of injury. Skull base surgery is performed to remove malignant and cancerous growths, as well as abnormalities on the underside of the brain. Growths and conditions those needs a skull base surgery includes pituitary tumors, meningiomas, trigeminal neuralgia, cerebral aneurysm etc.

Surgery around the skull base may lead to considerable risk of nerve injury and even mortality due to the close proximity of cranial nerves to complex blood vessel networks [4]. Nerve injury mechanisms includes traction, stretching, impingement and transection [5]. Therefore, it is of paramount importance to clearly delineate cranial nerves in Magnetic

---

<sup>1</sup> IEEE Transactions and Journals style is used in this thesis for formatting figures, tables, and references.

Resonance Imaging (MRI) for planning and patient-specific simulation of neurosurgical procedures, where these critical structures are at risk. This identification of cranial nerves in MRI data is complicated by their thin anatomical structure, especially those (such as nerve IV and XII) that are narrow in relation to imaging resolution. This situation is further exacerbated by image artifacts such as partial volume effects.

In this dissertation, we propose a method for patient-specific cranial nerve segmentation using a digital atlas of the cranial nerves. We anticipate that this cranial nerve model would benefit the following applications:

- **Model-guided neurosurgical avoidance of cranial nerves.** The model would help towards the identification and avoidance of cranial nerves in the skull base in pre-operative planning and intra-operative navigation, respectively.
- **Neurosurgical training simulation to prevent operative injury to cranial nerves.** This model would help to penalize surgical gestures deleterious to cranial nerves during simulation-based training.
- **Model guided neurosurgical targeting of cranial nerves.** The proposed cranial nerve atlas would help to detect a specific nerve as a surgical target for nerve stimulation in epilepsy treatment [6] and the decompression of a cranial nerve for neuralgia treatment [7], [8] and with suitable modification, targeting of nerve tumors such as schwannoma.

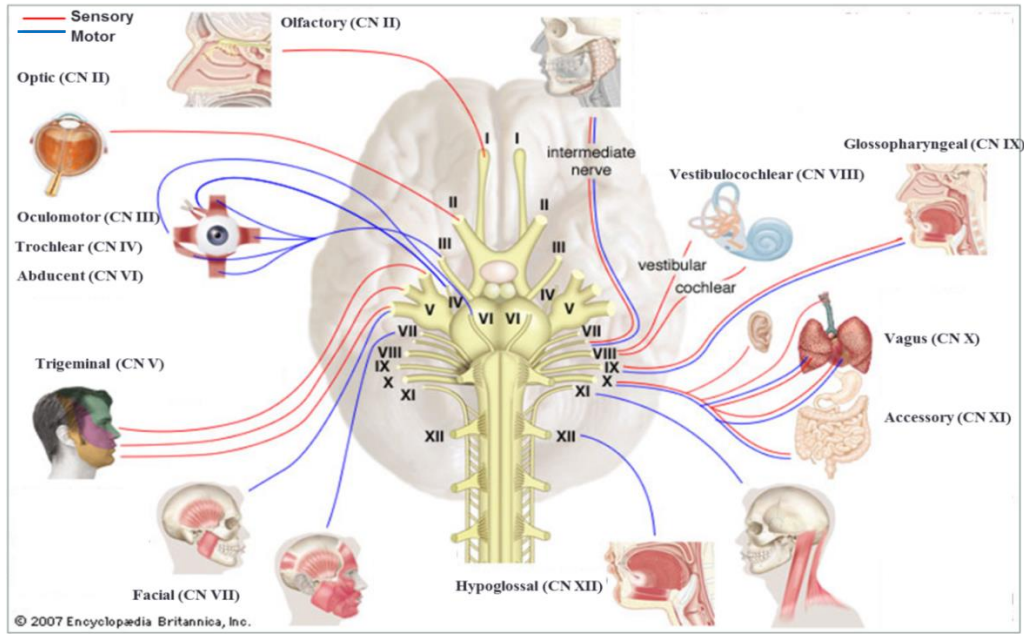


Fig. 1. Twelve pair cranial nerves and their motor and sensory connectivity with different body components. Blue lines transmit motor signals and red lines carry sensory signals [9].

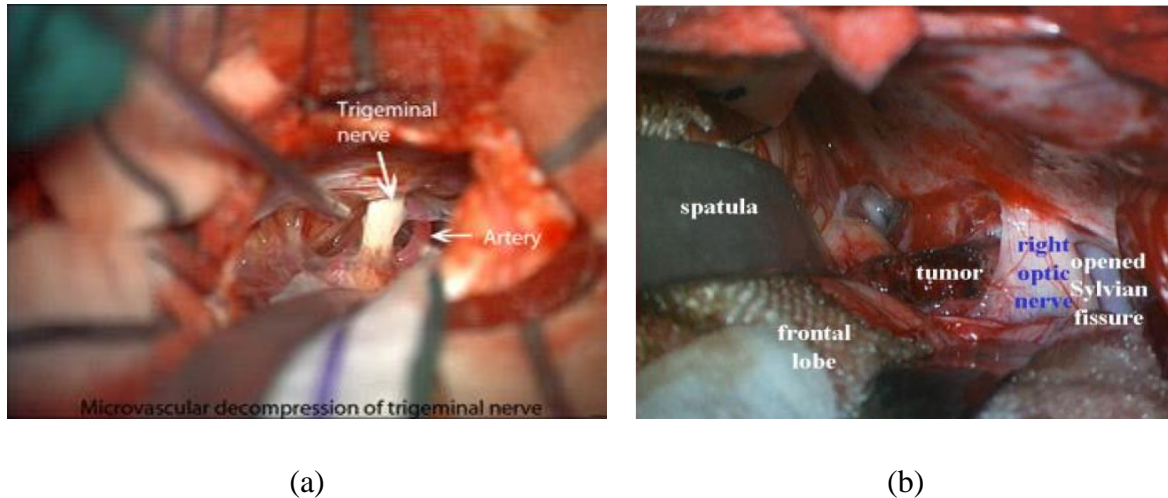


Fig. 2. Vulnerability of cranial nerves in neurosurgical procedures. (a) A view of an operating microscope showing micro-vascular decompression of trigeminal nerve (CNV)[10]. (b) A spatula exposes a deep-seated tumor near the right optic nerve; image courtesy of C. Trantakis, Division of Neurosurgery, University of Leipzig, Germany.

## 1.1 Problem

The importance of cranial nerve detection in neuro and ENT surgery is justified in two broad areas:

- Avoidance in surgery planning to prevent intra-operative damage to cranial nerves while targeting a tumor or arteriovenous malformation.
- Targeting of cranial nerves in the context of surgical treatment.

Iatrogenic nerve injury is defined as intra-operative damage to cranial nerves, which includes traction, stretching, impingement and transection of the nerve. Several factors contribute to a cranial nerve's susceptibility to trauma, such as the length and the course of the nerve and surrounding blood vessels. The course of the nerve, and in particular, its relationship with fixed and stiff structures such as the bone and dura, and its proximity to the planned surgical path, determine the vulnerability of each cranial nerve to trauma and the most vulnerable sites to injury [5]. Recently, Antoniadis et al. [11] performed a review of iatrogenic nerve injury from 1990 to 2012 involving 345 patients, and found that 25% of nerve lesions that required treatment were iatrogenic. They pointed out that cranial nerves are vulnerable because they are neither clearly exposed in the operative field nor are they recognized as nerves but mistaken as a blood vessel. Adachi et al. [12] reported about the risks and complications of surgery for skull base meningioma due to the involvement of cranial nerves and arteries, and proposed a scoring system to measure the relative risk involved in the surgery. Dubey et al. [13] performed a retrospective study of all posterior fossa surgeries from 1992 to 2002, involving over 500 patients, and found that the overall complication rate of the surgery is about 31.8% and the mortality rate is 2.6%. To avoid such complications, the authors recommended careful pre-operative planning and a thorough understanding of the operative cranial anatomy.



Cranial nerves also appear as surgical targets for the treatment of neuralgia<sup>2</sup> and epilepsy<sup>3</sup>. The most common treatment for neuralgia is microvascular decompression which is a surgical procedure that relieves abnormal compression of a cranial nerve [14]. Leal et al. [15] showed that the pre-operative determination of neurovascular features (such as conflicting nature, exact localization, direction and degree of compression) from MRI data could be of great importance to neurosurgeons performing microvascular decompression. They studied 100 patients with trigeminal neuralgia in the pre-operative stage by examining high-resolution 3D MR images, and concluded that neurovascular feature prediction from imaging increases the success rate of the decompression while helping the surgeons to decide the best surgical option. Vagus nerve stimulation (VNS) [6] is described as a valuable option in the therapeutic treatment for patients with refractory epilepsy. Apart from epilepsy and neuralgia, stimulation therapy for neuropathic pain may also require cranial nerve targeting [8] [16] [17] [18].

The current method for intra-operative cranial nerve monitoring during skull base surgery is done using electrophysiologic monitoring [19] [20] [21]. To monitor motor cranial nerves (such as trigeminal, facial, glossopharyngeal, spinal accessory, and hypoglossal nerves) during the surgical removal of tumors of the skull base, stimulodetection techniques are used as shown in Fig. 3. At the beginning of an operation, electrical stimulation is only used to identify the nerve structures. As the removal of the tumor progresses, the goal is to verify that a surgical injury to the nerve is avoided by looking for the absence of any changes in amplitude, morphology, and latency of motor responses.

---

<sup>2</sup> Neuralgia is a stabbing, burning, and often quite severe pain that occurs along a damaged nerve.

<sup>3</sup> Epilepsy is a neurological disorder in which the nerve cell activity in the brain is disturbed, causing a seizure during which the afflicted experiences abnormal behavior, symptoms and sensations, including loss of consciousness.

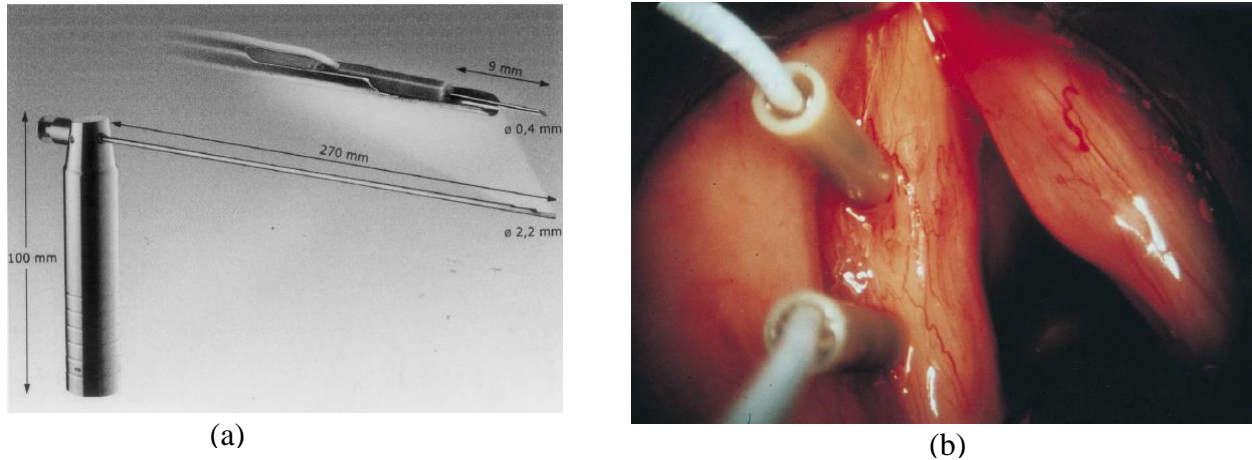


Fig. 3. Electrophysiological monitoring of CN IX during tumor surgery. (a) Special applicator used for placing a pair of needle electrodes. (b) Endoscopic view of the ‘true vocal cord’ with a pair of steel needle electrodes being unilaterally inserted. Reproduced from [19].

The necessity for cranial nerve identification has also been observed in neurosurgical simulators to accurately model the correct response to therapy. Recently, the neurosurgical simulation research center<sup>4</sup> of Montreal Neurological Institute developed a physically-based virtual reality neurosurgical simulator with haptic feedback, called NeuroTouch, for the training and assessment of technical skills during craniotomy-based procedures. Although this simulator can represent anatomical details of the human body as well as blood vessels in a realistic manner, it does not model the cranial nerves nor does it represent the skull base anatomy.

From both a surgical and a simulation point of view, our proposed cranial nerve model has potential in surgical planning and treatment by accurately and precisely segmenting cranial nerves in MR images.

To the best of our knowledge, *there exists no comparable clinically applicable method for identifying cranial nerves, particularly the finer ones, in routine  $T_2$ -weighted MR images.*

---

<sup>4</sup> <http://neurosims.mcgill.ca/>

Existing whole-brain segmentations of [23] and digital brain atlases of [24] have not attempted to segment cranial nerves, while the Surgical Planning Laboratory (SPL) atlas [25] only accounts for the larger cranial nerves. Nowinski et al. [26] constructed a 3D atlas of the cranial nerves with their nuclei correlated with their surface neuroanatomy, vasculature and magnetic resonance imaging which is based on their previously developed whole brain atlas of structures, vasculature and tracts [27]. This 3D geometric model has potential usefulness such as anatomy browsing, automatic student assessment and preparation of materials for education. Although this 3D atlas of cranial nerves might serve the purpose of medical research and education, it is a static model based on high-field (7T) images, and is not intended for patient-specific segmentation or surgical planning; it does not support inter-subject registration.

## 1.2 Proposed Solution

To address the absence of cranial nerve models in current brain modeling, we propose to develop a shape-based digital deformable atlas of cranial nerves which will be constructed from high-resolution  $T_2$ -weighted MRI data and a registration procedure of the proposed atlas to individual patient data (possibly from low-resolution MRI data) to perform patient-specific cranial nerve segmentation. The proposed system will model the cranial nerves using a centerline-based approach, which will then be made more robust by integrating a Statistical Shape Model. Once the atlas of the cranial nerves is constructed, medical image data will be segmented using a combined segmentation-registration approach.

Cranial nerves are tube-like structures, some of which have branchial arches outside the cranium forming tree-like structures such as the trigeminal, facial, glossopharyngeal, vagus and accessory nerves. However, the intracranial portions of cranial nerves that lie within the cranium

are assumed to have comparatively simpler contour shapes. We are interested in the intra-cranial (or cisternal) portion of the cranial nerves that are targeted during skull-base neurosurgery.

The first step of the proposed system is to represent cranial nerves using centerline and radius estimation. We will trace the centerlines of the cranial nerves by using a discrete deformable model called  $l$ -Simplex mesh. A  $k$ -Simplex mesh, introduced by Delingette [29], is a  $k+1$ -connected mesh used for active surface modeling which has the unique property of having a constant connectivity at each vertex. The 2-Simplex is a surface mesh where each vertex has 3 neighbors linked by edges; the 1-Simplex is a 2D or 3D contour where each vertex except end-points is connected to 2 neighbors. Our proposed segmentation approach will be a semi-automatic approach, where the user/expert defines a pair of start and end points for each of the cranial nerves; in a future version, these end and start points will be supplied through patient-fitted digital brainstem and cranial foramina models. Once these end points are defined, the rest of the process will be automatic. The first stage computes the shortest path between each of the start and end points using Fast Marching method [30, 31]. These shortest paths will act as the initial estimation of the centerlines of the cranial nerves, which are then deformed using internal and external forces to move towards the true medial axis of the nerves. The proposed system then computes 3D centerline curves, and at the same time, also estimates the radius of the nerve at regularly sampled points of the curve.

The following step is to segment the nerve surface boundary using the centerline and radius information. We have employed 2-Simplex mesh refinement to perform the surface segmentation.

An important feature of the proposed system is to endow the cranial nerve atlas with prior shape information by integrating Statistical Shape Models with the deformable 1-Simplex model

so that the atlas is capable of identifying and segmenting nerves from low-resolution images or in the presence of partial volume effects. The proposed system will compute statistical shape information from a population of training data set, which will be added in the form of a shape-enforcing energy functional to the deformable Simplex model's Newtonian formulation.

The final refinement of the proposed system will be to segment cranial nerves in the subject MRI by using the constructed shape-aware atlas. The proposed system will accomplish this by making use of an elastic deformable model registration, which is achieved by aligning the atlas with the target image (the image that needs to be segmented) by minimizing a similarity criteria (internal and external forces).

### **1.3 Anticipated Contributions**

Although there is an essential need for a deformable digital cranial nerve atlas in neurosurgery and treatment of cranial nerve disorders and tumors, to the best of our knowledge no research group has attempted to develop such a digital deformable contour atlas. In this research, we have developed a deformable digital cranial nerve atlas which will be able to segment the twelve pairs of cranial nerves from patient MRI data, although this work will emphasize the ten brainstem pairs. In addition, this research is the first to develop a minimally supervised Statistical Shape Model formulation for 3D contours. The following sections describe the contributions that are the foundation of this proposed system.

#### **1.3.1 Discrete Deformable Representation of Curvilinear Structures**

We will model each of the cranial nerves using a centerline-based method, which is a common approach for the segmentation of tubular shaped structures. But the representation of

the centerlines of tubular/curvilinear structures using a 1-Simplex mesh model is a new idea that will be implemented in this research. We will formulate new internal and external energy functions for the 1-Simplex based curve deformation.

### **1.3.2 Incorporation of a Statistical Shape Model with the Deformable Contour Atlas**

Cranial nerves are fine critical structures in the human brain. Some of the cranial nerves are much finer than others, in particular the trochlear nerve (CN IV) and the lower cranial nerves (CN IX to CN CXII). These cranial nerves cannot be seen very clearly even in high-resolution (3T) MR image. As a result, they are vulnerable to head injury or surgical injury which might result in the loss of motor functions, for example, limiting the ability to look down and outwards (CN IV malfunction) and the loss of taste from the back of the tongue (CN IX malfunction). To remedy such malfunctions of the cranial nerves, we wish to identify them from regular MRI data using our deformable atlas. To fulfil this aim, we will integrate a Statistical Shape Model to our deformable atlas so that we know, *a priori*, the average shape information and shape variation when we segment the low resolution image data. Although shape priors have been used in the literature for segmentation purposes, this framework has not yet been used with 3D contour models. We will formulate the shape prior as an energy functional, which will be described mathematically, which in turn leads to a minimization along with other components of the internal and external energy functions during the 3D contour deformation.

## **1.4 Deformable Representation of Cranial Nerves Conducive to Subject-Specific Registration**

Non-rigid registration is one of the prevalent techniques for aligning source and target images. We will be using a model-to-image registration technique to align our deformable nerve contour atlas with the target image. We will use an energy-oriented distance field as a similarity measure, which is minimized to perform the non-rigid registration during the nerve segmentation process.

## **1.5 Organization**

This manuscript is divided into the following chapters. Chapter 2 describes the anatomy of cranial nerves of the human brain as well as imaging techniques used for visualizing cranial nerves. Chapter 3 reviews the relevant literature on the following areas: deformable models (Section 3.1), curvilinear structure segmentation (Section 3.2), a review on nerve segmentation methods (Section 3.3), Statistical Shape Models (Section 3.4 and Section 3.5) and image registration methods (Section 3.6). Chapter 4 elaborately discusses our approach to centerline extraction and surface segmentation of nerves. Chapter 5 describes the construction of Statistical Shape Models of cranial nerves and the application of SSMs to nerve segmentation. Chapter 6 concludes the dissertation by discussing scopes, limitations and future work of our approach.

## CHAPTER 2

### ANATOMY AND IMAGING

In this chapter, we will present an anatomical description of all the twelve pairs of cranial nerve (Section 2.1). Then, Section 2.2 will describe some common MRI sequences that can be used to identify cranial nerves.

#### 2.1 Anatomy of Cranial Nerves

There are a total of 12 pairs of cranial nerves: 10 pairs that originate from the brainstem, which can be seen having the shape of a twenty-legged spider, and two more pairs that attach to the brain anteriorly and superiorly to the brainstem, as shown in Fig. 1. Depending on the impulses they carry, cranial nerves in the central nervous system can be classified as sensory (I, II, VIII), motor (II, IV, VI, XI, XII) or mixed (V, VII, IX,X) as summarized in Table 1. Each of them carries different signals related to the corresponding sensory or motor functions of our body. Sensory nerves are responsible for transmitting sensory impulses of vision, hearing, smell, taste and touch. Motor and mixed nerves are responsible for carrying signals for facial expressions, swallowing, speech, etc. Motor components of the cranial nerves transmit nerve impulses from the brain to the target muscles in the head and neck. Sensory components transmit nerve impulse from sensory organs to the brain. Except the olfactory (CN I) and the optic (CN II) nerves, all the other cranial nerves (III to IX) originate from the brainstem, travel through the perimesencephalic and basal cisterns, and then exit the intracranial compartment the neurovascular foramina (or cranial openings) of the skull base [5, 32].

The olfactory nerve is a collection of sensory nerve rootlets that extend down from the olfactory bulb and pass through the many openings of the cribriform plate in the ethmoid bone.



Receptor neurons of the olfactory nerves are located in the olfactory mucosa of the upper parts of the nasal cavity as shown in Fig. 4. (a). Each of the optic nerve originates from the bipolar cells of the corresponding retina and exits the back of the eye in the orbit through the optic canal. It enters the central nervous system at the optic chiasm (or crossing) where the nerve fiber becomes the optic tract just prior to entering the brain as shown in Fig. 4. (b). Most of the axons of the optic nerve terminate in the lateral geniculate nucleus (LGN) in the thalamus, from where information is relayed to the visual cortex.

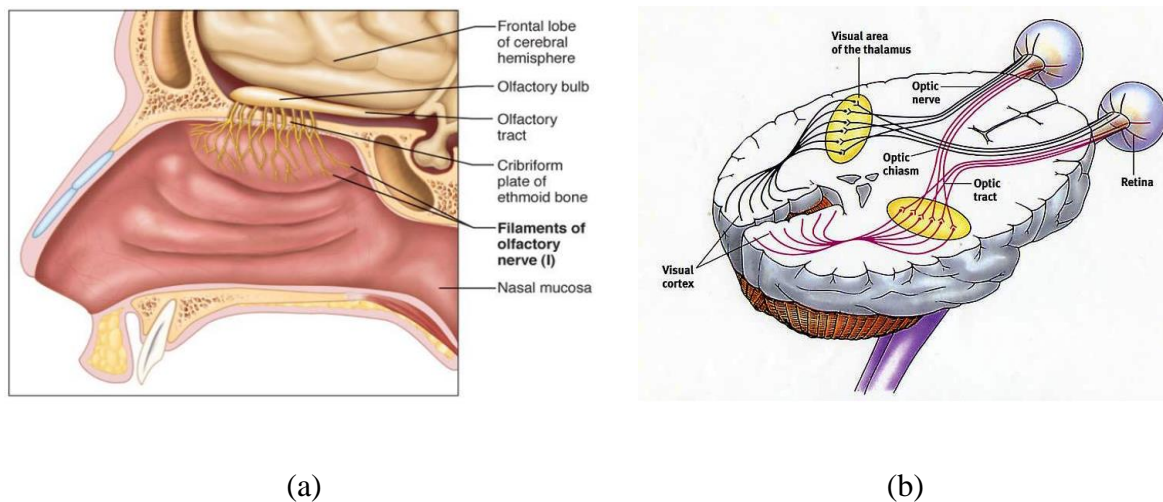


Fig. 4. The Olfactory (I) and Optic (II) Nerve. (a) View of the receptor neurons in the nasal cavity and olfactory bulb. Reproduced with the permission from [studyblue.com](http://studyblue.com). (b) Visual pathway from orbit including optic chiasm. Reproduced with the permission from [rhmpsychology.com](http://rhmpsychology.com).

Table 1. Cranial nerves, origins, functions and openings

Nerves	Types	Origin	Functions	Cranial Openings
Olfactory (I)	Sensory	Olfactory Bulb	Olfactory receptor for sense of smell	Foramina in cribriform plate (ethmoid)
Optic (II)	Sensory	Thalamus	Retina for sense of light	Optic Foreman (sphenoid)
Oculomotor (III)	Motor	Midbrain	Motor control of some eye muscles and eyelid	Superior orbital fissure
Trochlear (IV)	Motor	Midbrain	Motor control of Superior oblique muscle; Eye movement	Superior orbital fissure
Trigeminal (V)	Mixed	Pons	Sensory for head/neck, sinuses, meninges and external surface of tympanic membrane. Motor control for chewing - Muscles of mastication.	Superior orbital fissure
Abducens(VI)	Motor	Pons	Eye movement	Superior orbital fissure
Facial (VII)	Mixed	Pons	Sensory for ear and tympanic membrane. Taste anterior two third of tongue. Motor control for muscles of facial expression, salivation.	Internal auditory meatus
Acoustic/ Vestibulocochlear (VIII)	Sensory	Pons	Sense of hearing and Equilibrium (balance)	Internal auditory meatus
Glossopharyngeal (IX)	Mixed	Medulla Oblongata	Salivation, sensation of posterior one-third tongue and internal surface of tympanic membrane. Motor control for swallowing-muscles of Pharynx.	Jugular Foramen
Vagus (X)	Mixed	Medulla Oblongata	Sensation from the thorax, pharynx and abdominal. Motor control for pharynx, larynx, heart.	Jugular Foramen
Spinal Accessory (XI)	Motor	Medulla Oblongata	Motor impulses to the pharynx and shoulder. Movement of Trapezius and sternocleidomastoid muscles.	Jugular Foramen
Hypoglossal (XII)	Motor	Medulla Oblongata	Tongue muscles (swallowing and speech)	Hypoglossal canal

The brainstem is the area of the brain that lies between the deep structures of the cerebral hemispheres and the cervical spinal cord. It is divided into three sections: midbrain (or mesencephalon), pons (or metencephalon) and medulla oblongata (or myelencephalon) as depicted in Fig. 5. (a). Except the olfactory and optic nerves, all of the cranial nerve nuclei are located in the brainstem as shown in Fig. 5. (b). The midbrain is divided into the anterior and the posterior sections by the Aqueduct of Sylvius, which connects the third and fourth ventricles. Cranial nerves III and IV are connected to the midbrain. CN III supplies four out of the six extraocular muscles of the eye and the levator palpebrae superioris muscle of the upper eyelid, as well as provides the parasympathetic innervation of the constrictor pupillae and ciliary muscles. CN IV innervates the superior oblique muscle of the contralateral orbit.

The pons, coinciding with the middle of the brainstem, lies above the medulla oblongata and below the cerebellum and in the cavity of fourth ventricle. It is the point of origin of the four cranial nerves V, VI, VII and VIII. The nuclei of these cranial nerves relay information from the ear, face and teeth as well as emit signals that move the jaw, adjust facial expressions, and produce some eye movements.

The medulla oblongata, the lowest portion of the brainstem, contains the last four cranial nerves, namely the glossopharyngeal (IX), the vagus (X), the accessory (XI) and the glossopharyngeal (XII). The glossopharyngeal nerve consists of both efferent and afferent components, each of which has distinct functions. The efferent neurons of CN IX are responsible for the following activity: i) supplying impulses to the stylopharyngeus muscle involving the motion of the pharynx and larynx; ii) providing general sensory information from the skin of the external ear and internal surface of the tympanic membrane, upper pharynx; and iii) providing taste sensation from the posterior part of the tongue. Next, the vagus nerve (CN X) also have

several functions: i) supplying impulses to the voluntary muscles of the pharynx and most of the larynx and one extrinsic tongue muscle; ii) providing visceral sensory information from the larynx, esophagus, trachea, and abdominal and thoracic viscera; and iii) providing general sensory information from the outer and middle ear as well as the pharynx. Next, the accessory nerve (XI) has both a cranial and a spinal root, consisting of motor fibers. The cranial root innervates the muscles of the pharynx and larynx, while the spinal root innervates the trapezius and sternocleidomastoid muscles. Lastly, the hypoglossal nerve (XII) innervates muscles of the tongue for providing motor control of the three out of four extrinsic muscles (four pair of muscles that originate from bone and extend to the tongue); genioglossus, hyoglossus, styloglossus and the intrinsic muscles (four paired muscles that originate and insert within the tongue, running along its length).

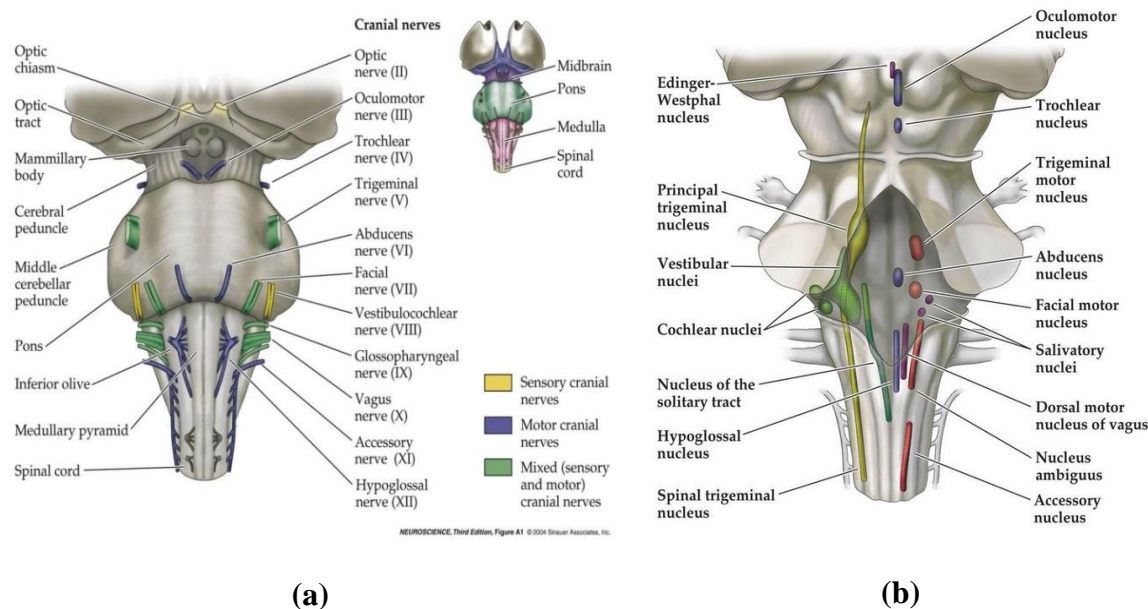


Fig. 5. Depiction of brainstem, along with nerves II to XII [33].

The cranial openings, also called cranial foramina, are located on the base of the skull to allow passage through the cranium for structures like cranial nerves, blood vessels as well as other structures of the CNS, as shown in Fig. 6. and summarized in Table 1. Therefore, in the long term, accounting for these openings is the key to determining the exit positions of the cranial nerves in a minimally supervised fashion.

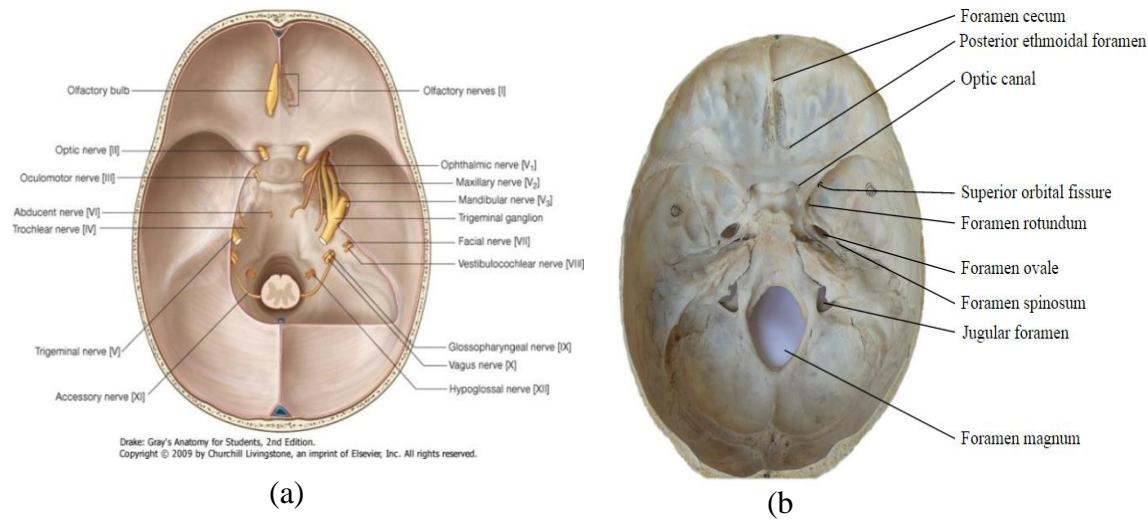


Fig. 6. Cranial Openings, (a) All the twelve pairs of cranial nerves exit through openings. (b) Cranium with labeled foramina [34].

## 2.2 Image Acquisition of Cranial Nerves

The ability of modern MRI techniques for visualizing detailed anatomy of the brainstem, basal cisterns and skull base has aided the evaluation of skull base neurosurgery. Generally, *MRI is the method of choice for imaging cranial nerves*. Although the larger nerves such as the optic and trigeminal nerves can be seen in routine MRI of the brain, smaller nerves and branches require high spatial resolution.

MRI uses the protons ( $H^+$ ) of water molecules which has a special magnetic property called nuclear spin. In a strong static magnetic field  $B_o$  in the  $z$ -direction, these spins align in either parallel or anti-parallel orientations with the direction of the magnetic field, creating a net magnetization vector. Magnetic resonance corresponds to the energetic interaction between spins, which precess at a characteristic Larmor frequency, and an electromagnetic radio frequency (RF) signal of the same frequency which can perturb the spinning proton. The RF sinusoid signal must be of that same Larmor frequency to induce a torque which causes spins to re-align in a direction other than the  $z$ -axis: the amount of flip angle with respect to the  $z$ -axis is determined by the duration of the RF pulse. A flip angle of 90 degrees results in a magnetization in the  $xy$ -plane, also known as transverse magnetization. When the RF signal is removed, the excited protons tend to return to their lower energy state through a process called relaxation. This relaxation process causes the emission of energy which is then received by RF coils and processed in a computer to produce MR images [35] [36] [37]. The resolution of MR images is dependent on several factors, including the strength of the magnetic field  $B_o$  in Teslas (T, the unit of magnetic flux density), the time used for scanning and the required Signal-to-Noise Ratio (SNR). Most clinical MRI facilities use a 1.5T or 3.0T magnetic field strength but recently 7.0T MRI scanners have been developed, which are capable of producing MR images of very high resolution; however, they are limited to research purposes only.

The contrast on the MR image can be manipulated by changing the parameters of spin echo sequence (a repetition of 90-degree and 180-degree RF pulses). Spin Echo sequence have two parameters: Repetition Time (TR) which is the time between consecutive 90-degree RF pulse and Echo Time (TE) which is the time between the initial 90-degree RF pulse and the echo. A  $T_1$ -weighted MRI sequence uses a short TR and short TE whereas a  $T_2$ -weighted MRI

sequence has a long TR and a long TE as shown in Fig. 7. The  $T_1$  relaxation time also known as longitudinal relaxation, which occurs in  $z$  direction, is a time constant for returning to longitudinal magnetization to the equilibrium whereas the  $T_2$  relaxation time is a measure of the decay of transverse magnetization within the  $xy$ -plane. Tissues with high fat contents such as white matter appear bright and CSF filled structures appears dark in  $T_1$ -weighted MRI. On the other hand, CSF-filled structures, tumors, edemas are seen as bright and white matters, fibrous tissues are seen as dark in  $T_2$ -weighted MRI.

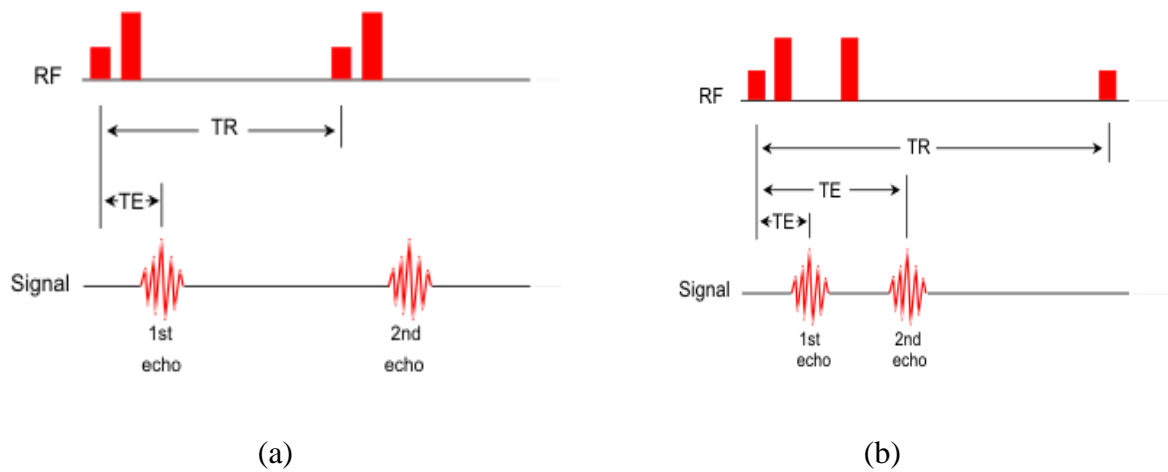


Fig. 7. Spin-echo pulse sequences. (a)  $T_1$ -weighted (b)  $T_2$ -weighted.

In the last few years, MRI techniques have been improved greatly and these improved MRI sequences at higher field strengths allow for more detailed imaging of cranial nerves and their abnormalities. A detailed review on MR imaging of the cranial nerves, with an emphasis on advanced extra-axial anatomy and illustrated with high-resolution MRI data, can be found in [38]. Imaging techniques in depicting normal anatomy as well as infectious, inflammatory, traumatic and congenital pathology affecting the cranial nerves are surveyed in [39] [5] [40].

*Steady State Free Precession (SSFP)* MRI is a type of gradient echo MRI pulse sequence that uses a steady transverse magnetization between successive cycles. A Gradient-echo sequence generally consists of repeated RF pulses and the imaging gradient [41]. These sequences have high contrast, sub-millimetric spatial resolution to highlight the course of each cranial nerve.

The family of SSFP sequence includes: *Balanced Fast Field Echo (bFFE)*, *Fast Imaging with Steady Precision (FISP)*, *Constructive Interface in Steady State (CISS)*, and *Balanced Turbo Field Echo (bTFE)*. These pulse sequences have the advantage of producing images with increased signals from fluids (like T<sub>2</sub>-weighted sequence) as well as retaining T<sub>1</sub>-weighted tissue contrast. The *bFFE* sequences, use a balanced gradient waveform, starting with the 90-degree RF pulse and then spins in a steady-state. The balanced gradient maintains the transverse and longitudinal magnetization so that both the T<sub>1</sub> and T<sub>2</sub> tissue contrast retain. *Both bFFE and CISS sequences have high spatial resolution to depict cranial nerves* [42] [43] [38] [44]. One of the limitations of the CISS sequence is that it has a longer acquisition time. *Fast Imaging Employing Steady State Acquisition (FIESTA)* is another sequence in the SSFP family which overcomes this limitation of CISS and provides images of fluid filled structures within a very short acquisition time. The FIESTA sequence is the potential imaging sequences in visualizing the lower cranial nerves attached with the posterior cranial fossa (part of the intracranial cavity containing brainstem and cerebellum) as showed in [45] [46] [47].

Tractography is a three-dimensional fiber tract reconstruction process based on the anisotropic diffusibility of water molecules (H<sup>+</sup> protons) in biological tissues containing large numbers of fibers. It is performed using Diffusion MRI (d-MRI) data, which makes use of this diffusibility property. The tractography of some of the cranial nerves (Cranial nerves II, III, and



V) from 3T Diffusion-Weighted Tensor Imaging (DTI) is shown in [49]. They attempted to reconstruct the tracts of cranial nerves II to XII but only cranial nerves II, III and V showed an acceptable degree of reconstruction. Due to the limited resolution of the DTI, they could not visualize the smaller and more diffuse nerve bundles (CN IV, IX, XI and XII). The DTI process is unable to distinguish criss-crossing fibers within a single voxel.

To address this issue, Diffusion Spectrum MRI (DSI) and High-Angular Resolution Diffusion Imaging (HARDI) were developed, which could image complex distributions of intra-voxel fiber orientation [50] [51]. DTI is further discussed elaborately in Section 3.3.3. Kabasawa et al. [52] presented a feasibility study for cranial nerve fiber tracking with enhanced reconstruction (PROPELLER) based Diffusion Tensor fiber Tractography (DTT) using 3T MRI data. They argued that the current state of the art for DTI acquisition is based on Single-Shot Echo Planner Imaging (ssEPI) which might suffer from low SNR and high magnetic susceptibility. As a result, it is challenging to visualize small anatomical structures like cranial nerves. On the other hand, PROPELLER-based DTT does not suffer from such kinds of artifacts and thus is able to visualize small neurofiber tracts such as cranial nerves. The cited research on diffusion imaging does not invalidate our contour model framework, although our own work did not build on diffusion images because of a paucity of such imaging data for cranial nerves. The application of the contour models described in this dissertation is feasible with diffusion images and is planned in future work.

## 2.3 Conclusion

In this chapter, we have presented anatomical description of all the twelve pairs of cranial nerves including their origin, exit point and functions. However, in this dissertation, we have

targeted the brainstem cranial nerves III to XII which can be extensible to olfactory and optic nerve.

Depiction of cranial nerves requires special MR imaging sequences such as gradient echo pulse sequences which provides higher sub-millimetric spatial contrast w.r.t. background. Potential imaging sequences that provide clear visualization of cranial nerves might include SSFP, bFFE, CISS and FIESTA.

## **CHAPTER 3**

### **BACKGROUND**

This chapter will provide a literature survey of medical image analysis with an emphasis on deformable model-based segmentation and curvilinear structure segmentation, coinciding with Section 3.1 and Section 3.2. Then Section 3.3 reviews existing optic nerve and spinal nerve segmentation methods. This section also includes a discussion of nerve fiber tractography. The construction of a Statistical Shape Models is reviewed in Section 3.5 and the registration methods of tubular models are reviewed in Section 3.6.

#### **3.1 Deformable Models in Segmentation**

Deformable models were first introduced in the late eighties [53], [54], elicited significant research interest and found numerous applications in computer vision and medical imaging including pattern recognition, computer animation, tracking, surgery simulation and image segmentation. Due to their wide range of applications, several surveys have published in this area, namely [55], [56], [57].

Deformable models have been widely used for 3D surface reconstruction and segmentation, whereas for vascular segmentation they have been used as a 2D curve. In vascular segmentation, an explicit or implicit model of a 2D curve is deformed to extract the vasculature. These deformable models of curves or surfaces are defined within an image domain and can change their shape to optimize some energy functional. The energy functional is composed of internal forces that are defined within the curve or surface itself, and external forces which are computed from image data (Xu, Pham et al. 2000).

Montagnat et. al [55] classified deformable models based on the surface geometric representation and a simplified version of this classification, relevant to this research, is illustrated in Fig. 8. Deformable models can broadly be classified into two groups – continuous and discrete models. Continuous models can be defined by implicit or explicit equations; on the other hand, discrete models are defined in terms of a finite set of points. Because of their relevance in this research, deformable model-based segmentation techniques like Snakes, Level Sets and Simplex meshes are discussed in the following sections.

### **3.1.1 Explicit Active Contours – Snakes**

Explicit or parametric active contours are represented explicitly as parameterized curves in a Lagrangian formulation. The classical example of a parametric active contour is the “Snake”. A snake is an energy-minimizing spline featuring a set of control points. The deformation of the snake is guided by external constraints and influenced by image-based forces that pull it towards image features such as contours and lines. Snakes were first introduced by Kass et. al [53] and represent an early influential and useful method for defining 2D contours in numerous image analysis tasks. The forces that move a snake are called internal and external forces. Internal forces are responsible for maintaining the smoothness and continuity of the contour while external forces pull the snake towards the desired image features. Snakes were originally applied to 2D images, and represent 2D energy-minimizing deformable parametric contours to detect the object boundary, based on the assumption that the boundary is piece-wise continuous.

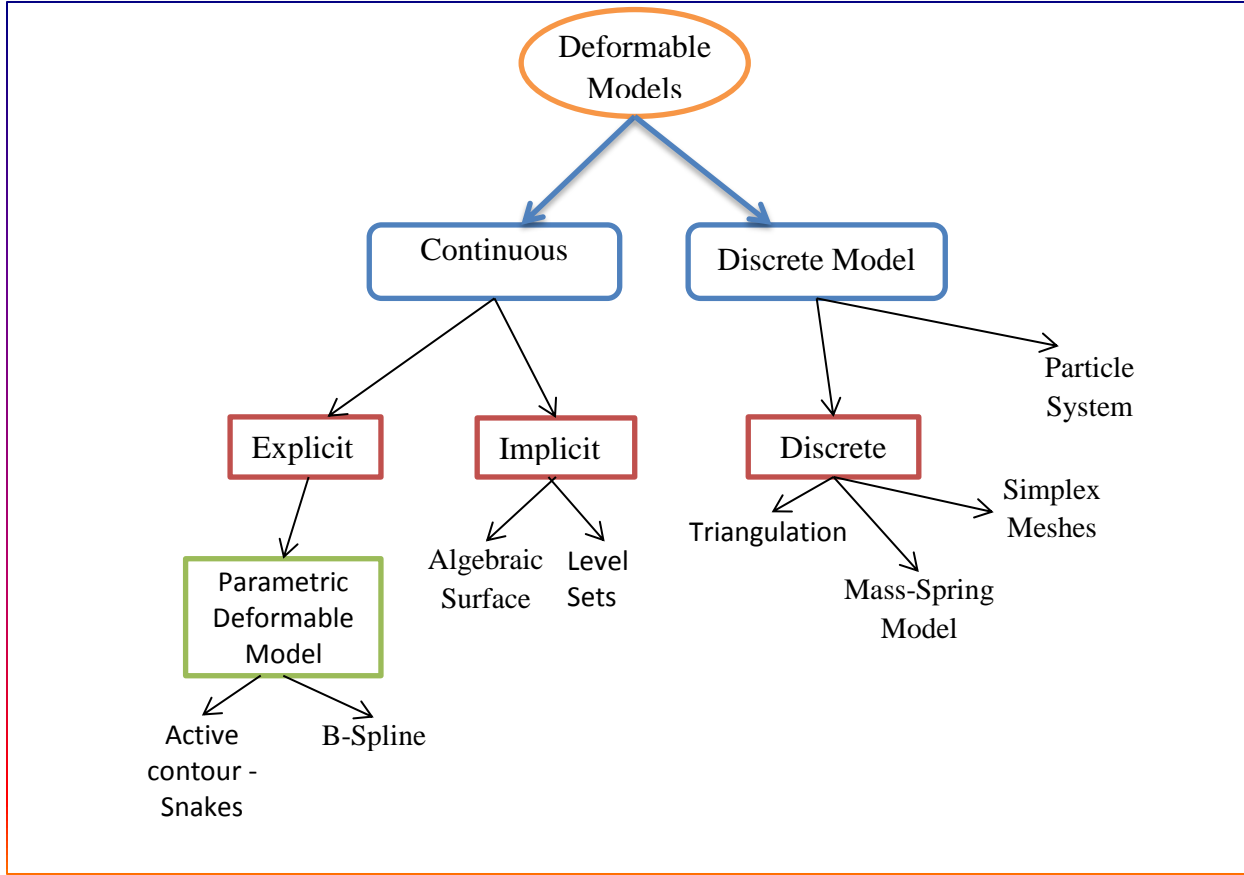


Fig. 8. Simplified classification of deformable models

Mathematically, a parametric deformable contour represented in the image plane  $(x, y) \in \mathbb{R}^2$  has the following form:

$v(s) = (x(s), y(s))$ , where  $s \in [0, 1]$  and  $x, y$  are coordinate functions, and the energy functional can be written as follows [53]:

$$E_{Snake}^* = \int_0^1 E_{Snake}(v(s)) ds \quad (1)$$

$$E_{Snake}^* = \int_0^1 E_{int}(v(s)) ds + \int_0^1 E_{image}(v(s)) ds. \quad (2)$$

Here  $E_{int}$  and  $E_{image}$  are the internal force and the image-based external force, respectively.

Over the years, a few variations of the Snakes model have been developed. Topologically adaptive Snakes or T-snakes, introduced in [58], are parametrically deformable models that are embedded in an affine cell decomposition based framework, and are able to extract complex structures. T-snakes have a topology control property combined with a specific re-parameterization scheme, enabling contour splitting and merging, and also allowing for the segmentation of thin and branching structures.

Mille et. al [59] presented a deformable cylinder model that minimizes region-dependent energy functional, following a narrow band implementation, and which is capable of extracting tubular objects from medical images.

### 3.1.2 Implicit Active Contours – Level Sets

Implicit active contours in 2D are represented as curves where the evolution of the curve is dependent on Level Set functions. The main idea behind the Level Set method is to provide an implicit representation for evolving curves/contours as the zero Level Set of a higher dimensional function. Given an interface  $\Gamma$  in  $R^n$  and a speed function  $F$  which will propagate  $\Gamma$  in its direction, the goal is to analyze and compute the motion of the interface as it evolves. The function  $\phi(x, t)$  represents the interface where the zero Level Set is defined as  $\phi(x, t) = 0$  [30].

The evolution equation for  $\phi$  can be given as (3):

$$\phi_t + F|\nabla \phi| = 0, \quad (3)$$

where  $\nabla \phi$  represents the spatial gradient of  $\phi$  and  $\phi_t$  is the partial derivative of  $\phi$  with respect to  $t$ . The speed function  $F$  depends on the position and time, the geometry of the interface (its normal and its mean curvature), and the external physics [60]. A complete and detailed discussion of Level Set techniques and their applications can be found in [30] [61]. To improve

the computational efficiency of the Level Set method, Sethian [31] proposed the Fast Marching Method (FMM), which provides a fast scheme for the problems where the front advances monotonically with a speed function that does not change in sign.

Consider a monotonically advancing front, moving with speed,  $F$  whose Level Set equation has the form as shown in (3). Let,  $T(x, y)$  is the time at which the propagating curve  $\Gamma$  crosses the point  $(x, y)$ , then according to FMM the following equation should be satisfied:

$$|\nabla T|F = 1. \quad (4)$$

Here  $T(x,y)$  is called the arrival time that determines the evolution of the interface. Equation (4) is the Eikonal equation that provides a faster solution for propagating curves, yielding a computationally efficient Level Set method.

In [62], a wave propagation approach is presented to segment vasculature from 2D medical image data. This method employs a dual sigmoidal filter to determine the likelihood of each pixel being within the vessel. Using this likelihood image, a digital wave is then propagated from the base of the vascular tree which washes over the vasculature.

A Level Set implementation based on FMM to extract tubular shapes, given in [63], is based on a freezing technique. This technique involves front propagation only on the actual moving front and refraining from updating all other points to make it computationally efficient.

### 3.1.3 Discrete Deformable Models – Simplex Meshes

Discrete deformable models are represented as meshes which are defined as a set of vertices with a well-defined connectivity relationship. These models have many advantages over parametric and implicit models. Implicit models have a limitation due to their implicit nature. Particularly, an implicit approach requires a conversion to an explicit representation to apply

techniques like shape statistics or collision detection. A discrete representation can remedy this problem.

Some of the discrete representations of deformable models include triangulation, mass-spring models, particle systems and Simplex meshes. A triangulated surface is the most common discrete representation where the surface is decomposed into a set of adjacent triangles. In [64] and [65] triangular meshes are used for image segmentation. Vaselescu and Terzopoulos [66] created an adaptive mesh model using non-linear springs and masses on a triangulated mesh for surface reconstruction.

The Simplex mesh, introduced by Delingette [29], is a discrete deformable model with constant vertex connectivity used for 3D surface segmentation in [67], [68]. A  $k$ -Simplex mesh is a  $k$ -manifold discrete mesh where each vertex has  $k + 1$  constant connectivity. Based on the values of  $k$ , a Simplex mesh can represent various objects such as curves ( $k = 1$ ), surfaces ( $k = 2$ ) or volumes ( $k = 3$ ). These  $k$ -Simplex meshes have well defined dual counterparts as shown in Fig. 9.

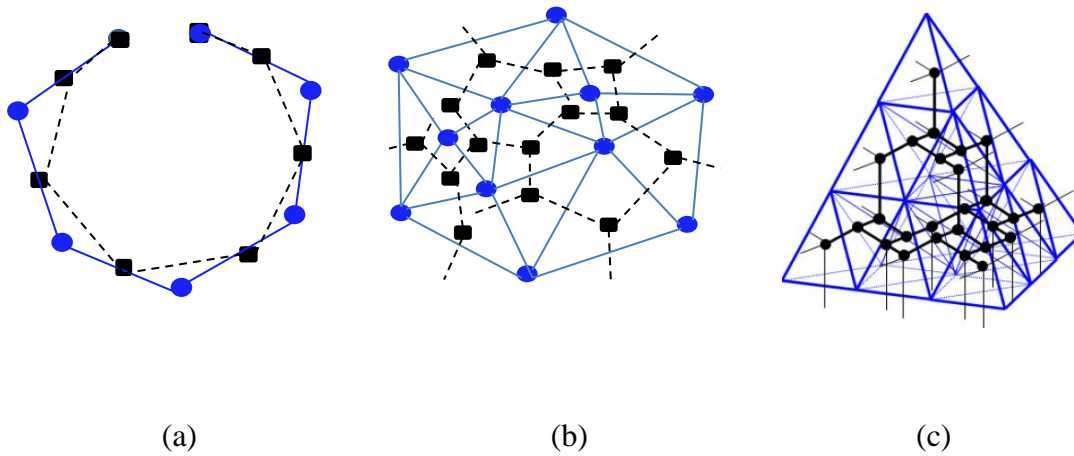


Fig. 9. Simplex Meshes. (a) 1-Simplex, (b) 2-Simplex (c) 3-Simplex. Black points and dotted lines belong to the Simplex mesh while blue points and solid lines belong to corresponding polygonal mesh.



The deformation of the Simplex mesh is based on the relative position of the vertices with respect to their neighbors. Like other deformable models, Simplex meshes are also deformed using a physical expression based on internal and external forces. Each vertex of the Simplex mesh is considered as a mass-spring system that follows the Newtonian law of motion for equilibrium as shown in (5) [29].

$$m \frac{d^2 \mathbf{P}_i}{dt^2} = -\gamma \frac{d\mathbf{P}_i}{dt} + \mathbf{F}_{int} + \mathbf{F}_{ext} , \quad (5)$$

where  $\mathbf{P}_i$  indicates relative position of the vertex,  $m$  is the mass of the vertex,  $\gamma$  is the damping factor,  $\mathbf{F}_{int}$  is the internal force and  $\mathbf{F}_{ext}$  is the image based external force.

To compute the evolution of the Simplex mesh, equation (5) is discretized over time as follows, while also providing weights  $\alpha_i$  and  $\beta_i$  to internal and external forces:

$$\mathbf{P}_i^{t+1} = \mathbf{P}_i^t + (1 - \gamma) (\mathbf{P}_i^t - \mathbf{P}_i^{t-1}) + \alpha_i \mathbf{F}_{int} + \beta_i \mathbf{F}_{ext} . \quad (6)$$

One of the advantages of Simplex mesh models is that the adaptation, refinement and level of smoothness can be controlled in a computationally efficient manner. Furthermore, the constant vertex connectivity of Simplex meshes enables the definition of discrete geometric quantities such as the normal vector, Simplex angle and mean curvature at each vertex.

Due to their discrete and point-based representation, Simplex meshes can accommodate important features such as:

- 1) *Multi-resolution representation*: The Level of Detail (LOD) of a representation can be increased by simply increasing number of points in surface (2-Simplex) or curve (1-Simplex). This representation is computationally efficient, especially during registration because it enables a coarse-to-fine optimization, which alleviates the effect of local optima.

2) *Collision detection*: While segmenting multiple structures that are near each other, a spatial overlap between these structures must be prevented using a static collision detection mechanism. The Simplex model can be easily adapted to support a multi-surface representation [68], which can enable static collision detection.

3) *Shape Statistics*: A Statistical Shape Model (SSM) (discussed in Section 3.4) requires a finite set of points to represent the shape. The shape training is performed by computing the point set within a suite of surfaces or contours. The Simplex representation is a point-based representation that simplifies shape training in relation to the implicit representations that requires a conversion to an explicit surface or contour.

Gilles et al. [68] proposed an approach for musculoskeletal segmentation and registration using the 2-Simplex mesh. They have extended the 2-Simplex originally described in [29], through improved topological operators for local and global mesh adaptation as well as multi-surface modeling based on static collision handling founded on the medial representation of the anatomical surfaces of interest. During multi-region segmentation, the collision handling ensures that the object boundaries do not overlap each other or self-penetrate. In multi-surface muscle segmentation, the spatial overlap between muscles is handled using this collision detection scheme. The source to target image registration was performed through model deformation. An initial template is aligned with the target image which is then deformed iteratively until it matches the boundary of target image. This registration is guided by equation (7).

$$\tilde{j} = \underset{(-\frac{d}{s} < j < \frac{d}{s})}{\operatorname{argmin}} \Delta(S(\eta(\mathbf{P}^0)), T(\eta(\mathbf{P} + j\mathbf{s}\mathbf{n}))), \quad (7)$$

where  $S$  is the source image,  $T$  target image,  $\mathbf{P}^0$  is the vertex position of  $S$  where the model is initially aligned,  $\eta$  is the vertex neighborhood around  $\mathbf{P}^0$ ,  $\Delta$  is an image distance measure,  $\mathbf{n}$  is

the surface normal direction,  $d$  is the search direction and  $s$  is the step size.  $\tilde{j}$  is the measure of optimal shift between the model and the target image.

### 3.2 Segmentation of Curvilinear Structures

The detection and segmentation of tubular structures in 3D images is an important issue for the diagnosis and treatment of vascular diseases. Although a tremendous amount of previous and on-going research has been dedicated towards algorithms for segmenting curvilinear tissues, most of these techniques have been applied to the segmentation of blood vessels, and comparatively few have been applied to cranial nerves. This section will focus on discussing the main concepts in the segmentation of curvilinear structures.

#### 3.2.1 Hessian-based Segmentation

Operators that sensitive to local structure and are based on Hessian analysis have been successfully used to detect vascular patterns from medical images. The Hessian has an intuitive justification in the context of vessel detection, that is, it can encode the local principal directions of a curvilinear structure to characterize the image geometry. The Hessian matrix is the most popular tool to capture such information. Sato et al. [69] developed a multiscale 3D line filter, based on eigenvalues of the Hessian matrix, with the purpose of enhancing line structures of various widths. Following this idea, several publications were dedicated to multiscale Hessian-based filters for tubular structure enhancement [70] [71] [72] [73] [74].

These approaches are based on the eigenvalues of the Hessian matrix. The Hessian matrix of a 3D image  $I(\mathbf{x})$ , where  $\mathbf{x} = (x, y, z)$ , is given by (8):

$$H = \nabla^2 I(\mathbf{x}) = \begin{bmatrix} I_{xx}(\mathbf{x}) & I_{xy}(\mathbf{x}) & I_{xz}(\mathbf{x}) \\ I_{yx}(\mathbf{x}) & I_{yy}(\mathbf{x}) & I_{yz}(\mathbf{x}) \\ I_{zx}(\mathbf{x}) & I_{zy}(\mathbf{x}) & I_{zz}(\mathbf{x}) \end{bmatrix}. \quad (8)$$

In the above equation,  $I_{\alpha\beta}(\mathbf{x})$  represents the partial second order derivative of the image  $I(\mathbf{x})$  over  $\alpha$  and  $\beta$ . For example,  $I_{xx}(\mathbf{x}) = \frac{\partial^2}{\partial x^2} I(\mathbf{x})$ ;  $I_{xy}(\mathbf{x}) = \frac{\partial^2}{\partial x \partial y} I(\mathbf{x})$ , and so on. In order to make these derivatives' computation well posed in the presence of noise and to impose a scale on the detection, they are pre-filtered with a Gaussian kernel. This filtering is performed by simply convolving the image  $I(\mathbf{x})$  with derivatives of the Gaussian kernel as shown in (9) and (10). In practice, the response of the Gaussian kernel is calculated at several scales  $\sigma$  that fall within a range of interest, e.g. the expected radius of a blood vessel.

$$I_{\alpha\beta}(\mathbf{x}) = \frac{\partial^2 G(\mathbf{x}, \sigma)}{\partial \alpha \partial \beta} * I(\mathbf{x}) \quad (9)$$

$$G(\mathbf{x}, \sigma) = \frac{1}{\sqrt{(2\pi\sigma^2)^3}} e^{-|\mathbf{x}|^2 / 2\sigma^2}. \quad (10)$$

The Hessian Matrix  $H$  represents the second order structure of local intensity variation around each voxel of a 3D image. Let the eigenvalues of  $H$  be  $\lambda_1$ ,  $\lambda_2$  and  $\lambda_3$  where they are ordered as  $|\lambda_1| < |\lambda_2| < |\lambda_3|$ , and their corresponding eigenvectors are labeled  $\vec{v}_1$ ,  $\vec{v}_2$  and  $\vec{v}_3$  respectively. According to [70], a voxel inside the tubular structure is identified by *one* eigenvalue  $\lambda_1$  *near zero* and *two much larger* eigenvalues  $\lambda_2$  and  $\lambda_3$ , as shown in Fig. 10

Table 2 summarizes the relationship among these eigenvalues to detect different patterns. Here N, H, L represent noisy, high and low values of  $\lambda_k$ , respectively. The +/- sign indicates the polarity of  $\lambda_k$  i.e. brightness/darkness. For example, a bright tubular structure in a dark background has a near-zero  $\lambda_1$  but significantly larger values of  $\lambda_2$  and  $\lambda_3$  of the same polarity.

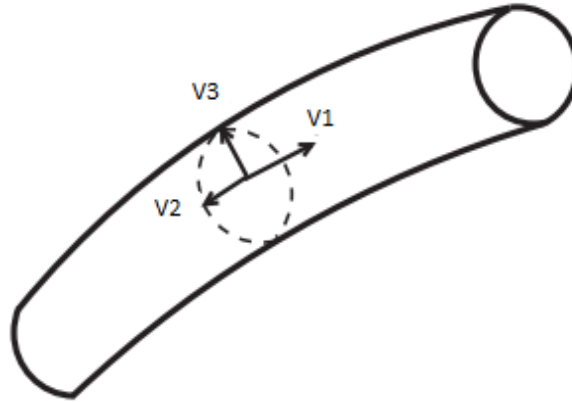


Fig. 10. At locations centered within tubular structures the eigenvector ( $v_1$ ) corresponding to the smallest eigenvalue ( $\lambda_1$ ) of the Hessian matrix is along the vessel direction and the other eigenvectors  $v_2$  and  $v_3$  span the cross-sectional plane. Reproduced from [75].

Table 2. Different patterns in 3-D image based on eigenvalues of Hessian. Reproduced from [70]

Patterns	$\lambda_1$	$\lambda_2$	$\lambda_3$
No preferred direction	N	N	N
Bright plate like structures	L	L	H-
Dark plate like structures	L	L	H+
Bright tubular structures	L	H-	H-
Dark tubular structures	L	H+	H+
Bright blob-like structures	H-	H	H-
Dark blob-like structures	H+	H+	H+

The vesselness measure at a scale  $\sigma$ , which is based on eigenvalue analysis, can be expressed as:

$$V(\mathbf{x}, \sigma) = \begin{cases} 0 & \text{if } \lambda_2 > 0 \text{ or } \lambda_3 > 0 \\ \left[1 - \exp\left(-\frac{R_A^2}{2\alpha^2}\right)\right] \exp\left(-\frac{R_B^2}{2\beta^2}\right) \left[1 - \exp\left(-\frac{S^2}{2c^2}\right)\right] & \text{otherwise} \end{cases} \quad (11)$$

The parameters  $\alpha$ ,  $\beta$  and  $c$  tune the sensitivity of the vesselness filter.  $R_A$ ,  $R_B$  and  $S$ , corresponding to the local measure of asymmetry, blobness and degree of image structure, respectively, are defined as:

$$R_A = \frac{|\lambda_2|}{|\lambda_3|}; \quad R_B = \frac{|\lambda_1|}{\sqrt{|\lambda_2\lambda_3|}}; \quad S = \sqrt{\sum_j \lambda_j^2}. \quad (12)$$

The vesselness filter described in (11) enhances vessel-like structures in the image and reduce the effects of other morphologies. To realize the multiscale feature of (11), the response of the filter is computed over a range of scales, and then the scale at which the filter's response is maximum is recorded as the size of the vessel to be detected.

### 3.2.2 Centerline, Medial Axis, and Skeleton-based Segmentation

The centerline of a tube-like structure can be considered as a 1D representation of 2D or 3D curvilinear structures. Centerline tracking has been used as an integral method in many vessel segmentation techniques.

Centerline-based algorithms seek to extract the medial line of the vessel and then use them to efficiently constrain the segmentation of the vessel's contours. In [71], [76], [73], centerline tracking is performed using eigenanalysis of the Hessian matrix. Frangi et al. [71] modeled the central vessel axis using B-splines. The B-spline model is then deformed by

minimizing an external energy, where the external energy is the output of the image Hessian-based vesselness filter (as discussed in Section 3.2.1). Wink et al. combined Frangi's vesselness measure to the Fast Marching shortest path problem to determine the central axis of vessels.

Aylward et al. developed a centerline extraction algorithm based on an intensity ridge traversal [76]. An intensity ridge map is a 3D elevation map in which the grayscale image intensity is mapped to height. The ridge points in the intensity map are locally maximal in the gradient direction. This approach is semi-automatic, starting from a manually selected seed point and a seed scale, where the seed point is on, or near, a vessel. The subsequent centerline extraction is automatic. From the initial seed point and seed scale, the full extent of the ridge is traversed by a step maximizing procedure based on the maximum eigenvalue's eigenvector of the Hessian. This extracted intensity ridge represents the vessel's medial axis. Along with the medial axis, the radius of the tube at each ridge point is also estimated using a scale based approach. In [76], the authors paid particular attention to both the quantitative and qualitative validation of their algorithm, demonstrating its robustness under parameter changes and image acquisition noise. The main application of this approach is in multimodal registration, which will be discussed later in this chapter (Section 3.6.3).

### 3.2.3 Minimal Path-based Segmentation

If the start and end points are available for a given vascular segment, the centerline extraction problem can be solved by path minimization techniques. By defining a cost function inside an image, the Minimal Path becomes the path for which the integral of the cost between the two points is minimal. Based on the optimization method involved, minimum path based techniques differ notably. One approach, called Dijkstra's shortest path algorithm [77], solves

the Minimal Path problem by using graph theory and dynamic programming. Dijkstra's shortest path algorithm finds the Minimal Path between two end nodes in a discrete manner where a cost is associated with transitions from each point to its neighbors. This optimization method has been used in [73], [78] and [79]. Although such algorithms show computational efficiency, they might introduce metrication errors<sup>5</sup> due to their discrete nature, as shown in Fig. 11 [80].

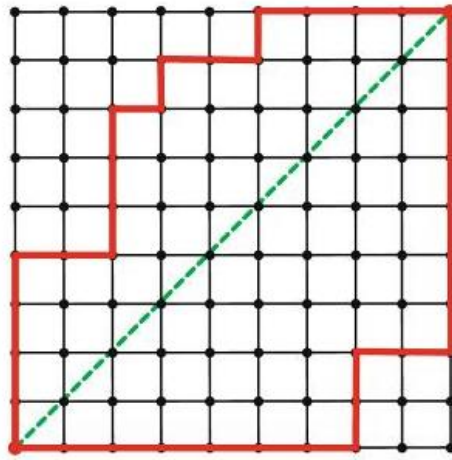


Fig. 11. Metrication error. Shortest path measured by Dijkstra's algorithm (green dashed line) do not converge to the true shortest path (red solid line), no matter how much the grid is refined.

To avoid metrication errors, Cohen and Kimmel [81] solved the Minimal Path problem with a front propagation equation and a Fast Marching method. An improved version of this method was presented in [80] which has much similarities with Dijkstra's method, but it had the advantage of being consistent with continuous formulation of the Minimal Path problem. This Fast Marching optimization of the Minimal Path provides a globally optimal curve by minimizing the active contour energy. The method of Minimal Path extraction exhibits some

---

<sup>5</sup> Due to the discrete nature of the graph, the approximated shortest distance measured from Dijkstra's algorithm might become inconsistent with the true graph distance, this phenomenon is called metrication error.



limitations: this method in general does not correspond to the true centerline of the vessel, and it also does not provide any information about the vessel boundary or local width.

A Minimal Path between two points, optimal in *geodesic distance*, globally minimizes an energy functional defined as an image-based potential function. Assuming that  $C$  is the parameterized contour and  $s$  is the arc-length parameter such that  $||C'(s)|| = 1$  [81], the energy functional can be represented using following form:

$$E(C) = \int_{\Omega} P(C(s)) ds, \quad (13)$$

where  $P$  is the image potential function and  $\Omega$  is the image domain.

The solution of (13) can be obtained by computing the minimal action map  $U$ . The minimal action map is the minimal energy integrated along a path between a starting point  $p_o$  and any other point  $x$  of the image domain  $\Omega$ :

$$\forall x \in \Omega, \quad U(x) = \min_{C \in \mathcal{A}_{p_o, x}} \left\{ \int_{\Omega} P(C(s)) ds \right\}. \quad (14)$$

In equation (14),  $\mathcal{A}_{p_o, x}$  is the set of paths linking  $x$  to  $p_o$ . The values of  $U$  are also called arrival times of the front propagating from the source  $p_o$ . Assuming that the potential  $P > 0$ , the action map has only one local minimum, i.e., the starting point  $p_o$ . Now, according to FMM,  $U$  satisfies the following Eikonal equation:

$$||\nabla U(x)|| = P \quad \text{for } x \in \Omega, \quad \text{and} \quad U(p_o) = 0, \quad (15)$$

which can be solved by the Fast Marching approach. Finally, the Minimal Path between  $p_o$  and  $p_l$  can be established by a simple back propagation on the action map.

Li and Yezzi [82] extended the Minimal Path technique by incorporating an extra dimension into the search space which represents the entire structure as a 4D curve. Using this approach the centerline, along with the entire tubular surface will be segmented. The authors

represented the tubular structures as an envelope of a family of spheres with continuously changing center points and radii. Each 4D coordinate on the curve consists of three spatial coordinates and the fourth coordinate represents the vessel thickness at the corresponding 3D point. According to authors, this approach combines Minimal Path and active surface techniques, which results in a well centered centerline and a direct approximation of the vessel surface.

Following the seminal idea of Li and Yezzi, Benmansour and Cohen [83] developed a vessel segmentation approach involving a Minimal Path extraction which is based on the Optimally Oriented Flux (OOF). The OOF is a metric that can extract geometric information from 3D images, and this is useful for detecting edges and ridges at any orientation. The authors claimed that their introduced anisotropic metric based on OOF allows for faster propagation along the vessel's centerline.

### **3.3 Nerve Segmentation**

Although vascular segmentation has been an active research area and a tremendous amount of past and on-going research has been dedicated to it, very few of these techniques have been applied to segmenting cranial nerves. All the vessel segmentation techniques discussed so far in this chapter have been applied on blood vessel segmentation, which is a comparatively simpler problem than nerve segmentation due to the high contrast available in typical MR angiography data, as shown in Fig. 12. Due to their fine structure, cranial nerves require images of high resolution and contrast with respect to corticospinal fluid, which entails special MRI pulse sequences to be detected from medical images as discussed in Section 2.2.

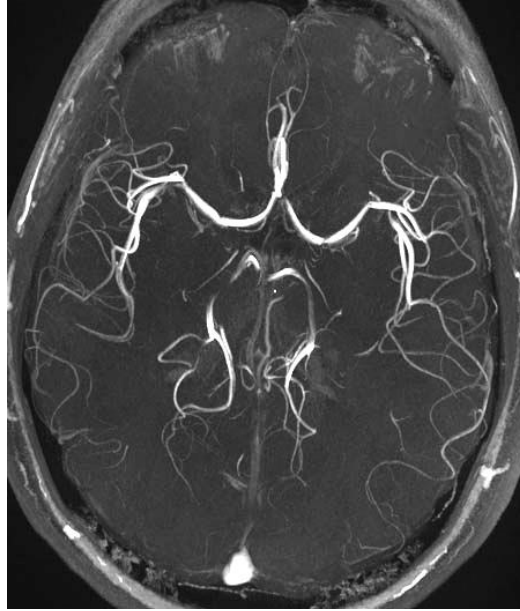


Fig. 12. MRA of a brain slice showing blood vessels and veins.

### 3.3.1 Optic Nerve Segmentation

The localization of the optic nerve in MR or CT images might be difficult due to the variability of contrast along the nerve path, although this nerve is less challenging than many of the brainstem nerves because of its larger size comparative to other nerves. Several recent approaches have been suggested for segmenting the optic nerves and tracts [84], [79], [85], [86] and [87].

Noble and Dawant [79] presented an atlas-based segmentation of the optic nerves and chiasm from both MR and CT modalities. In this approach, a model-based atlas is created by combining an optimal path algorithm (i.e., Dijkstra's shortest path algorithm) with a model of average shape and of typical intensity information. The subsequent segmentation based on this model is performed by computing the centerline path and the radius function at regular sample points along the path. Although this approach can segment optic nerves, it cannot be applied to

the thinner cranial nerves because this method requires a manually pre-segmented structure to create the atlas. Another limitation of this approach is that it only includes first-order statistics that cannot explicitly account for shape variability.

In [86] and [85] other atlas-based segmentation of the optic nerve and its surrounding structures (such as chiasm, lenses, eyeballs etc.) are presented. To improve the accuracy of their segmentation results, Panda and Asman [87] extended the single atlas approach to a multiple atlas approach. Their technique proposes a segmentation of the optic nerves, eye globes and muscles by employing a pairwise affine and non-rigid registration techniques.

### 3.3.2 Spinal Nerve Segmentation

Dalca et al. developed a segmentation method of spinal nerve bundles based on particle filtering. Particle filters approximate the posterior density of the state variables given the observation variables. Nerve segments were modeled using Bezier splines and the propagation of the nerve segments was done by a dynamic model. Specifically, each segment of a nerve bundle was represented by an 8-feature vector, termed a particle,  $\mathbf{h}$ :

$$\mathbf{h} = (\mathbf{p}_0, \mathbf{p}_1, \mathbf{p}_2, \mathbf{p}_3, r_1, r_2, r_3, \mu), \quad (16)$$

where  $\mathbf{p}_0, \mathbf{p}_1, \mathbf{p}_2$  and  $\mathbf{p}_3$  are control points which constitute the centerline of the segment using a 3<sup>rd</sup> degree Bezier curve;  $r_1, r_2, r_3$  are control points that defines a radius function via a 2<sup>nd</sup> order Bezier curve and  $\mu$  is the mean image intensity inside the segment. The dynamic model introduced in this method specifies the construction of a state vector at time step  $t$ , given the state vector at previous time step  $t-1$ . The likelihood of a nerve at a specific location in the MR image measures how well the particles can describe the corresponding segment of the image. Based on

the likelihood measure, the particles are weighted in each iteration. This particle filtering-based method is highly sensitive to parameter initialization.

### 3.3.3 Nerve fiber Tractography

Tractography is a three-dimensional fiber tract reconstruction process based on the anisotropic diffusion of biological tissue containing large number of fibers, like brain white matter. It provides the mapping of neural fiber pathways which allows the visualization of the fiber tracts. Tractography is constructed from Diffusion MRI (dMRI), which captures the average diffusion of water molecules in biological tissues at a scale much smaller than the imaging resolution [88]. Water molecules in fibrous structures such as white matter diffuse predominantly along the length of nerve fibers and are hindered across nerve fiber membranes, which results in anisotropic diffusion. The influential *diffusion tensor* model was proposed by [89]. In this model, diffusion behavior is characterized in a voxel-by-voxel manner where the diffusion tensor yields the diffusion coefficient corresponding to any direction in space [75]. The diffusion tensor at each voxel is defined as a  $3 \times 3$  symmetric matrix as shown in (17), which can be visualized as a 3D ellipsoid, as shown in Fig. 13.

$$\mathbf{D} = \begin{bmatrix} D_{xx} & D_{xy} & D_{xz} \\ D_{yx} & D_{yy} & D_{yz} \\ D_{zx} & D_{zy} & D_{zz} \end{bmatrix}. \quad (17)$$

The diffusion Probability Density Function (PDF) can be denoted as the function  $P(\mathbf{R}, t)$ , which represents the probability that a water molecule located at an initial position  $\mathbf{r}_0$  has moved to position  $\mathbf{r}$  in time  $\tau$ . Given that  $\mathbf{R} = \mathbf{r} - \mathbf{r}_0$ , the rate of change of  $P(\mathbf{R}, t)$  can be defined as in equation (18):

$$\frac{\partial P(\mathbf{R}, t)}{\partial t} = \mathbf{D} \nabla^2 P(\mathbf{R}, t), \quad (18)$$

where,  $\mathbf{R}$  is the net displacement vector representing the displacement of water molecules at time  $\tau$ . The solution of (18) is  $P$ , which describes the probability distribution of how the water molecules diffuse over time  $t$ .

The reconstruction method of Diffusion Tensor Imaging (DTI) is based on the assumption that the PDF of the diffused water molecules has a 3D Gaussian distribution, and is expressed as (19) [89]

$$P(\mathbf{r}, t) = \frac{1}{\sqrt{(4\pi t)^3 |\mathbf{D}|}} \exp\left(-\frac{\mathbf{r}^T \mathbf{D}^{-1} \mathbf{r}}{4t}\right), \quad (19)$$

where,  $\mathbf{D}$  is the diffusion tensor defined in equation (17) and  $\mathbf{r}$  is the relative spin displacement.  $|\mathbf{D}|$  is the determinant of  $\mathbf{D}$ .

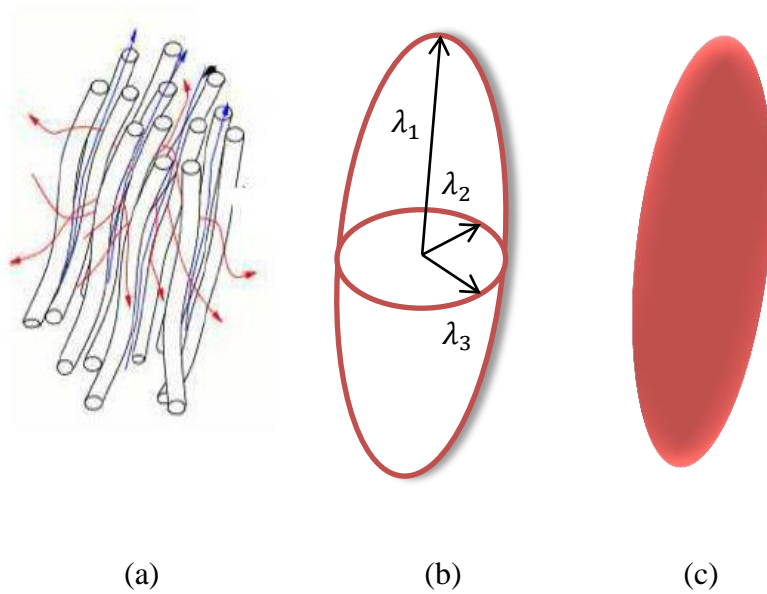


Fig. 13. Diffusion Tensor representation, reproduced from [75]. (a) Brownian motion of water along the fibers. (b) Eigen-decomposition of DT. (c) Ellipsoid representation of DT.

The Diffusion Tensor matrix  $\mathbf{D}$  can be decomposed into three eigenvalues ( $\lambda_1, \lambda_2, \lambda_3$ ) and the corresponding eigenvectors ( $e_1, e_2, e_3$ ), where  $\lambda_1 \geq \lambda_2 \geq \lambda_3$ . The largest eigenvalue  $\lambda_1$  and its corresponding eigenvector  $e_1$  give the first principal direction of the diffusion tensor, while the other two eigenvectors span the plane orthogonal to it. The eigenvalue decomposition of  $\mathbf{D}$  is also used to extract important orientation information of the tissue structures and some useful measures, such as mean diffusivity (MD) and fractional anisotropy (FA). The FA measure is used to show the region of anisotropy and is defined as (20) [90]:

$$FA = \sqrt{\frac{3}{2}} \sqrt{\frac{(\lambda_1 - \bar{\lambda})^2 + (\lambda_2 - \bar{\lambda})^2 + (\lambda_3 - \bar{\lambda})^2}{\lambda_1^2 + \lambda_2^2 + \lambda_3^2}}. \quad (20)$$

Here,  $\bar{\lambda}$  is the mean diffusivity. For an isotropic medium FA is 0, and 1 for a strongly anisotropic medium.

White matter tractography is the computational process through which the fibers are detected and delineated. It is also called streamline fiber tracking. The streamline tracking algorithm, proposed in [89], starts from a seed voxel and traces down the trajectory in a voxel-by-voxel manner by estimating the direction of the eigenvector  $e_1$  as the direction of the local fiber orientation.

Even though DTI is a powerful tool for white matter tractography in many clinical applications, it has some limitations due of the Gaussian PDF assumption. Due to this assumption, DTI cannot directly image multiple fibers crossing within the same voxel.

To capture multiple fiber directions within the same imaging voxel, Diffusion Spectrum Imaging (DSI), was introduced by [91]. DSI extracts the diffusion PDF in multiple gradient orientations that span a Cartesian grid of points [92],[50]. Since visualization of the 3D diffusion PDF at every voxel is expensive, the diffusion Oriented Distribution Function (ODF) is calculated from the PDF which contains the full angular information of the diffusion PDF. The

DSI technique requires a very strong gradient strength (b-value) and a long acquisition time. To reduce the acquisition time, a single shell High Angular Resolution Diffusion Imaging (HARDI) was introduced in [75, 92] and [93], which can extract the desired diffusion ODF in a single b-value [75].

### 3.4 Survey of Statistical Shape Models

Statistical Shape Models (SSMs) have been an established segmentation tool for medical images, especially in those cases where the traditional image segmentation methods fail due to insufficient resolution or contrast. The goal of SSMs is to capture the shape as well as shape variations of the features to be segmented. This shape information is integrated with the model as *a priori* knowledge which makes the approach more stable against local image artifacts and perturbations while segmenting structures from medical images.

The shape of an object is invariant to Euclidian transformations, i.e., the shape remains the same after removing translation, rotation and scaling effects from the object [94]. This information is utilized using statistical analysis in model-based segmentation which provides more optimized results. Cootes et al. introduced SSMs, also known as Active Shape Models (ASMs) [95], along with Active Appearance Models (AAMs) [96]. ASMs and AAMs construct models by learning the variability patterns of shape and intensity appearance respectively from a training set of images and then deforming the model within the target image to be segmented in a manner consistent with these statistics. In other words, the deformation process proceeds in a manner consistent with the shape or appearance present in the training set. In the ASM approach, shape variation is modeled using Principal Components, whose directions coincide with the eigenvectors of the landmarks' covariance matrix. Cootes et al. [95] constructed the ASM using



expert provided, manually identified landmarks in 2D, which made its 3D extension difficult due to the user supervision and complexity of landmark localization in areas of low contrast.

Cremers et al. [97] integrated a diffusion Snake-based segmentation process with nonlinear shape statistics. The authors claimed that the integration of nonlinear statistics as a shape prior enables this approach to capture the fine details of shape variation. An extensive review of Statistical Shape Models can be found in [98].

Nain et al. [99] proposed a blood vessel segmentation technique that incorporates image statistics and shape information to a region-based active contour model. Besides segmenting the vasculature, this method also penalizes any deviation from a tubular structure. A weak shape prior based on a local neighborhood, called a Ball measure, is computed and added with the image force to deform the active contour.

Tejos and Irarrazaval [100] presented a Simplex Mesh Diffusion Snakes (SDMS) method that combines Simplex meshes and statistical shape knowledge through diffusion snakes. They have extended the 2D Deformable Snakes (DS) proposed in [97] in 3D and then integrated Simplex mesh to represent the boundaries of the object of interest. They proposed an iterative Statistical Shape Model where the shape training was performed using General Procrustes Analysis. This shape training did not require any pre-segmented shape and the training shapes were created using their own SDMS method. The shape energy term has the form given in (21).

$$E_{Shape}(\tilde{\mathbf{X}}) = \frac{1}{2} (\tilde{\mathbf{X}} - \bar{\mathbf{X}})^T \boldsymbol{\Sigma}_{\perp}^{-1} (\tilde{\mathbf{X}} - \bar{\mathbf{X}}). \quad (21)$$

Here  $\mathbf{X}$  is  $N \times d$  vector of Simplex nodes,  $\tilde{\mathbf{X}}$  are the aligned nodes with respect to the mean shape  $\bar{\mathbf{X}}$  and  $\boldsymbol{\Sigma}$  is covariance matrix. This shape energy functional was integrated with the energy functional derived from the input image. The evolution of the Simplex was guided by the differential equation shown in (22).

$$\frac{dX}{dt} = - \frac{\partial(E_{Shape}(\bar{X}))}{\partial \bar{X}^T}. \quad (22)$$

A prior knowledge-based discrete deformable model for subject-specific musculoskeletal modeling was proposed in [101]. They constructed a Statistical Shape Model, as well as an Active Appearance Model (based on consistent medical image modalities) for the structures of interest, which were then integrated into Gilles' multi-resolution Simplex-based deformable model to produce an atlas of bone structures of the leg. The initialization of the atlas in the images was performed in an adaptive manner, which could overcome variations in image resolution and field of view.

### 3.5 Shape Representation and Model Construction

The first fundamental decision that needs to be made when constructing Statistical Shape Models is the choice of shape representation. Based on the segmentation method used, these representations may vary. Shapes have been represented using points, curves, medial models or surface meshes in the literature. Among them, the most common and generic method for shape representation is by using points. A subset of these point sets are often referred to as landmarks. The most widely used landmark-based SSM was proposed by Cootes et al. [102], called the Point Distribution Model (PDM). A PDM computes a geometric mean and some statistical modes of geometric variation derived from a set of training dataset. In mesh representations, additional connectivity information between points is stored. In medial-based representations, a medial model generally consists of a set of points on the centerline of the object and the corresponding radii. Pizer et al. [103] represented the medial model shape representation and termed it as *m-reps*. A continuous version of *m-reps* was used to build SSMs in [104].

Basically, an SSM computes the mean shape and the most important modes of variation from a collection of training data sets. The basic two steps for constructing a shape model are: (1) shape alignment and (2) modeling shape variations.

### 3.5.1 Ordinary Procrustes Analysis

Since shapes are invariant under a similarity transform, training shapes need to be aligned by filtering all the global transformations comprised of translation, rotation and scaling. This can be done by establishing a common coordinate reference frame with respect to the position, rotation and scale, commonly referred to as a *pose*. The most popular data alignment method is the Procrustes analysis, which minimizes the Euclidean mean-squared distance between shapes, known as the *Procrustes distance*. The ordinary Procrustes Analysis (OPA) works by aligning two shapes through one-to-one correspondences.

Consider two shape  $\mathbf{X}_1$  and  $\mathbf{X}_2$ , each having a finite number of  $k$  points in  $n$  dimensions. Each  $\mathbf{X}_i$  is represented in a vector format:

$$\mathbf{X}_i = (x_{i1}y_{i1}z_{i1}, \dots \dots \dots x_{ik}y_{ik}z_{ik}). \quad (23)$$

First, the centroid of each shape  $\mathbf{X}_i$  must be calculated as:

$$(\bar{X}_i, \bar{Y}_i, \bar{Z}_i) = (\frac{1}{k} \sum_{j=1}^k x_{ij}, \frac{1}{k} \sum_{j=1}^k y_{ij}, \frac{1}{k} \sum_{j=1}^k z_{ij}). \quad (24)$$

Now, the translation component between the two shapes is removed by either translating the centroid of one shape to another or by translating each of the centroids to the origin. The scaling component is removed by scaling the object in a way so that the root-mean-squared distance from the points to the translated origin is 1. The rotational component is finally removed using Singular Value Decomposition (SVD) [94]. Finally, the distance between the two shapes is minimized by minimizing the following Procrustes distance:

$$P_d^2 = \sum_{j=1}^k [(x_{1j} - x_{2j})^2 + (y_{1j} - y_{2j})^2 + (z_{1j} - z_{2j})^2]. \quad (25)$$

### 3.5.2 General Procrustes Analysis

Unlike the OPA method, the General Procrustes Analysis (GPA) [105] method optimally superimposes a set of shapes in a group-wise manner instead of superimposing them on an arbitrary selected shape. The GPA technique is similar to OPA when the number of shapes is two. The GPA approach iteratively aligns shapes by registering their corresponding point sets. The algorithm is outlined as follows:

1. Choose a reference shape as an estimate of mean shape.
2. Align all the remaining shapes to the mean shape.
3. Re-compute the mean shape from the aligned shapes.
4. If the Procrustes distance of the two estimated means are above a threshold then continue to step 2.

The estimate of the mean in the GPA method is computed by simply averaging over all the samples, as shown below:

$$\bar{\mathbf{X}} = \frac{1}{N} \sum_{i=1}^N \mathbf{X}_i, \quad (26)$$

where,  $N$  is the number of shapes. This mean is also called the Procrustes mean.

### 3.5.3 Modeling Shape Variations using Principal Component Analysis

After shape alignment, when all the shapes are brought into a common frame of reference, the next step in SSM construction is to find the set of modes that best describe the shape variations within the frame. This is also known as shape decomposition and is usually

performed using Principal Component Analysis (PCA) [94]. The PCA method extracts principal modes which represent data correlation along principal directions within the training data set, eventually reduces problem dimensionality.

Let us consider that there are  $N$  training shapes where each of the shape has a vector of the form  $\mathbf{X}_i = (x_{i1}, \dots, x_{ik})$  which is composed of  $k$  points of dimension  $d$ . The mean of the training data set is computed using equation (26). The corresponding  $dk \times dk$  covariance matrix  $\Sigma_X$  can be written as in (27).

$$\Sigma_X = \frac{1}{N-1} \sum_{i=1}^N (\mathbf{X}_i - \bar{\mathbf{X}}) (\mathbf{X}_i - \bar{\mathbf{X}})^T. \quad (27)$$

The PCA method aims to find an orthogonal matrix  $M$  such that the following linear transformation holds (28),

$$\mathbf{Y} = \mathbf{M}\mathbf{X}, \quad (28)$$

where,  $M$  is an orthonormal matrix. The mean of  $Y$  can be expressed as  $\bar{\mathbf{Y}} = \mathbf{M}\bar{\mathbf{X}}$  and the covariance of  $\mathbf{Y}$  is given by (29):

$$\Sigma_Y = \frac{1}{N-1} \sum_{i=1}^N (\mathbf{Y}_i - \bar{\mathbf{Y}}) (\mathbf{Y}_i - \bar{\mathbf{Y}})^T = \mathbf{M} \Sigma_X \mathbf{M}^T. \quad (29)$$

The detailed derivation of (29) can be found in [94]. Further manipulation of (29) yields:

$$\mathbf{M}^T \Sigma_Y = \Sigma_X \mathbf{M}^T. \quad (30)$$

By substituting  $\mathbf{M}^T = \boldsymbol{\phi}$  we get the following linear relation:

$$\Sigma_X \boldsymbol{\phi} = \boldsymbol{\phi} \Sigma_Y, \quad (31)$$

where  $\boldsymbol{\phi} = \{\boldsymbol{\phi}_1, \boldsymbol{\phi}_2, \dots, \boldsymbol{\phi}_m\}$  is the eigenvector of  $\Sigma_X$ .

Using the transformation of (31), any observation  $\mathbf{X}_i \in \mathbb{R}^m$  can be defined in a new basis  $\{\boldsymbol{\phi}_i\}$  as a new vector  $\mathbf{Y}_i \in \mathbb{R}^m$  and vice versa. Each  $\boldsymbol{\phi}_i$  represents a principal mode or principal axis of variation within the training data set.

The rows of  $\mathbf{M}$  are the eigenvectors of  $\mathbf{\Sigma}_X$  and the diagonal matrix of the covariance of transformed shapes represents the eigenvalues [94]. In the case of correlated points where the smallest eigenvalues are very close to zero, the corresponding eigenvectors are omitted. As a result, the dimensionality of  $\mathbf{M}$  will be reduced. There are several benefits of this dimensionality reduction: (1) the complexity of the SSM model is reduced; (2) this reduction helps to filter out possible noise present in the data, (3) while also improving efficiency of the algorithm in terms of speed and memory.

The computation of PCA is done by an eigenvalue decomposition (EVD) of  $\mathbf{\Sigma}_X$ . Eigenvectors are sorted according to the magnitude of eigenvalues in the decreasing order so that  $|\lambda_i| > |\lambda_{i+1}|$ , where  $\lambda_i$ 's represent eigenvalues. Any sample shape can be approximated by the linear combination of first  $c$  modes using equation (32).

$$\mathbf{X} = \bar{\mathbf{X}} + \sum_{t=1}^c b_t \boldsymbol{\phi}_t, \quad (32)$$

where  $\mathbf{b}_t$  are the PCA model parameters that control the scaling of each eigenvectors and  $c$  is chosen so that the accumulated variance reaches a certain ratio of total variance. An infinite number of shapes can be defined by modifying the scalar weights  $\mathbf{b}_t$ . However, to ensure the variations of the new shapes are within the training data set, each  $\mathbf{b}_t$  is constrained to lie within  $[-3\lambda_t, 3\lambda_t]$ .

### 3.6 Registration in Medical Imaging

Image registration is the process of determining the spatial transformation or mapping that relates the positions in one image to corresponding positions in other image(s). Basically, the registration process geometrically aligns different images for the purpose of integrating useful information obtained from those images. In many cases, registration needs to be done for images

taken at different times, using multiple imaging modalities such as MR, CT, PET, and SPECT, possibly in conjunction with longitudinal imaging studies of a subject carried out at many points in time.

There are three categories of registration based on agreement between images: (1) image-to-image, (2) model-to-model and (3) model-to-image. Image-to-image registration methods directly compare voxel intensities rather than derivative features. Model-to-model registration methods align images by matching features and then minimize the distance between those features. Model-to-image registration methods register a model which is extracted from one image and then registers it with another image.

In general, the registration between two images, say  $A$  and  $B$ , can be represented by the following equation [106]:

$$\mathbf{p}_A = T(\mathbf{p}_B), \quad (33)$$

where  $\mathbf{p}_A = (x_A, y_A, z_A)$  and  $\mathbf{p}_B = (x_B, y_B, z_B)$  are the points of the coordinate systems of  $A$  and  $B$ . Image registration aims to find the transformation  $T$  that maximizes the similarities between images  $A$  and  $B$ . The basic stages involved in image registration are: (1) The choice of the transformation model which specifies how the source image needs to be transformed to match the target image, (2) a similarity measure of how well the two images match, and (3) the optimization process that maximizes the measure of similarity.

The transformation model, denoted by  $T$  in (33), defines how image features can be moved relative to one another to get the optimal mapping between the images. This transformation is performed between images of the same anatomy acquired from either different modalities or from same modalities at different times. Based on the transformation model, image registration can be classified as rigid-body and non-rigid-body transformations. In rigid-body

transformation, the images are rotated and translated with respect to one another to achieve correspondence. This transformation is described by 6 (3 translation and 3 rotation) parameters and can be expressed as:

$$B = \mathbf{R}_{AB}A + \mathbf{t}_{AB}, \quad (34)$$

where  $\mathbf{R}_{AB}$  and  $\mathbf{t}_{AB}$  are the rotation and translation parameters, respectively, both of which need to be minimized to get the correspondence between images  $A$  and  $B$ . An affine transformation is a generalization of a rigid transformation based on 12 parameters: 3 scaling and 3 shearing parameters in addition to the previous 6.

Non-rigid transformations are adopted where target needs to be deformed to perform the mapping. Piecewise polynomial functions such as thin-plate splines [107] and B-Splines [108] are commonly used to perform non-rigid transformation. In such cases minimization of interpolation functions are used to model the transformation. Deformable model-based registration also performs non-rigid transformation which is discussed in Section 3.6.2.

### 3.6.1 Similarity Measures in Registration

Efficient registration between images depends largely on choosing the appropriate similarity measure. First category of similarity measures are based on the image features where the goal of the registration is to maximize the similarity between these features. An image is represented using identifiable elements called *features* or *landmarks*. Commonly used features in image registrations are points, curves, and regions. Point landmarks are either chosen based on anatomical or geometrical significance such as extrema of curvature [109].

Curves have also been used as geometric features for medical image registration in [111] and [112]. Specifically, ridges or crest lines of the brain (like gyri and sulci) which are



meaningful anatomical features, are extracted from different brain images and then registered to each other [113, 114]. Region features refer to areas with homogeneous characteristics.

The second broad category of similarity measure is based on voxel intensity. Intensity based approaches work by matching mathematically or statistically defined image patterns over local neighborhoods, in a manner that is repeated over the whole image. In these cases, similarity measures are computed over local neighborhoods and aggregated over the source or target image, which leads to a putative transformation that is adjusted until the similarity is maximal.

Some of the commonly used similarity measures are Sum of Squared Differences (SSD), Correlation Coefficient (CC), Correlation Ratio (CR), Mutual Information (MI) and Normalized Mutual Information (NMI). SSD and CC are suitable for mono-modal registration (images from same modality having similar intensity patterns). On the other hand, CR, MI and NMI are appropriate measures for multimodal registration where the source and target images arise from different modalities. MI-based registration measures the joint probability of the corresponding voxel intensity of the two images and then maximizes this measure in a manner such that the amount of information they contain about each other is maximal. A thorough review of MI-based registration techniques is given in [115].

The third step of the registration process is to select the optimizer, which will maximize or minimize the transformation model to improve image similarity. The choice of the optimization method depends on: a cost function, the transformation model, the required registration accuracy and a time constraint. Optimization of the registration process has been solved using standard algorithms such as the Simplex method, the Powells method, and the Steepest Gradient Descent method. These algorithms are described in details in [116].

### 3.6.2 Deformable model based registration

Image registration based on deformable models, which is categorized as a model-to-image registration, is a well-researched field in medical image analysis. In this approach, a model is used as a set of geometric features that is deformed iteratively using external and internal forces. In deformable models, segmentation and registration processes are typically combined. The choice of the deformable model plays a governing role in this type of registration. Different deformable models are discussed in Section CHAPTER 3. In this section, we will emphasize on how the registration process works for deformable models. Sotiras et al. presented a recent detailed survey on deformable model registrations in medical imaging [117].

Rueckert et al. [118] presented a popular B-Spline based a non-rigid registration technique for 3D contrast-enhanced breast MRI. The transformation model consisted of global and local motions where the global motion was modeled using an affine transformation and a local motion is modeled by Free Form Deformation (FFD). The basic idea behind spline-based FFD is to deform an object based on a local deformation polynomial that is anchored by the motion of its underlying mesh control points, which eventually results in a  $C^2$ -continuous transformation (a transformation whose first and second derivatives are continuous). In Rueckert's work, the image-to-image registration is performed by maximizing the normalized mutual information between two images. Wang et al. [119] published a non-rigid registration of the brain which was modeled by a FFD-based Non-Uniform Rational B-Spline (NRRBS) and demonstrated better flexibility and performance.

Balci et al. [120] incorporated an FFD-based B-Spline in a groupwise registration technique. Groupwise registration techniques are advantageous for characterizing anatomical shape differences among the subjects of a population. Miller et al. developed a groupwise

registration method where the joint correspondence of the population images is computed by minimizing the summed voxel-wise entropies. Groupwise registration have been used recently in [121] to construct a longitudinal atlas of the human brain, and in [122] which combines structural information from the segmentation method into the registration.

### 3.6.3 Tubular Model Registration

This section covers the state of the art for tubular or vascular model registration. Aylward et al. [123] presented a model-to-image registration technique for the purpose of rigidly aligning images of tubes. The models of the tubes were produced from a dynamic-scale, ridge-based segmentation approach [76]. This segmentation results in the estimation of centerlines and radii of the blood vessels, which is discussed in Section 3.2.2. The rigid transformation from source to target coordinate system was achieved using (35):

$$\mathbf{y} = \mathbf{x}\mathbf{R} + \mathbf{t} . \quad (35)$$

Here  $\mathbf{x}$  is a point in the source image,  $\mathbf{y}$  is a point in the target image,  $\mathbf{R}$  is the rotation matrix and  $\mathbf{t}$  is the three-dimensional translation vector. The registration process optimizes  $\mathbf{R}$  and  $\mathbf{t}$  simultaneously by maximizing the metric function given in (36):

$$F(\mathbf{R}, \mathbf{t}) = \frac{1}{\sum_{i=1}^n w_i} \sum_{i=1}^n w_i I_{\kappa\sigma_i}(\mathbf{x}_i\mathbf{R} + \mathbf{t}), \quad (36)$$

where the subscript  $\kappa\sigma_i$  is the scaling of the image  $I$ ,  $w_i$  is the weight factor of the centerline point  $\mathbf{x}_i$ . Essentially, maximizing (36) resulted in a mapping of bright image points with the model centerline points. The authors used a two-phase coarse-to-fine optimization method involving the gradient descent direction line search algorithm.

Jomier and Aylward [124] further extended the rigid model-to-image registration by computing an elastic transformation in a hierarchical manner. After performing a global and

piecewise registration to align the vascular model with the target image, a non-rigid registration was performed to constrain the elasticity and rigidity of the tube.

Noble and Dawant [79] developed an elastic atlas-based segmentation method where they used both rigid and elastic transformations for inter-modal MR and CT image registration. To create the atlas for the optic nerve and chiasm, a pair of MR and CT images is registered using a rigid transformation. Then the atlas and training population are registered using a non-rigid intensity-based adaptive algorithm by maximizing Normalized Mutual Information.

### **3.7 Conclusion**

3D tubular structure segmentation is one of well-researched area in medical image analysis. However, there is a scarcity of segmentation algorithm applied to cranial nerves. This chapter presents current state-of-the-art algorithms for vessel segmentation. We have emphasized on deformable model-based segmentations, Hessian-based segmentations and Minimal Path-based segmentations as our proposed segmentation algorithm is built exploiting these concepts. This chapter also provides a brief literature review on the published nerve segmentation algorithms which includes optic nerve and spinal nerve.

The use of a priori knowledge in vessel segmentation is often crucial in terms of robustness and accuracy. Basic concepts of constructing a SSM are detailed including OPA, GPA and PCA methods. Deformable models perform a coupled segmentation-registration process. Brief discussions on the state-of-the art deformable model-based registration algorithms as well as other existing vascular registration techniques are presented.

## CHAPTER 4

### CENTERLINE EXTRACTION AND SURFACE MODELING

In this chapter, we present a segmentation technique to identify the medial axis and the surface boundary of cranial nerves. We utilize a 3D deformable 1-Simplex discrete contour model to extract the medial axis of each cranial nerve. This contour model represents a collection of 2-connected vertices linked by edges, where vertex position is determined by a Newtonian expression for vertex kinematics featuring external and internal forces, the latter of which include attractive forces towards the nerve medial axis. We also exploit multiscale vesselness filtering and Minimal Path techniques in the medial axis extraction method, which computes a radius estimate along the path. Once we have the medial axis and the radius function of a nerve, we identify the nerve surface using a 2-Simplex deformable model, which expands radially and can accommodate any nerve shape. As a result, the method proposed here combines the benefits of explicit contour and surface models, while also achieving a cornerstone for future work that will emphasize shape statistics, static collision with other critical structures and tree-shape analysis.

Although the 2-Simplex mesh has been used for surface representation and segmentation in the literature, the 1-Simplex mesh has not been implemented for the segmentation of curvilinear structures. Delingette [29] alluded to 1-Simplex geometry in his publications, but never implemented it with a Newtonian, image-based model. In this chapter, we present a cranial nerve segmentation technique that utilizes 1-Simplex-based discrete active contour model of the intracranial nerve centerlines, which exploits vesselness-based image forces, as well as 2-Simplex-based nerve surface segmentation that identifies the nerve boundary using gradient-based image forces.

The rest of the chapter is organized as follows: Section 4.1 illustrates different steps of the centerline extraction pipeline. Section 4.2 describes the nerve surface segmentation process. Results and validation of both centerline identification and surface segmentation are presented in Section 4.3 and Section 4.4, respectively.

#### 4.1 Centerline Identification

We designed an image analysis pipeline that ends up with the extraction of the nerve centerlines from patient-specific T<sub>2</sub>-weighted MRI data. This centerline extraction pipeline, as shown in Fig. 14, can be sub-divided into four main steps: image preprocessing, computation of the geodesic path between two user-provided end points, construction of a 1-Simplex 3D contour, and 3D contour deformation.

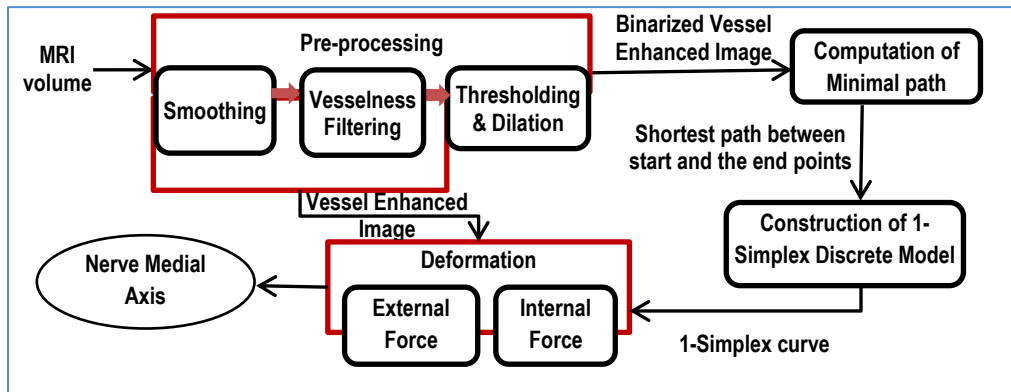


Fig. 14 . Centerline Extraction Pipeline.

#### 4.1.1 Preprocessing

The raw MR image undergoes the following preprocessing techniques: Gaussian smoothing, vesselness computation and binary thresholding. Image smoothing is performed by convolving the image with a Gaussian kernel, as shown in (37).

$$G(x, y, z) = \frac{1}{\sigma\sqrt{2\pi}} \exp\left(-\frac{(x^2+y^2+z^2)}{2\sigma^2}\right), \quad (37)$$

where  $\sigma$  is the std. deviation of the Gaussian distribution.

Subsequently, a vesselness operator, as shown in (11) and (12), identifies locally tubular portions of the image coinciding with voxels characterized by the local Hessian matrix having one near-zero eigenvalue [70]. The Hessian encodes the local principal directions of the intensity ridges, which enables detection of blood vessels from angiographic images. A permissive vesselness threshold and the morphological dilation of the binarized image enable us to restrict the subsequent medial axis computation to a sub-volume of interest while still making allowances for partial volume effects.

#### 4.1.2 Computation of the Minimal Path

The centerline, aka medial axis, extraction technique is a semi-automatic process that requires the user to input two terminating points coinciding with the start and the end of each nerve. We compute a Minimal Path that links these points, which serves as a putative estimate of the medial axis of the nerve. This computation determines a path between two points similarly to Deschamps' Fast Marching technique [63]. This geodesic path between two points can be found by globally minimizing a cost functional that is defined in terms of the image-derived "speed function". This is a real-valued function on the image domain characterized by a high-valued vesselness measure on nerve voxels. A moving front evolves from the beginning seed point and

ultimately concludes when the front arrives at the ending seed point. The Minimal Path is determined by back-propagating from the ending position to the starting position.

#### 4.1.3 Geometry and Construction of 1-Simplex Contour

The medial axis of each nerve will be identified and discretized using a 1-Simplex model. The continuous path is discretized as a curvilinear aggregate of vertices linked by edges, and this piecewise-linear curve is endowed with the ability to deform according to the equation (5). The curve model presented below exploits the same geometric definitions as elaborated by Delingette [29].

A 1-Simplex is a piecewise-linear curve where each non-terminating vertex has two vertex-neighbors as depicted in Fig. 15(a). The geometrical measurements defined at a 1-Simplex vertex are defined in terms of the Frenet frame, which features tangent  $\mathbf{t}_i$ , normal  $\mathbf{n}_i$  and bi-normal  $\mathbf{b}_i$  vectors at that vertex, as also shown in Fig. 15(a). The relation between the unit tangent and the unit normal around a vertex  $\mathbf{P}_i$  is established using the unit bi-normal vector, expressed in equations (38), (39) and (40).

$$\mathbf{t}_i = \frac{\mathbf{P}_{i+1} - \mathbf{P}_{i-1}}{\|\mathbf{P}_{i+1} - \mathbf{P}_{i-1}\|} \quad (38)$$

$$\mathbf{b}_i = \frac{(\mathbf{P}_i - \mathbf{P}_{i-1}) \wedge (\mathbf{P}_{i+1} - \mathbf{P}_i)}{\|(\mathbf{P}_i - \mathbf{P}_{i-1}) \wedge (\mathbf{P}_{i+1} - \mathbf{P}_i)\|} \quad (39)$$

$$\mathbf{n}_i = \mathbf{b}_i \wedge \mathbf{t}_i . \quad (40)$$

We can uniquely define each vertex of a 1-Simplex mesh as a linear combination of its two direct neighbors using two metric parameters ( $\varepsilon_{1i}$  and  $\varepsilon_{2i}$ ) and two angular parameters ( $\phi_i$  and  $\psi_i$ ) as depicted in Fig. 15 (a). In particular, a vertex  $\mathbf{P}_i$  can be expressed as the vector sum [125] represented as in (41):



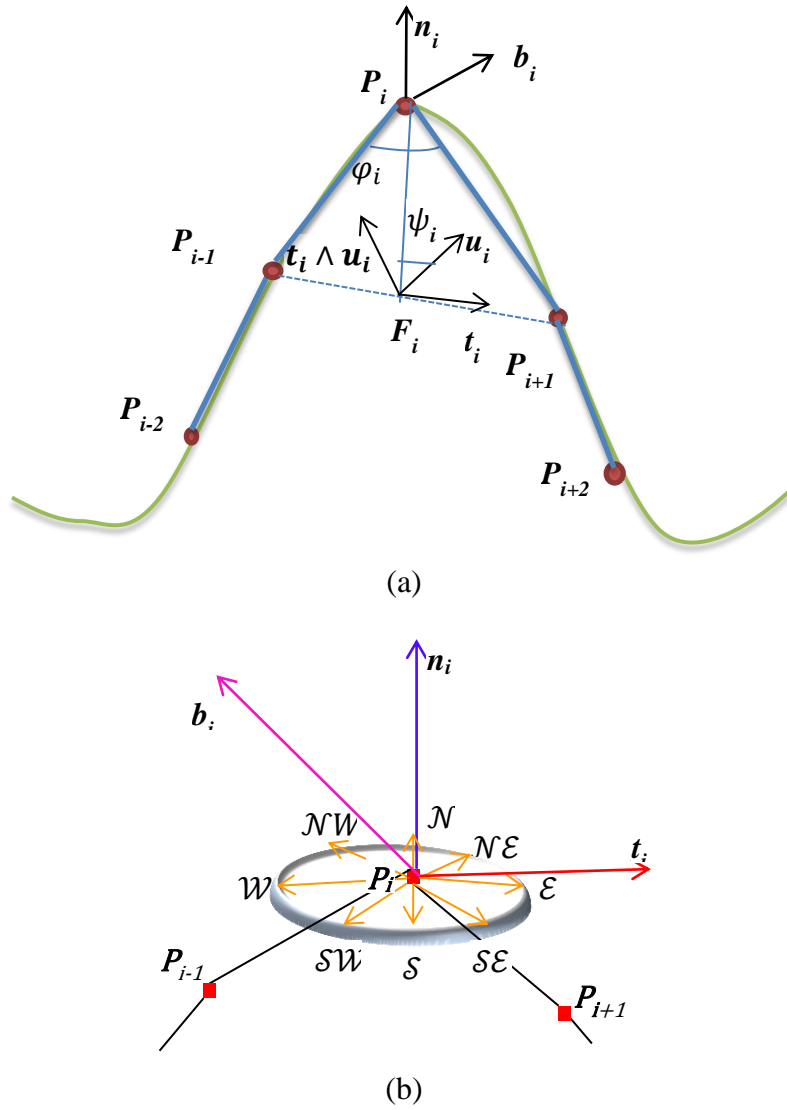


Fig. 15. 1-Simplex geometry. (a) A 1-Simplex curve overlaid with the Frenet frame defined at vertex  $P_i$ , depicted with its discretized geometry at  $P_i$ . (b) Search strategy at the 1-Simplex vertex  $P_i$  in the normal-binormal plane with all the eight search directions.

$$\mathbf{P}_i(\epsilon_{1i}, \epsilon_{2i}, \psi_i, \phi_i) = \epsilon_{1i}\mathbf{P}_{i-1} + \epsilon_{2i}\mathbf{P}_{i+1} + h(\phi_i)\mathbf{n}(\psi_i). \quad (41)$$

The vertices  $\mathbf{P}_{i-1}$  and  $\mathbf{P}_{i+1}$  are the two vertex-neighbors of  $\mathbf{P}_i$ , while  $\epsilon_{1i}$  and  $\epsilon_{2i}$  are the metric parameters,  $\mathbf{n}(\psi_i)$  is the local normal within the curve's normal plane, and  $h(\phi_i)$  is the height function. The latter two depend on the two angular parameters  $\psi_i$  and  $\phi_i$  respectively. The two metric parameters  $\epsilon_{1i}$  and  $\epsilon_{2i}$  must sum to 1. The Simplex angle  $\phi_i$  is the angle between two consecutive segments  $[\mathbf{P}_{i-1} \mathbf{P}_i]$  and  $[\mathbf{P}_i \mathbf{P}_{i+1}]$ . The other angular parameter  $\psi_i$  is defined on the basis of *second-order tangency*, which is characterized by the *osculating plane*, formed by the *curve tangent* and the *acceleration* vector defined at a point (vertex) [126], and by the *normal plane* spanned by the binormal and the acceleration vectors. A curve has an infinite number of normal vectors defined at a given point; however there is only one normal vector contained in this normal plane, which is defined by the vector  $\mathbf{u}_i$ , as shown in Fig. 15(a) and described in (42):

$$\mathbf{u}_i = \frac{\mathbf{t}_i \wedge ((\mathbf{P}_{i-1} - \mathbf{P}_{i-2}) \wedge (\mathbf{P}_{i+2} - \mathbf{P}_{i-1}))}{\|\mathbf{t}_i \wedge ((\mathbf{P}_{i-1} - \mathbf{P}_{i-2}) \wedge (\mathbf{P}_{i+2} - \mathbf{P}_{i-1}))\|}. \quad (42)$$

The parameter  $\psi_i$  represents curve differential geometry based on second-order tangency and equates with the angle between  $\mathbf{u}_i$  and the normal  $\mathbf{n}_i$ . The normal  $\mathbf{n}(\psi_i)$  is estimated through  $\psi_i$  as expressed as (43) [125]:

$$\mathbf{n}(\psi_i) = \cos(\psi_i)\mathbf{u}_i + \sin(\psi_i) \mathbf{t}_i \wedge \mathbf{u}_i. \quad (43)$$

Finally, the height function, defined from the projection (or foot)  $\mathbf{F}_i$  of  $\mathbf{P}_i$  on the segment  $[\mathbf{P}_{i-1}, \mathbf{P}_{i+1}]$  is given by the expression as (44) :

$$h(\phi_i) = \frac{r_i(-1 + \epsilon \sqrt{1 + 4 \epsilon_{1i} \epsilon_{2i} \tan^2 \phi_i})}{2 \tan \phi_i}, \quad (44)$$

where  $r_i$  is half the distance from  $\mathbf{P}_{i-1}$  to  $\mathbf{P}_{i+1}$ .

#### 4.1.4 Deformation of the 1-Simplex Contour

After the discretization of the minimal continuous path between two terminal points coinciding with the 1-Simplex initialization, what comes next is the Newtonian deformation of the 1-Simplex model to have it conform to the medial axis of the nerve. We define external and internal forces to constrain the contour deformation towards the actual medial axis while preserving internal properties such as continuity. The kinematics of each vertex is controlled through the Newtonian model described in (5). We implement two internal forces, both described by Delingette but not implemented in the 1-Simplex model [29]: a tangential force that concentrates vertices in portions of high curvature and a Laplacian force that ensures curve smoothing by enforcing  $C^1$  continuity. These are defined in expressions (45) and (46), respectively:

$$\mathbf{F}_{Tangent} = (\tilde{\epsilon}_{1i} - \epsilon_{1i})\mathbf{P}_{i-1} + (\tilde{\epsilon}_{2i} - \epsilon_{2i})\mathbf{P}_{i+1} \quad (45)$$

$$\mathbf{F}_{Laplacian} = \frac{1}{2}(\mathbf{P}_{i-1} + \mathbf{P}_{i+1}) - \mathbf{P}_i . \quad (46)$$

The external Newtonian force of the model is employed to nudge the curve towards the points that have a high likelihood of lying along the medial axis of the tube. We exploit the *vesselness* function, described in Section 3.2.1 to extract this high-centeredness information. The vesselness filter gives the maximum intensity value at the center of a vessel [70].

For the sake of computing the external force  $F_{ext}$  at a vertex, we perform a search for the voxel possessing the greatest vesselness value in the plane spanned by the normal and binormal vectors as depicted in Fig. 15 (b). This search is performed along four directions in this plane, which we can label North-N, South-S, East-E, West-W, and the four directions midway between those: NE, SE, NW, and SW. We sample with a specified step size in each direction to find the

smallest offset. This small offset is eventually used to minimize the distance between the 1-Simplex curve's vertex and the voxel having the highest vesselness value in the image.

## 4.2 Nerve Surface Generation

In this section, we have elaborated the process of cranial nerves' boundary surfaces generation. In the first step, we have estimated nerves' radius at each discrete vertices of the 1-Simplex centerline which is detailed in Section 4.2.1. In the following step, the 2-Simplex based deformable surface boundary is constructed (Section 4.2).

### 4.2.1 Radius Estimation

In general, tubular surfaces can be segmented using tube medial axes in addition to tube semi-axis or radius information. We employ Frangi's multiscale vesselness filtering to estimate the radius at each vertex of the contour [127]. The vesselness filter of equation (11) is measured using a range of radius or scale as expressed in (47). The filter's response is maximal at a scale that matches the vessel size. This scale is recorded as the vessel width of the medial axis vertex.

$$V(\mathbf{x}) = \max_{\sigma_{min} \leq \sigma \leq \sigma_{max}} V(\mathbf{x}, \sigma), \quad (47)$$

where  $\sigma_{min}$  and  $\sigma_{max}$  are minimum and maximum vessel width, respectively.

The process of 3D surface generation is depicted in Fig. 16 using a 3D synthetic tube image. User-specified seed points are shown in green dots in Fig. 16(a) through which the MP is computed in Fig. 16 (b) as shown in red contour. The MP is then deformed using 1-Simplex to get the actual medial axis of the tube as shown Fig. 16 (c) with the green contour. We estimate the radius of a nerve at each point of the 1-Simplex medial axis model using Frangi's multiscale

approach. A triangulated 3D surface model is then generated using the medial axis and radius information depicted in Fig. 16 (d).

#### 4.2.2 2-Simplex-based Nerve Boundary Surface Generation

2-Simplex deformable models can be used to segment 3D surfaces from medical images. Each vertex of a 2-Simplex mesh has a constant 3-connectivity and can be represented as the linear combination of neighbors like the 1-Simplex mesh.

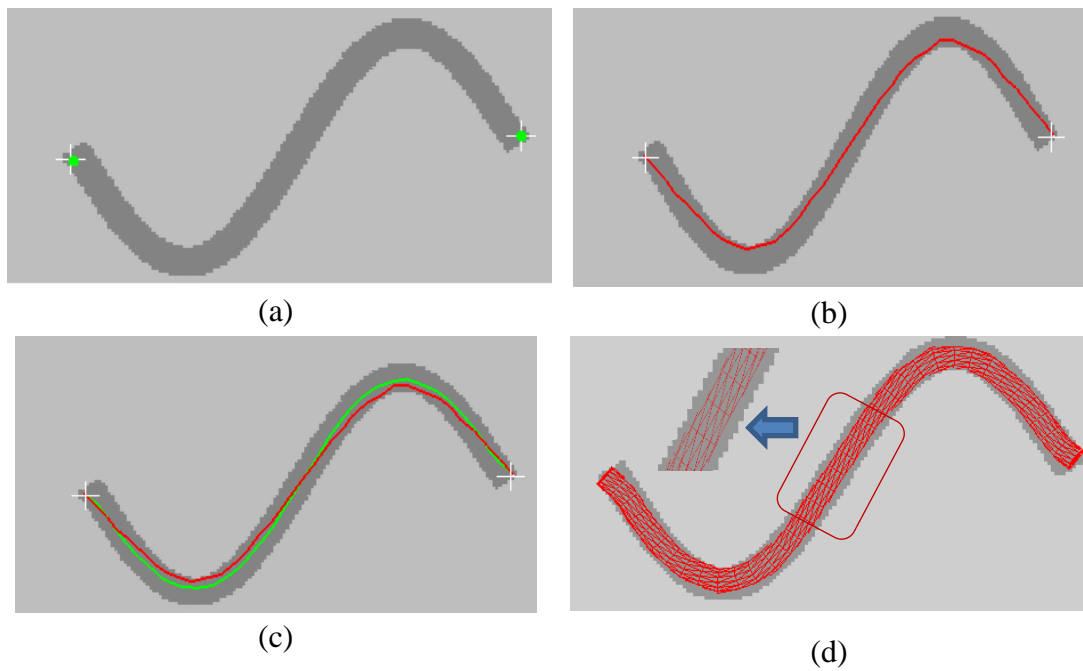


Fig. 16. A step by step segmentation process of synthetic nerve surface; (a) user-initialized start and end points on a axial slice of the synthetic image volume; (b) geodesic path (the red curve) between start and end point using front propagation (c) medial axis computation (green curve) by deforming the 1-Simplex discretization of the geodesic path; (d) triangular nerve surface; the inset picture shows the under-segmentation result.

The 2-Simplex mesh has the property of topological duality to the triangular mesh. We convert the initial triangular surface constructed from the medial axis and the radius into a 2-Simplex mesh. The conversion process works by computing the centroids of each triangle of the triangular mesh, coinciding with the vertices of the 2-Simplex mesh, and then linking these centroids to produce edges of the 2-Simplex mesh as shown in Fig. 17 (a). To perform this conversion the triangle mesh should be watertight and 2-manifold.

The problem associated with this approach is that the computed surface model might be underestimated depending on the initialization of maximum and minimum scale ( $\sigma_{min}$  and  $\sigma_{max}$ ) of the multiscale filter as depicted in Fig. 17 (b). To improve the accuracy of nerve boundary segmentation, the converted 2-Simplex mesh is used to initialize the 2-Simplex deformation process. The result after the deformation is shown in Fig. 17 (c). Similar to the 1-Simplex mesh, the 2-Simplex mesh follows the same Newtonian model shown in (5).

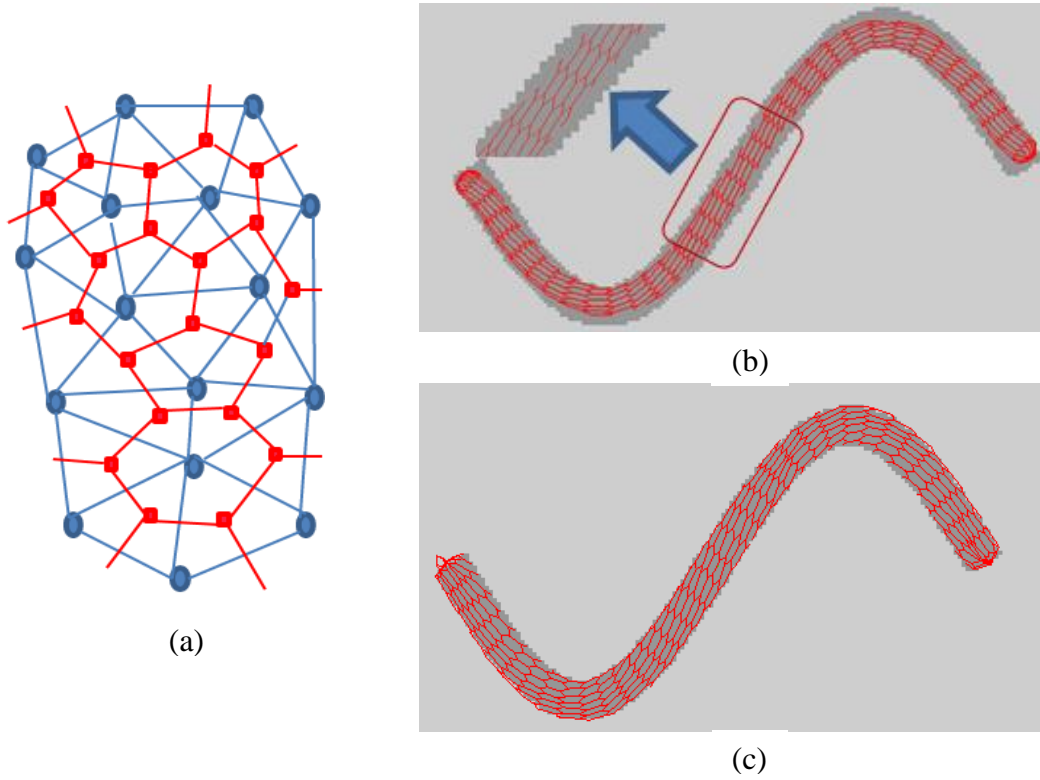


Fig. 17. 2-Simplex mesh surface segmentation; (a) Conversion between the triangle and 2-Simplex mesh using topological duality; (b) Converted 2-Simplex mesh from the triangular mesh of Fig. 16 (d); (c) 2-Simplex mesh after deformation shown as wireframe nerve model.

The 2-Simplex deformation is also based on equilibrium between Newtonian forces, where the image gradient along the surface normal is used to compute the external force. Internal forces are used to ensure smoothness and continuity as suggested by Delingette [29].

### 4.3 Results

In this section, we have illustrated results of centerline extraction and surface extraction methods. We have applied these algorithms both to synthesized and healthy patient MRI data.

### 4.3.1 Centerline Extraction – Synthetic Data

This section describes the results of centerline extraction algorithm applied to both synthetic and patient MRI data sets. The first validation exercise involves several synthetic images imbedded with tubes of various shapes specified analytically, where we compare the detected medial axes of these tubular digital phantoms against the corresponding analytical expressions for the medial axis considered as the ground truth.

Image intensities of these analytical images range between 0 to 255. We added Gaussian noise, the noise was zero-mean and had a standard deviation of 60. We synthesized isotropic datasets featuring simple arc-shape, sinusoid and helix-shaped tubes. These tubular datasets were sampled at three different voxel spacings: 0.1 mm, 0.5 mm and 1 mm. The radius of each of these tubes was set to 1mm. The arc-shaped and sinusoidal phantom images are shown in Fig. 18 and Fig. 19, respectively. In Fig. 18, the left column images are 3D rendering of the images, the middle column shows the medial axis (green) and ground-truth (red) paths along axial slices. The rightmost column features sagittal curve renderings that illustrate the agreement between the identified medial axis and the ground truth. Fig. 19 illustrates results comparable to Fig. 18 (a)-(c) for the sinusoid digital phantom.

Helix-shaped tube volumes are shown in Fig. 20. For this shape, we created two volumes having isotropic voxel sizes of 0.5mm and 1.0mm each with added noise. The resulting 1-Simplex medial axis curves of the helix-shaped tubes prove that the method can handle high torsion and curvature of 3D tubular objects and can produce  $C^1$ -continuous space curves.



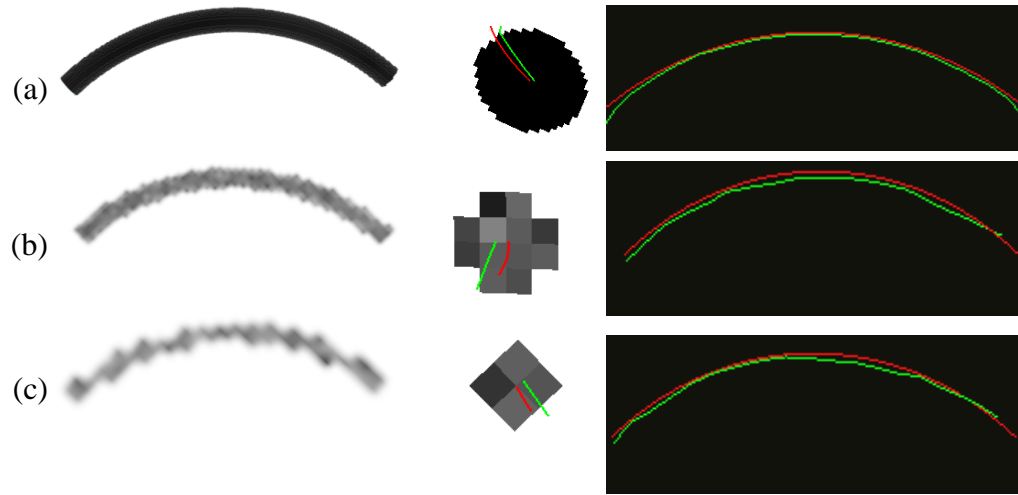


Fig. 18. Results of arc-shaped tubular digital phantom. Image slices of spacing 0.1 mm (Panel a), 0.5mm (Panel b) and 1.0 mm (Panel c) with their corresponding computed (green) and ground-truth medial axes (red). Gaussian noise is added to images of Panel (b) and (c). Images shown at the middle are the sagittal slices of the corresponding image.

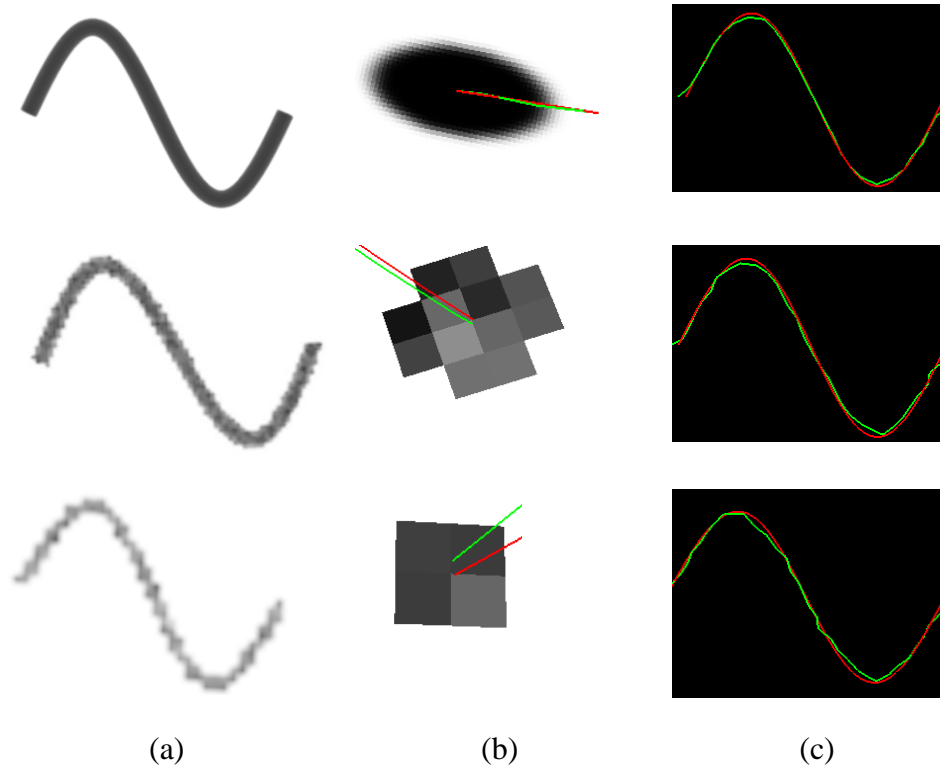


Fig. 19. Results of sinusoidal digital phantom. Image slices of spacing 0.1 mm (Panel a), 0.5mm (Panel b) and 1mm (Panel c) and their corresponding computed (green) and ground-truth medial axes (red).

#### 4.3.2 Centerline Extraction – MRI data

We now apply this medial axis identification to a skull-base MRI data set provided by neuroradiologist Dr. J. Butman of NIH. The main image modality of interest is a Balanced Fast Field Echo (BFFE) sequence of anisotropic slice spacing  $0.3 \times 0.3 \times 0.4 \text{ mm}^3$ , dimension of  $256 \times 256 \times 220$  voxels,  $TR = 5.45 \text{ ms}$  and  $TE = 2.175 \text{ ms}$ .

The end points of the nerves are identified by a neurosurgeon from the Department of Neurosurgery at Children's Hospital of Pittsburgh, which are used as the seed points of the medial axis extraction method. All ten pairs of cranial nerves that are attached to brainstem are identified by our medial axis extraction algorithm as shown in Fig. 21 and Fig. 22, where

column *A* represents the nerves superimposed on MRI slices and column *B* illustrates surface renderings of 3D nerve medial axes.

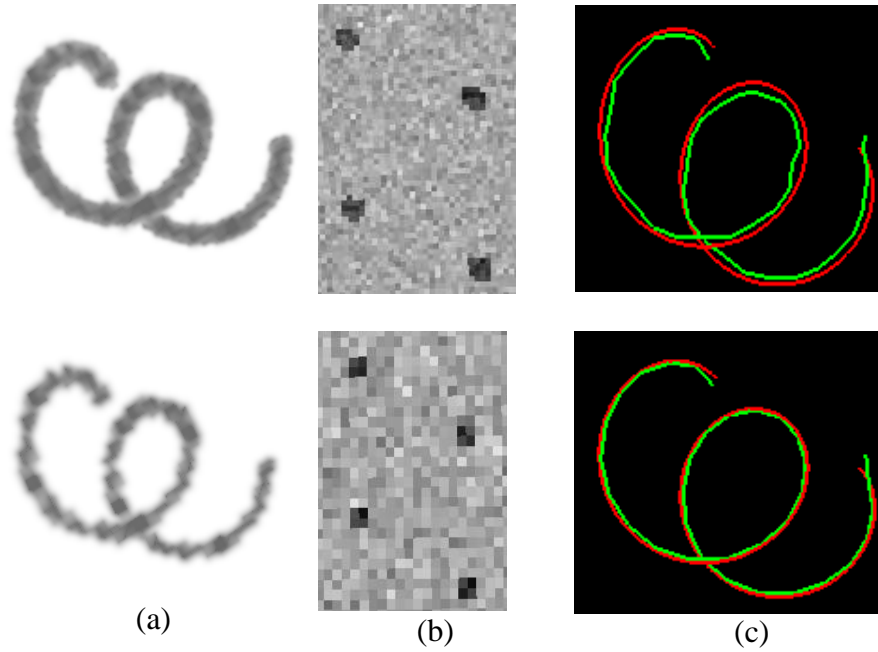


Fig. 20. 3D helix-shaped digital tubular phantom results. Phantom images with Gaussian noise and voxel size of 0.5mm (top row) and 1mm (bottom row). Panel (a) 3D rendering of the volumes, Panel (b) Sagittal image slices, Panel (c) Computed (green) and ground-truth (red) medial axes.

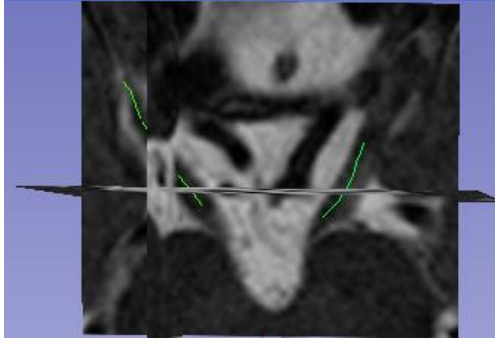
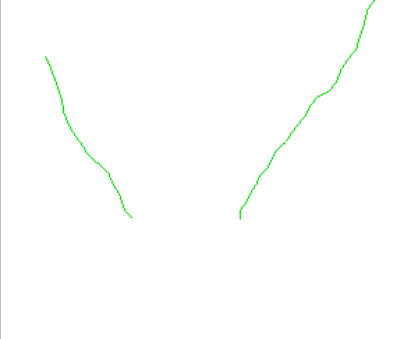
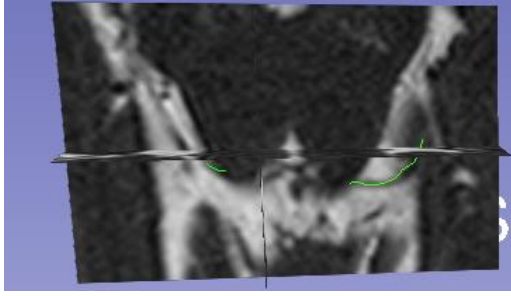

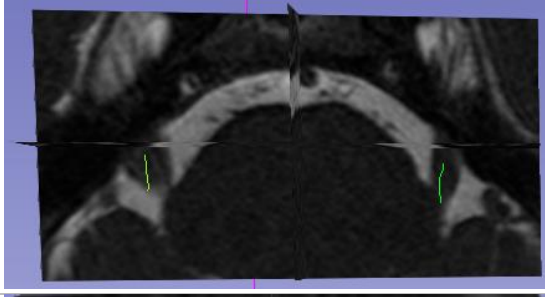
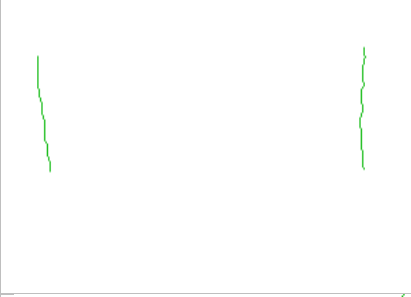
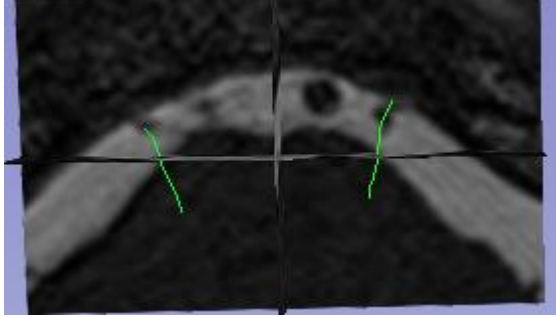
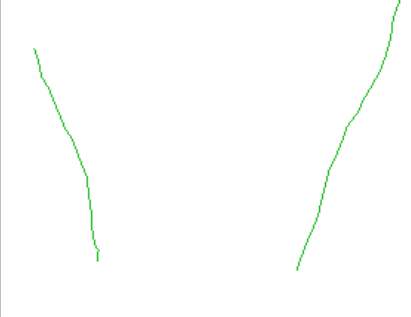
Nerves	Column A	Column B
CNIII		
CNIV		
CNV		
CNVI		

Fig. 21. Centerlines of cranial nerves (CNIII to CNVI) from MR patient data. Column A: nerve medial axes superimposed on tri-planar image, emphasizing the axial plane. 3DSlicer has been used to visualize MR slices; Column B: Extracted 1-simplex medial axis curves of the cranial nerves.

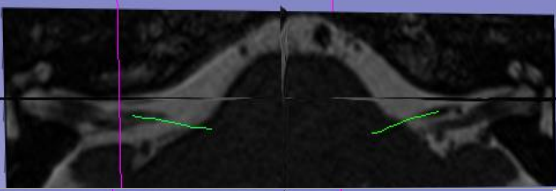

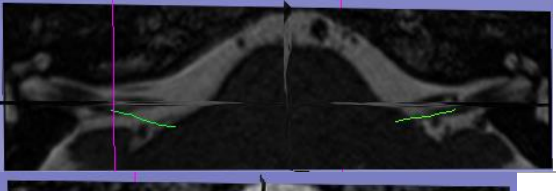
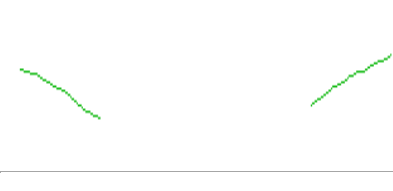
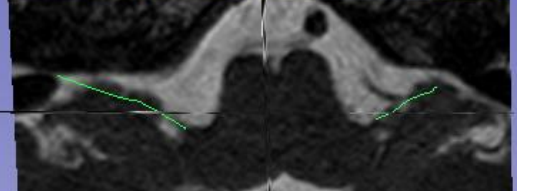
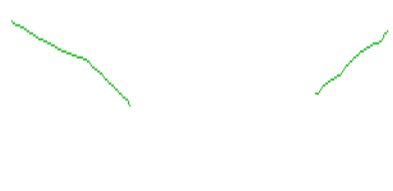
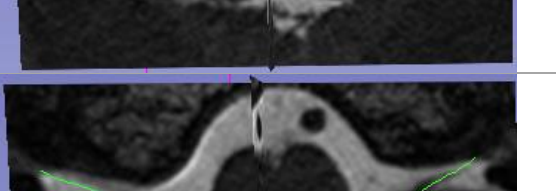

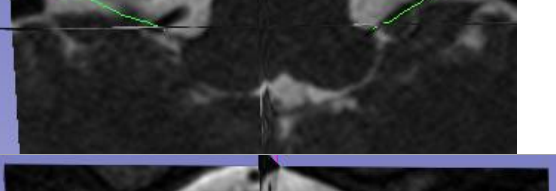
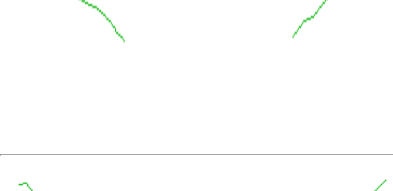
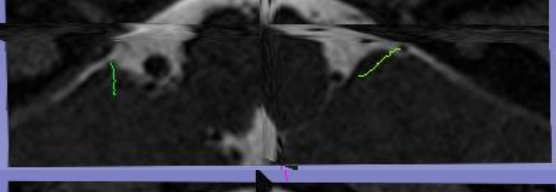

Nerves	Column A	Column A
CNVII		
CNVIII		
CNIX		
CNX		
CNXI		
CNXII		

Fig. 22. Centerlines of cranial nerves (CNVII to CNXII) from MR patient data. Column A: nerve medial axes superimposed on triplanar image, emphasizing the axial plane. 3DSlicer has been used to visualize MR slices ;Column B: Extracted 1-simplex medial axis curves of the cranial nerves.

### 4.3.3 3D Boundary Segmentation

The results of the nerves' boundary segmentation are depicted in Fig. 23 and Fig. 24. Fig. 23 illustrates the evolution of the segmentation process, where the red structures are the initial triangulated surfaces generated from the 1-Simplex medial axes and radii which are superimposed on the corresponding axial MRI slices (Column A); the green surfaces represent the deformed 2-Simplex nerve surfaces (Column B) superimposed on the same MRI slices. Column C shows an overlaid view of the triangulated meshes (red surface) of Column A and 2-Simplex meshes (green wireframe) of Column B. For illustration purposes, we show the initial segmentation models for first three brainstem nerves (CNIII, CNIV and CNV) in Fig. 23, whereas Fig. 24 and Fig. 25 depict the segmented surface models for the ten pairs of brainstem nerves (CNIII to CNXII) where Column A illustrates nerve contours shown in axial planes and Column B shows the 3D rendering of nerves. In each of the slices blue and red color map refer to the highest and lowest intensities, respectively.

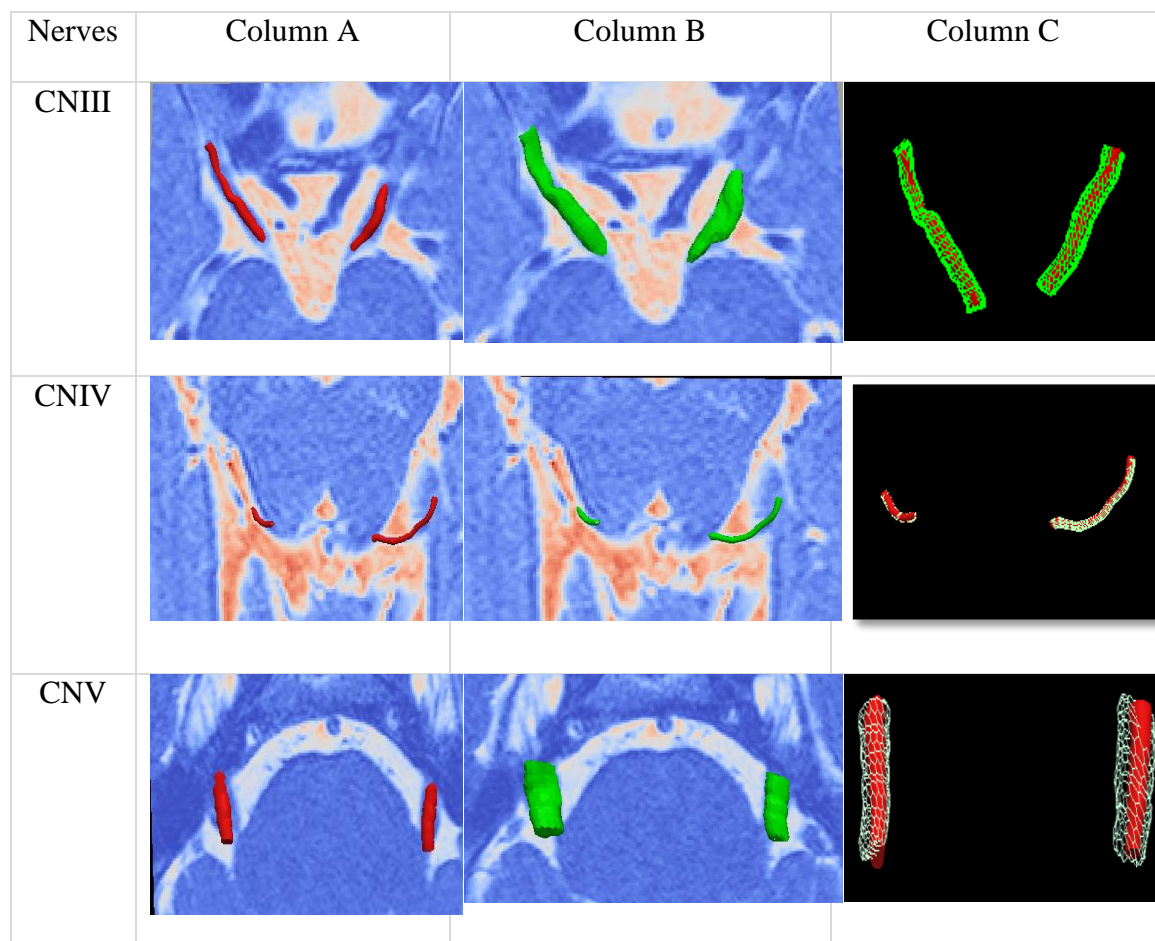


Fig. 23. 3D segmentation of cranial nerves III to V; Column A shows the initial nerve models (red structures); Column B shows the 2-Simplex nerve model after deformation (green structures); Column C shows overlaid model of initial (red surface) and final (green wireframe) segmentation.

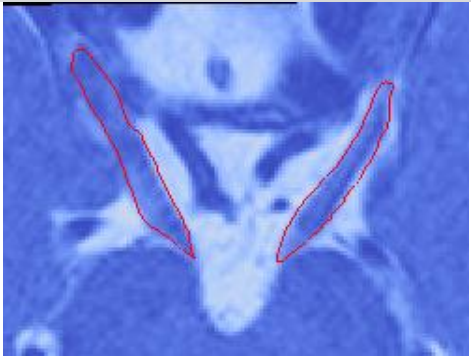
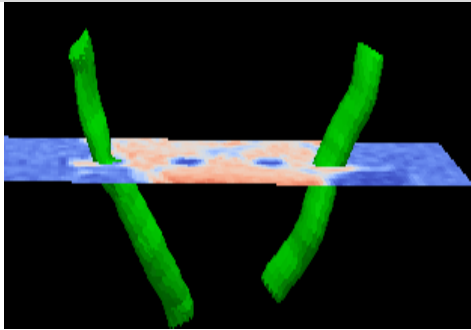
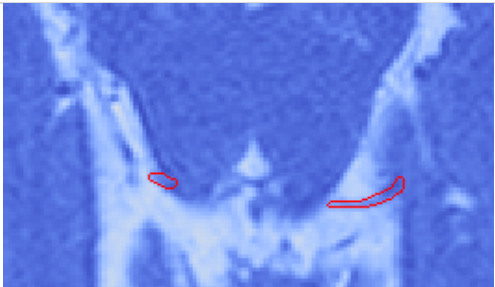
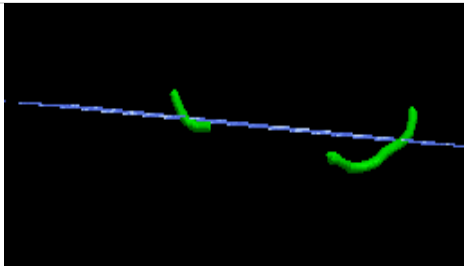
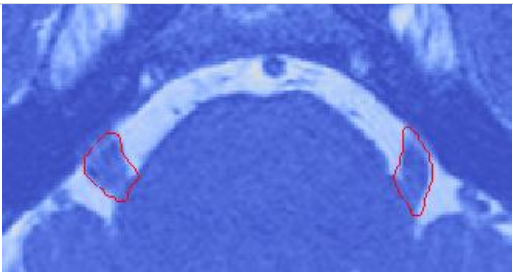
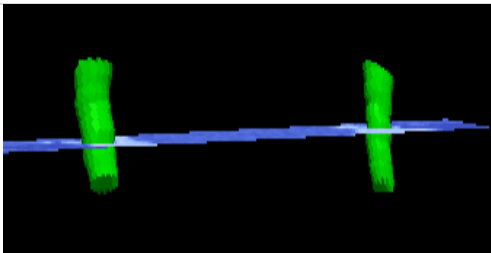
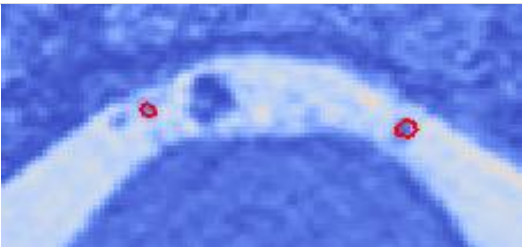
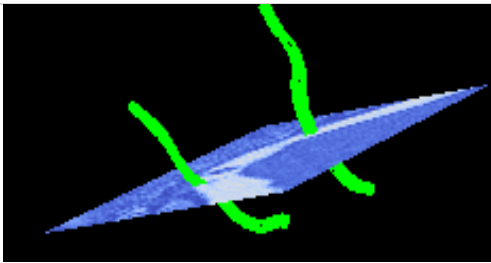
Nerves	Column A	Column B
CNIII		
CNIV		
CNV		
CNVI		

Fig. 24. 3D segmentation of cranial nerves III to VI; Column A: segmentation result is shown in a nerve corresponding axial plane; Column B: rendering of 3D nerve models.




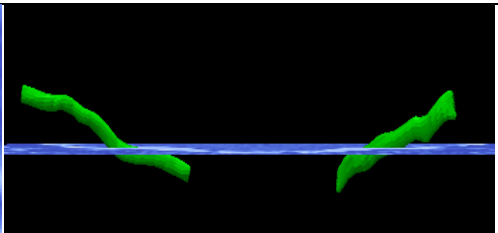

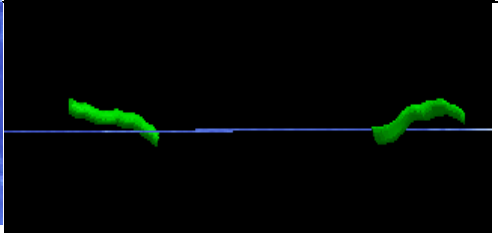
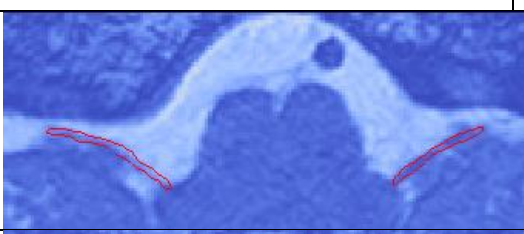
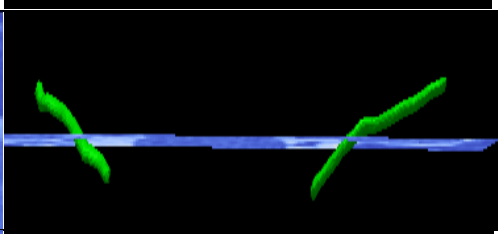
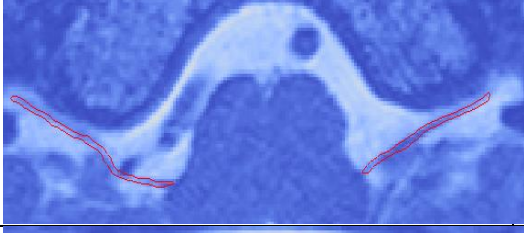
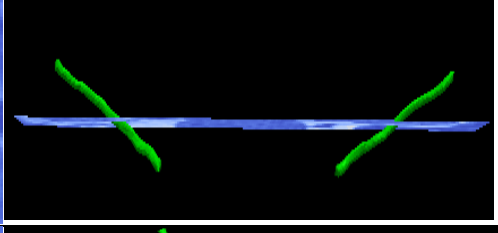

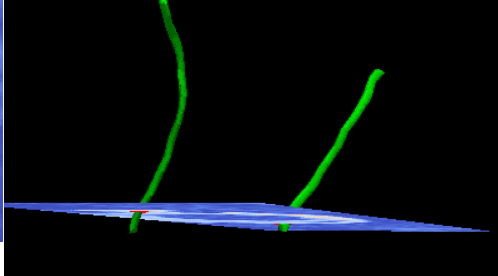
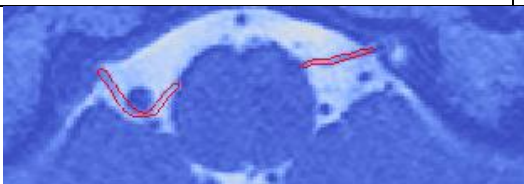
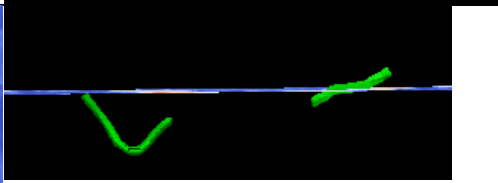
Nerves	Column A	Column B
CNVII		
CNVIII		
CNIX		
CNX		
CNXI		
CNXII		

Fig. 25. 3D segmentation of cranial nerves VII to XII; Column A: segmentation result is shown in a nerve corresponding axial plane; Column B: rendering of 3D nerve models.

## 4.4 Validation

This section illustrates the validation of centerline and surface extraction methods.

### 4.4.1 Centerline Validation

For both synthetic and patient datasets, a quantitative medial axis validation is performed. For the synthetic dataset, this validation images feature additive Gaussian noise while also replicating partial volume effects. Our quantitative analysis centers on the computation of the average Euclidian distance and maximum distance between each point on the computed 1-Simplex medial axis and the nearest point of the ground truth medial axis curve. The ground truth was generated as described in Section 4.3.1. Table 3 shows the results. In each case, the average and maximum distances of the computed 1-Simplex curve from the ground truth is less than the voxel size which implies sub-voxel accurate medial axis computation.

Table 3. Quantitative validation of the medial axis extraction method for synthetic datasets

Synthetic Volume	Voxel Size (mm)	Presence of Noise	Average Distance (mm)	Maximum Distance (mm)
Arc	0.10	No	0.0958	0.1591
	0.50	Yes	0.3169	0.4760
	1.00	Yes	0.2126	0.4308
Sine tube	0.10	No	0.1156	0.3774
	0.50	Yes	0.3258	0.3912
	1.00	Yes	0.4417	0.8870
Helical Tube	0.50	Yes	0.1358	0.4528
	1.00	Yes	0.4877	0.8615

We also carried out the same quantitative validation on the MRI patient dataset by calculating the average distance and the maximum distance between the computed medial axis and the ground-truth medial axis. The ground truth for each nerve is a piecewise-linear path through a set of landmarks provided by a neurosurgeon at UNC School of medicine, Chapel Hill NC. To visualize this validation concept, distances between the extracted nerve medial axis and the ground truth medial axis are shown in Fig. 26 for the oculomotor nerve (CNIII).

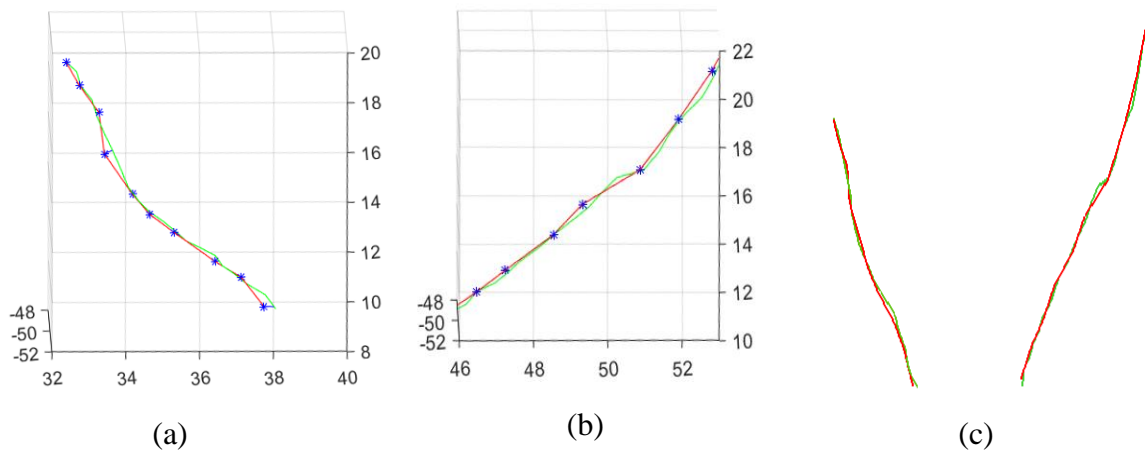


Fig. 26. Visualization of CNIII w.r.t. the ground truth; (a) left side of the nerve, extracted centerline curve and ground truth centerline are shown in green and red respectively, ground truth landmarks are shown in blue asterisk; (b) right side of the nerve; (c) Both nerve centerline models (green curves) where the ground truth centerline are shown as red curves.

The validation results of the MRI dataset are shown in Table 4. In each case, the average and maximum distances are also less than or equal to the voxel size, implying persistent sub-voxel accuracy both for synthetic and patient data.

Table 4. Quantitative validation of the medial axis extraction method for the brainstem MRI dataset

Cranial Nerve	Average distance (mm)	Max distance (mm)
CNIII-left	0.1967	0.3040
CNIII-right	0.2177	0.2500
CNIV-left	0.3017	0.1542
CNIV-right	0.3074	0.2837
CNV-left	0.2150	0.2550
CNV-right	0.2068	0.2600
CNVI-left	0.1805	0.2003
CNVI-right	0.1913	0.2103
CNVII-left	0.1725	0.2215
CNVII-right	0.1924	0.3004
CNVIII-left	0.2000	0.2698
CNVIII-right	0.2198	0.2711
CNIX-left	0.1624	0.2632
CNIX-right	0.1791	0.2913
CNX-left	0.2025	0.2765
CNX-right	0.1584	0.2997
CNXI-left	0.1225	0.2693
CNXI-right	0.1584	0.2409
CNXII-left	0.1618	0.2937
CNXII-right	0.1529	0.2313
<b>Average</b>	<b>0.195</b>	<b>0.256</b>

#### 4.4.2 Validation of Boundary Segmentation

For validating boundary segmentations, we use manual segmentation, performed by an expert, as the ground truth. The manual segmentations are performed by labeling every 2D slice

using 3D Slicer [110], which is a very time-consuming process. Also, manually segmented results are not smooth as the labeling is based on manual contouring. For the thinner nerve, such as CNXI, it was very challenging to produce a manually segmented contiguous nerve surface. We present the quantitative validation for six pairs of nerve – CNIII, CNV, CNVI, CNVIII, CNX and CNXI. CNIII and CNV are comparatively bigger one, therefore is a good candidate for manual segmentation. Even though it was a cumbersome process to manually segment the other four pairs of nerve (CNVI, CNVIII, CNX and CNXI), it was possible because of their anatomical course as well as high image contrast resolution in this specific dataset. Visual comparisons between the segmentation results from our algorithm and ground truths are shown in Fig. 27, Fig. 28, Fig. 29, Fig. 30, Fig. 31 and Fig. 32 for nerves CNIII, CNV, CNVI, CNVIII, CNX and CNXI, respectively.

We compute four performance measures to compare the quality of the segmentation results with respect to the ground truths. The performance metrics are: average distance, Mean Square Distance (MSD), Hausdorff Distance and Dice's coefficient. All the performance metrics are computed in millimeter units. Statistical comparisons are reported in Table 5.

The Dice similarity coefficient compares the similarity between the resulting segmentation and ground truth, thus measures the amount of spatial overlap, which can be defined using (48).

$$DSC(A, B) = \frac{2 \times |A \cap B|}{|A| + |B|}, \quad (48)$$

where A and B are the two surfaces being compared.

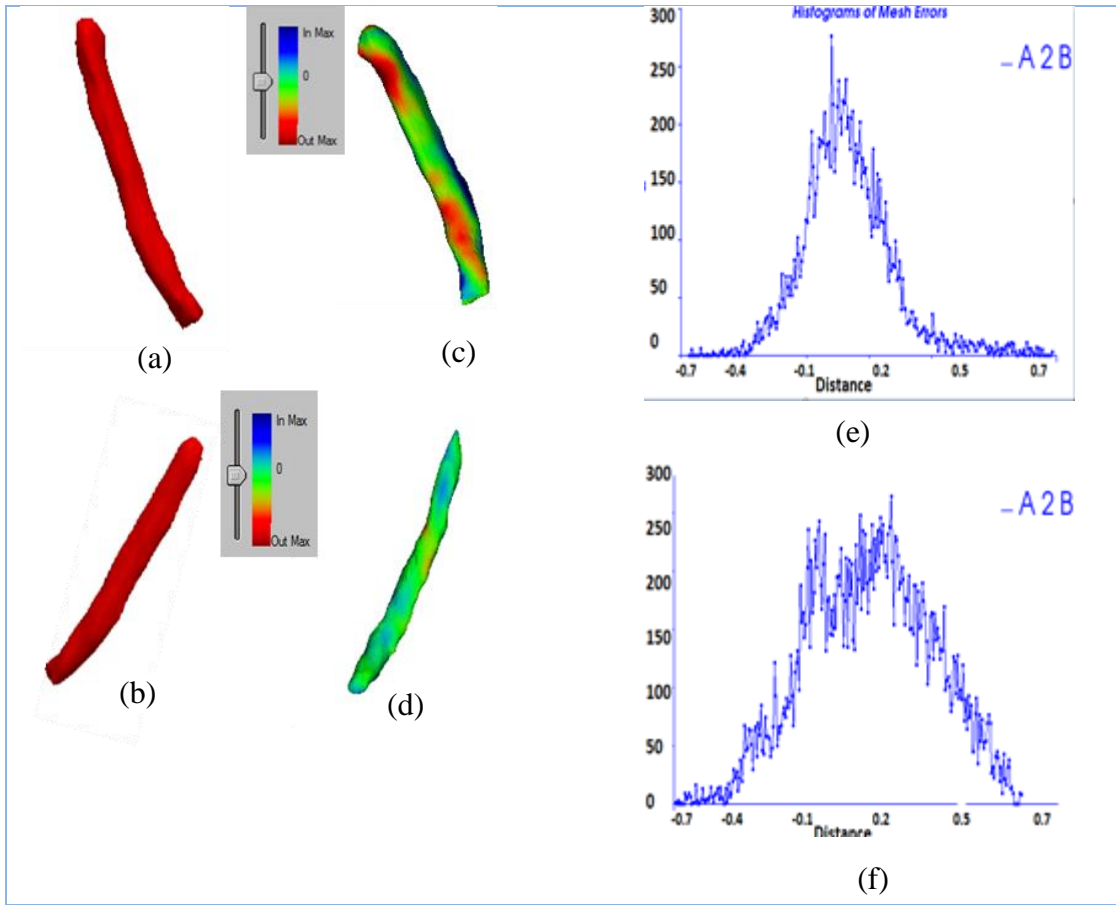


Fig. 27. Validation of oculomotor nerves (CNIII). (a) and (b) show manual segmentation results. (c) and (d) show comparison of the manual and our 2-Simplex segmentation results where the blue region shows over-segmentation error, red region shows under-segmentation error and green region shows zero error. Top color-code: In-Max = -0.6mm, Out-Max = 0.7mm; Bottom color-code: In-Max = -0.6mm, Out-Max = 0.7mm. (e) and (f) depict the distribution of the error compiled over all vertices.

The Hausdorff Distance measures how far the two segmentations are from each other and therefore quantitatively represents a measure of the worst segmentation error, defined as (49).

$$HD(A, B) = \max(h(A, B), h(B, A)) \quad (49)$$

$$h(A, B) = \max_{a \in A} \min_{b \in B} \text{dist}(a, b),$$

where A and B are the two surfaces being compared.

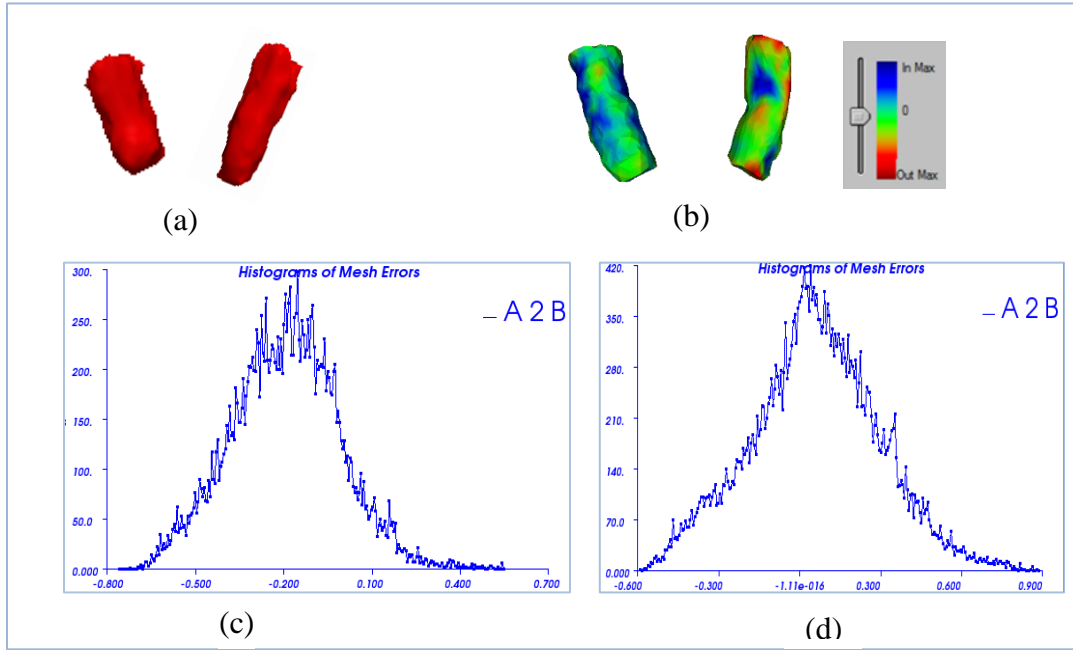


Fig. 28. Validation of abducens nerves (CNV). Panel (a) shows manual segmentation results. Panel (b) shows comparison of the manual and our 2-Simplex segmentation results where the blue region shows over-segmentation error, red region shows under-segmentation error and green region shows zero error. Top color-code: In-Max = -0.3mm, Out-Max = 0.5mm; Bottom color-code: In-Max = -0.3mm, Out-Max = 0.5mm. Panel c) depicts the distribution of the error compiled over all vertices.

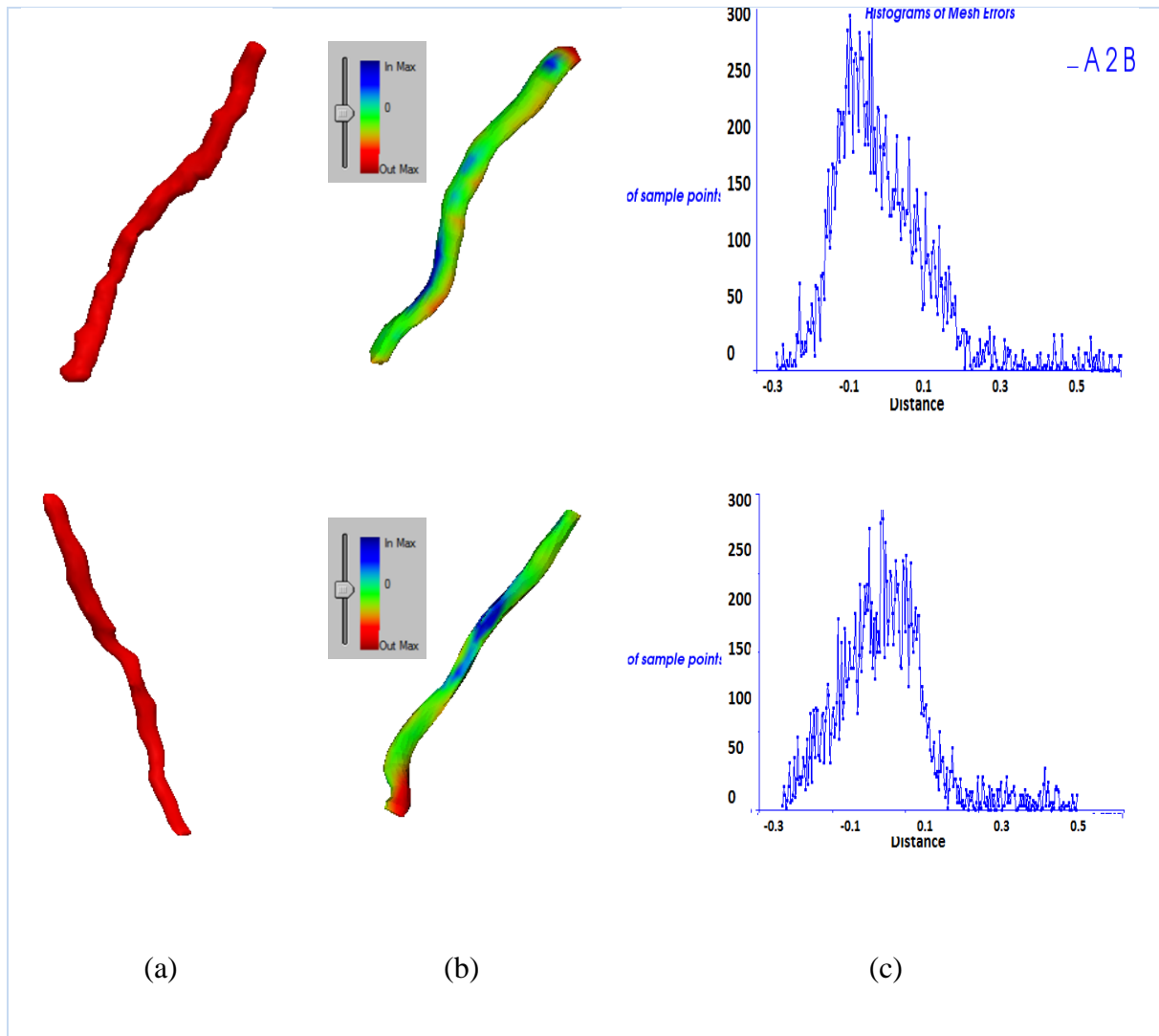


Fig. 29. Validation of trigeminal nerves (CN VI). (a) shows manual segmentation results. (b) shows comparison of the manual and our 2-Simplex surface segmentation results where the blue region shows over-segmentation error, red region shows under-segmentation error and green region shows zero error. Color-code: In-Max = -0.6mm, Out-Max = 0.8mm. (c) depicts the distribution of the error compiled over all vertices for left (top-rightmost graph) and right(bottom-rightmost graph) nerve, respectively.



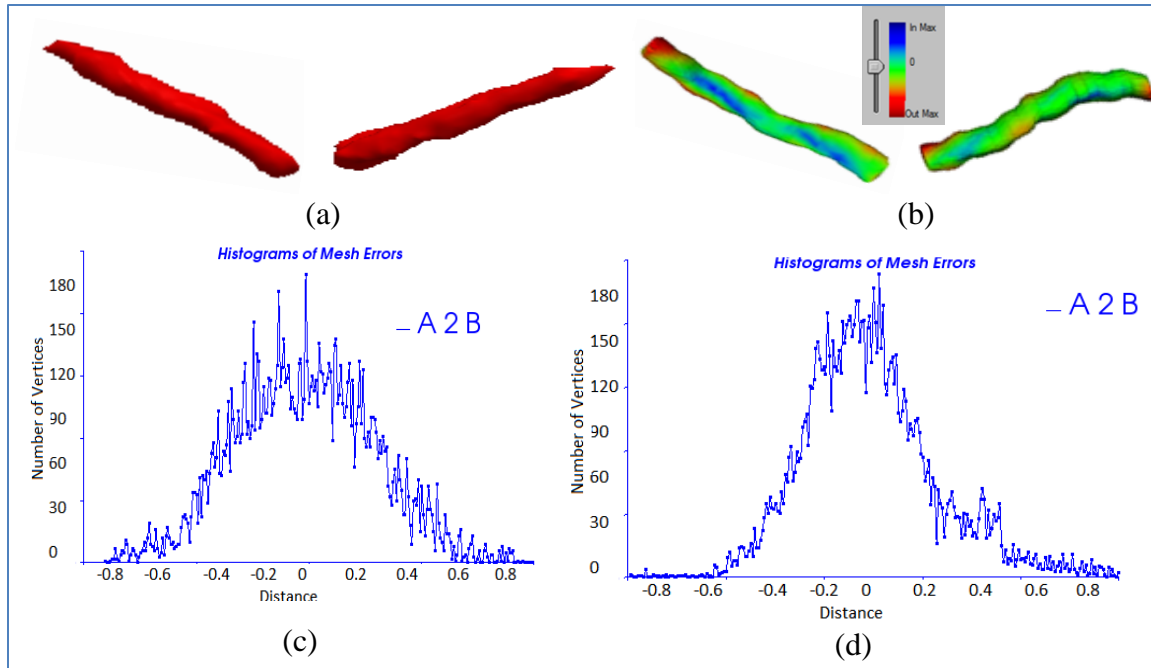


Fig. 30. Validation of vestibulocochlear nerves (CN VIII). (a) shows manual segmentation results. (b) shows comparison of the manual and our 2-Simplex segmentation results where the blue region shows over-segmentation error, red region shows under-segmentation error and green region shows zero error. Color-code: In-Max = -0.6mm, Out-Max = 0.8mm. (c) – (d) depict the distribution of the error compiled over all vertices for left and right nerve, respectively.

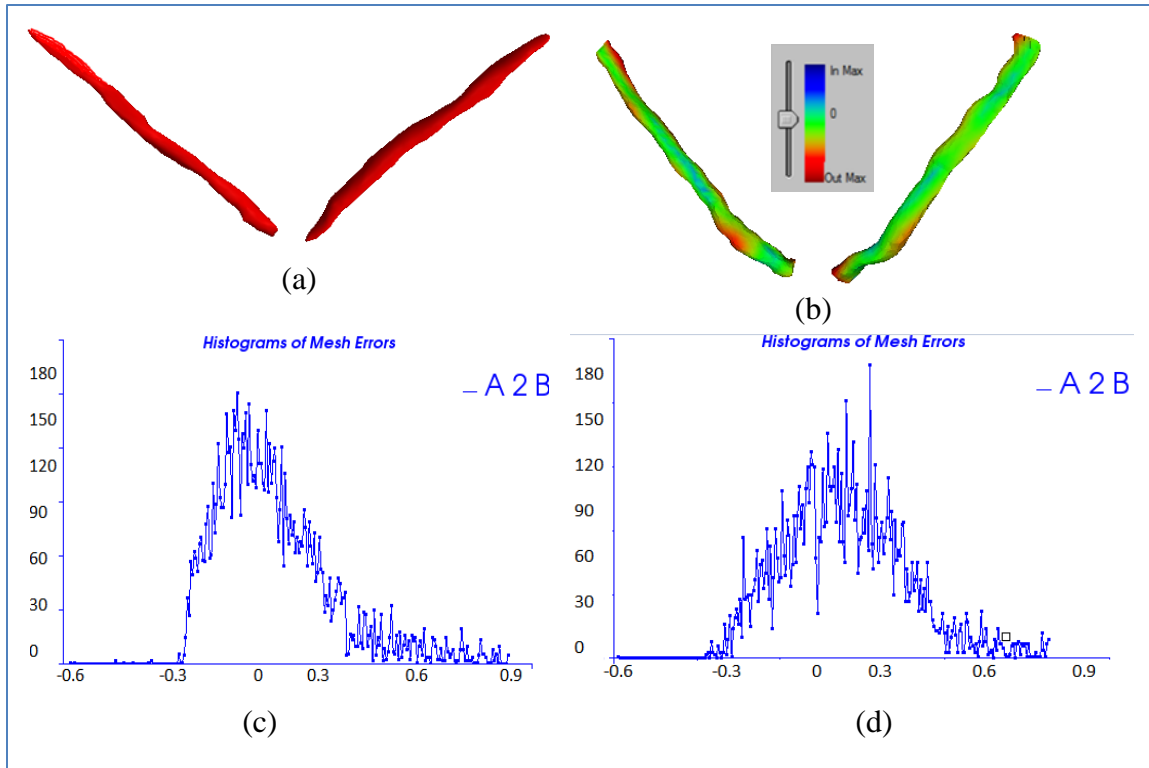


Fig. 31. Validation of vagus nerves (CN X). (a) shows manual segmentation results. (b) shows comparison of the manual and our 2-Simplex segmentation results where the blue region shows over-segmentation error, red region shows under-segmentation error and green region shows zero error. Color-code: In-Max = -0.6mm, Out-Max = 0.8mm; (c) – (d) depict the distribution of the error compiled over all vertices for left and right nerve, respectively.

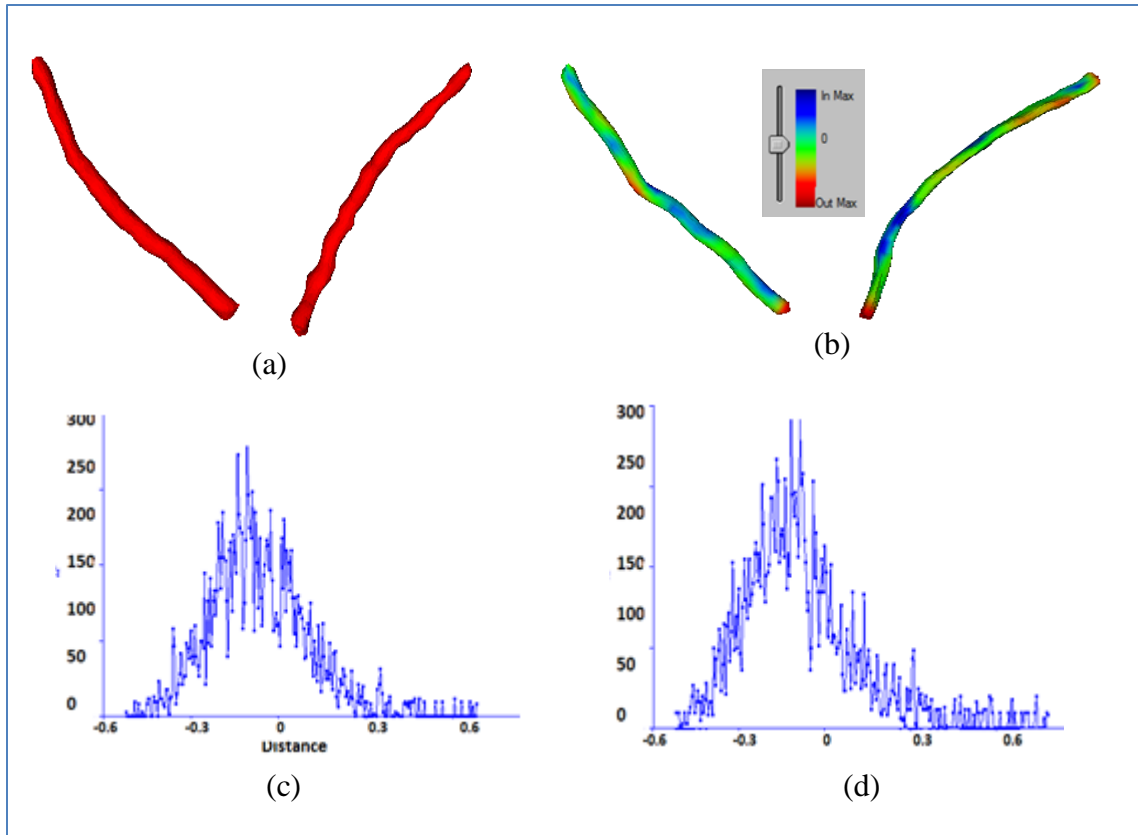


Fig. 32. Validation of accessory nerves (CNXI). (a) shows manual segmentation results. (b) shows comparison of the manual and our 2-Simplex segmentation results where the blue region shows over-segmentation error, red region shows under-segmentation error and green region shows zero error. Color-code: In-Max = -0.6mm, Out-Max = 0.6mm (c) and (d) depict the distribution of the error compiled over all vertices for left and right nerve, respectively.

From Table 5, the worst surface segmentation error in terms of Hausdorff Distance is 76.6% which was seen in right CNX on the other hand the minimum similarity in terms of Dice coefficient is 72.5% for left CNXI. The average of the sample mean error distance over all the nerves is 0.03 mm and the average of mean squared distance is 0.04 mm. The average HD is 0.62 mm and dice similarity coefficient is 82%.

Table 5. Quantitative validation of boundary surfaces of cranial nerves

Nerves	Validation Matric			
	Sample Mean Error (mm)	Mean Square Distance (MSD) (mm)	Hausdorff Distance (mm)	Dice's coefficient
CNIII-left	0.002	0.027	0.700	0.858
CNIII-Right	0.019	0.021	0.600	0.803
CNV-left	0.190	0.070	0.757	0.816
CNV-right	0.013	0.054	0.759	0.895
CNVI-left	0.002	0.027	0.350	0.854
CNVI-right	0.018	0.021	0.400	0.803
CNVIII-left	0.016	0.094	0.683	0.846
CNVIII-right	0.002	0.082	0.632	0.946
CNX-left	0.054	0.035	0.686	0.727
CNX-right	0.005	0.039	0.766	0.832
CNXI-left	0.061	0.035	0.686	0.725
CNXI-right	0.019	0.066	0.538	0.746
<b>Average</b>	<b>0.033</b>	<b>0.047</b>	<b>0.629</b>	<b>0.820</b>

## 4.5 Conclusion

In this chapter, we present a discrete deformable model-based approach to segmenting the ten pairs of brainstem cranial nerves from CNIII (the oculomotor nerve) to CNXII (the Hypoglossal nerve) using MRI data. Here our first contribution is a nerve medial axis extraction technique using a novel 1-simplex based discrete deformable model from MR data where the initial nerve is generated between a pair of user-supplied end points by minimal path technique

and vesselness information is encoded as external forces. Our second contribution is to employ the 2-simplex deformable surface model to identify the nerve boundary from an initialization comprised of the centerline and radius function of the first stage. Quantitative validation for medial axis extraction technique shows sub-voxel accuracy both for synthetic and patient MR data. The surface segmentation technique shows encouraging result of 82% Dice Coefficient between manual and semi-automatic results.

## CHAPTER 5

### SHAPE-AWARE DEFORMABLE CONTOUR ATLAS

In this chapter, we will discuss the construction of a Statistical Shape Model-based atlas of cranial nerve centerlines. A set of training data for the construction of the 3D contour shape model is produced using a 1-Simplex-based discrete deformable 3D contour model. Point correspondence for the training dataset is performed using an entropy-based energy minimization framework applied to particles located on the centerline curve. The constructed average shape and Principal Component Analysis (PCA) model computed from the training dataset are incorporated into the 1-Simplex mesh as *a priori* knowledge, making the deformation stable against low resolution and image artifacts during segmentation using MRI data.

The chapter is organized as follows: Section 5.1 describes different steps of the Statistical Shape Model including methods of constructing training shapes, point distribution model and establishing shape correspondence. Computation of the shape prior is described in Section 5.2. The segmentation process of cranial nerves using shape-based deformable model is detailed in Section 5.4. Section 5.5 illustrates the benchmark of evaluating an SSM. Section 5.6 and 5.7 provide detailed experimental results and validation of the proposed method using synthetic and patient MRI data. Section 5.8 concludes the chapter.

#### 5.1 Statistical Shape Models

The steps of constructing an SSM are described in this section.

##### 5.1.1 Construction of Training Shapes

The goal of Statistical Shape Models (SSMs) is to construct, from a set of training shapes, a model that represents the patterns of expected shape and shape variability, and then

using the SSM to segment the anatomy of interest within the target image in a manner consistent with its underlying statistics. An SSM computes the mean shape and the modes of variation from a pool of training data, the latter of which characterize second-order shape statistics. Therefore, the first step towards the SSM is to construct a training dataset of  $M$  shapes from which shape statistics are inferred.

In this research, we have created SSMs for the ten pairs of cranial nerves with attachments to the brainstem (CNIII to CNXII), to exploit statistical shape priors to stabilize our 3D deformable contour approach to cranial nerve segmentation. To generate training shapes for each of the nerves, we have segmented the T<sub>2</sub>-weighted MRI datasets of 10 different patients. Each of the shapes in a training dataset is a nerve centerline, segmented using the 1-Simplex method discussed in 0 and manually corrected where necessary. While the semi-automatic 1-Simplex deformable model approach is used for segmenting nerve centerlines, it is feasible to manually correct these segmented results so that no segmentation error can propagate from the training dataset to the shape-based nerve atlas. As a result, this SSM-aware deformable 3D contour model preserves the accuracy of the segmentation while eliminating the need for cumbersome manual identification of nerve centerline points.

### 5.1.2 Shape-based Features

When designing an SSM, one of the fundamental decisions is to choose an appropriate shape representation. A brief discussion on shape representation is given in Section 3.5.

The discrete nature of the 1-Simplex deformable model that we have used to achieve the segmentation provides a generic way to represent a shape: using a set of points distributed over the contour shape. These point features are also known as landmarks in the SSM literature. We

have chosen the widely used Point Distribution Model (PDM) introduced by Cootes et al.[102] for the construction of the SSM. In general, a PDM is a statistical model that represents the mean shape and modes of variation calculated from training set of contours or surfaces where each component of the set is represented as a discrete number of points or landmarks. All the points of a contour or surface are concatenated into one vector. The construction of a PDM proceeds in three steps: i) shape correspondence, ii) shape alignment and iii) computation of the principal modes of variation.

In the following section, the method of shape correspondence that we have used for the PDM construction is discussed. The shape alignment is performed using GPA as discussed in Section 0. The shape variation is modeled as a multivariate Gaussian distribution where the principal modes of variation are computed using PCA as detailed in Section 3.5.3.

## 5.2 Shape Correspondence and Model Construction

Shape correspondence is established by finding a set of points from one shape that can be mapped to the same set of points found on another shape. Correct and anatomically meaningful shape correspondence is important to ensure precise shape parametrization and representation; otherwise the error introduced by the correspondence technique might be propagated to the resulting SSM. There are several point correspondence methods to be found in the literature, as reported in this survey paper [128], and the choice for the best approach depends on the application context and user preference. Point correspondence is classified into two groups based on the density of the correspondence: *dense correspondence*, which is achieved for all the landmark points or a subset of the available pointset, and *sparse correspondence*, which is done for a small set of anatomically significant feature points that are pre-selected. Although sparse



correspondence can be established by manual localization in 2D datasets, this overhead is much more prohibitive for 3D data. Establishing a meaningful dense point correspondence between all of the shapes of the training dataset is almost impossible by manual approach because of the following reasons:

1. Manual landmarking does not scale easily to the large number of landmarks needed for 3D structures.
2. Manual landmarking suffers from poor repeatability, particularly in situations where definitive tissue boundaries are more difficult to locate.
3. Manual landmarking is a tedious, time-consuming approach, which requires expert knowledge.
4. In case of cranial nerves, the difficulties of manual landmarking arise because of the presence of partial volume effects and unclear image gradient in MRI data as well as ambiguities due to the proximity of multiple nerves to each other.

One approach of achieving dense point correspondence in SSM is reported in [129], which used an implicit spherical surface parameterization. The surface parameterization was achieved by mapping the surface of the original object to the surface of a unit sphere where the parameterization is formulated as an optimization problem. Based on this technique a surface modeling method using Spherical Harmonics (SPHARM) was introduced in [130], which implicitly defined dense surface correspondences. Davies et al. [131] proposed an automatic point correspondence method involving the Minimum Description Length (MDL) of information theory, which sought a set of shape parameterizations to describe the training dataset. The main limitation of such a parametric approach for shape analysis in medical imaging is that the segmented volumes are difficult to generate parametrically.

In this research, we have chosen a *non-parametric* approach to establish point-based dense correspondence which has the advantage of performing *homologous point distribution automatically* over the contour shapes. The method is comprised of two main steps:

1. Sampling points over Simplex curves.
2. Establishing correspondence by optimizing entropy of the training dataset.

### 5.2.1 Point Sampling

We have employed a particle system-based method for controlled point sampling using cotangent theory [132] which was first applied to surfaces and subsequently extended to contours.

A training surface or contour can be represented implicitly using  $n$  repulsive particles  $p(t)$ , which is constrained by equation (50) [133]. An implicit surface can be represented using equation (50):

$$F(\mathbf{p}(t), \mathbf{q}(t)) = 0, \quad (50)$$

where  $\mathbf{q}(t)$  is the set of parameters that can handle surface deformations. Particles are distributed homogeneously over the surface using a repulsion force whereby each particle achieves a repulsion velocity. This method is known as the Witkin-Heckbert (W-H) method. Each particle has a repulsion radius that grows and shrinks based on the particle's local energy. However, this method cannot accommodate complex shapes with large variations in shape curvature. This problem is addressed in [132], where the particle placement is dependent on an optimization of the potential energy, as described in equation (51):

$$E_i = \frac{1}{2} \sum_{j=1}^{m, j \neq i} E_{ij}(|\mathbf{r}_{ij}|), \quad (51)$$

where  $\mathbf{r}_{ij} = \mathbf{p}_i - \mathbf{p}_j$ , which is the distance between interacting particles  $\mathbf{p}_i$  and all  $\mathbf{p}_j$  that lie within the neighborhood of the potential field of  $\mathbf{p}_i$ .

An even and homogeneous point sampling depends on the pair-wise energy functional  $E_{ij}$  which is defined in equation (52).

$$E_{ij} = \begin{cases} \cot\left(\frac{|\mathbf{r}_{ij}| \pi}{\sigma}\right) + \frac{|\mathbf{r}_{ij}| \pi}{\sigma} - \frac{\pi}{2} & |\mathbf{r}_{ij}| \leq \sigma \\ 0 & |\mathbf{r}_{ij}| > \sigma \end{cases}. \quad (52)$$

The cotangent-based energy function  $E_{ij}$  is dependent on only one parameter  $\sigma$ , where  $\sigma$  is the radius of potential field of particles. The optimization of this pairwise potential energy function ensures that homologous point pairs arise from the similar points on the contours, i.e. that the sampling of the two surfaces or contours be done as consistently as possible, so that the pairwise correspondences themselves are automatic.

The optimal distribution of particles on a sphere using repulsive forces is shown in Fig. 33, where the system is initialized using a single particle and then produces new, nearby particles iteratively, until a specific number of particles are produced to reach the steady state.

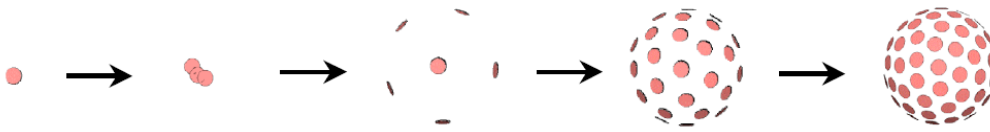


Fig. 33. Point Distribution on a sphere using particle positing. Reproduced from [134].

### 5.2.2 Covariance-based Correspondence Entropy

We establish the shape-to-shape correspondence using the entropy-based method described in [134] based on dynamic particles. This method proves its superiority by establishing correspondence through automatic consistent landmark positioning.

The ensemble  $\varepsilon$  is composed of  $M$  1-Simplex curves where each of the curves have an equal number of points after point sampling using the method described in Section 5.2.1. Each of the points in the Simplex curves is considered as an individual particle. The ensemble  $\varepsilon$  can be written as  $\varepsilon = z^1, z^2, \dots, z^M$ , where each  $z^k$  is modeled as an instance of a random variate  $\mathbf{Z}$ . Then the cost function  $Q$  can be formulated as in equation (53).

$$Q = H(\mathbf{Z}) - \sum_k H(\mathbf{P}^k), \quad (53)$$

where  $\mathbf{P}$  is the matrix that holds particle positions. The first term of equation (53) is the entropy of the entire ensemble, and the second term is the combined shape-wise entropy. The entropy is defined by modeling the probability  $p(\mathbf{Z})$  parametrically using a Gaussian distribution, as in (54).

$$H(\mathbf{Z}) = \frac{1}{2} \log |\mathbf{\Sigma}| = \frac{1}{2} \sum_{j=1}^{Nd} \log \lambda_j, \quad (54)$$

where  $\mathbf{\Sigma}$  represents the covariance of the ensemble and  $\lambda_j$  are the eigenvalues of the  $\mathbf{\Sigma}$ .

The point correspondence method described in this dissertation was first developed for surfaces by the scientific computing group of university of Utah, through a open-source software toolkit, ShapeWorks. The method has been recently extended to 3D contours through a second software tool called ContourWorks, which has been used to perform point correspondence for the proposed method in this dissertation. Our work is the first application of ContourWorks, and the Utah group appears as co-authors of our recent conference paper [135].

### 5.3 Computation of Strong Shape Priors

Segmentation using prior knowledge can be broadly categorized into two classes based on the level of information involved in the segmentation process: weak priors and strong priors. Weak priors build on scant knowledge of the segmentation domain, which is inferred from the image to be segmented or from very general assumptions about anatomy, such as the contiguity

of tissues. On the other hand, strong priors involve knowledge extracted from the PDM of the shape that needs to be segmented. The approach for computing strong shape priors for deformable models of the nerve is described in this section.

Consider  $M$  segmented nerve centerlines which are in correspondence. Each centerline model consists of  $N$  points. An approach incorporating only first-order statistics such as the mean of the segmented shapes does not consider variations among shapes. Thus, such an approach might produce poor segmentation results when segmenting test data having large variations. For better segmentation results, second-order statistics can be incorporated simply by finding a goodness of fit of the feature  $\mathbf{x}$  to the PCA model. This can be achieved by calculating Mahalanobis Distance as described below:

Given the mean  $\mu$  and covariance matrix  $\Sigma$  estimated from the training dataset  $M$ , the Mahalanobis Distance  $D_M$  of an observation  $\mathbf{x} = (\mathbf{x}_1, \mathbf{x}_2, \dots, \mathbf{x}_N)$  measures how many standard deviations  $\mathbf{x}$  is away from the mean  $\mu$  along each principle component axis of  $\Sigma$ . The Mahalanobis Distance  $D_M$  is defined using equation (55).

$$D_M(\mathbf{x}) = (\mathbf{x} - \mu)^T \Sigma_X^{-1} (\mathbf{x} - \mu). \quad (55)$$

The Mahalanobis distance has been exploited for building Active Appearance Models (AAM) in [32, 96, 102, 136], where image intensity and gradient boundary profiles are used as local appearance features. Inspired by Cootes et al. [137], we computed the Mahalanobis Distance to integrate second-order statistics with the shape model. The problem in computing  $D_M$  using equation (55) is that it requires the inversion of the covariance matrix, which might cause the singular matrix problem in a situation when the covariance matrix is not symmetric positive-definitive. To rectify this issue we choose to use the alternative approach suggested in [137] to compute  $D_M$  as a function of eigenvalues and eigenvectors.

Let the PCA model be computed from  $\mathbf{\Sigma}$  of aligned training shapes  $M$  where  $\phi_i$  are the eigenvectors of  $\mathbf{\Sigma}$  and their corresponding eigenvalues  $\lambda_i$  are sorted in an order such that  $\lambda_i > \lambda_{i+1}$ . Any test shape  $\mathbf{x}$  can be approximated using expression of (56):

$$\tilde{\mathbf{x}} = \boldsymbol{\mu} + \mathbf{b}_i \phi_i, \quad (56)$$

where  $\mathbf{b} = (\mathbf{b}_1, \mathbf{b}_2, \dots, \mathbf{b}_m)$  is the model parameter vector, each factor  $\mathbf{b}_i$  corresponding to each eigenvector  $\phi_i$ . The Mahalanobis distance can then be formulated as:

$$D_M = \sum_{i=1}^m \left( \frac{b_i^2}{\lambda_i} \right). \quad (57)$$

The  $k$  most significant modes of variation are described by the first  $k$  eigenvalues, thus reducing the dimensionality of the problem. In such a case,  $D_M$  can be computed using equations (58) and (59):

$$D_M = \sum_{i=1}^k \left( \frac{b_i^2}{\lambda_i} \right) + \frac{2R^2}{\lambda_k} \quad (58)$$

$$R^2 = (\mathbf{x} - \tilde{\mathbf{x}}) (\mathbf{x} - \tilde{\mathbf{x}})^T, \quad (59)$$

where  $R^2$  is the squared residual error between the shape  $\mathbf{x}$  and its approximation  $\tilde{\mathbf{x}}$ .

$D_M$  can be described as a quantitative value of how well the PDM fits the test shape, and it approaches zero as the fitting of the PCA to the test data improves.

## 5.4 Segmentation using SSM

The flow chart of the segmentation process using SSM-based deformable model is shown in Fig. 34, where the first part shows the steps for building the SSM and the second part describes the segmentation process using the SSM.

The segmentation of a test image using the SSM-based nerve centerline atlas proceeds in two steps:

1. Average shape registration and best-fitted model computation, and
2. Computation of SSM-based force.

#### 5.4.1 Average Shape Registration and Best-Fitted Model Computation

The reference model needs to be initialized within the image to be segmented in order to start the evolution process of the 1-Simplex mesh. The simplest way to register a model to an image is to i) locate a set of source landmarks on the model and a set of target landmarks on the image, and ii) perform the landmark-based transformation.

The landmarks should be chosen so that they appear as anatomically meaningful features. For each cranial nerve, we can pinpoint only two landmarks: the source point of the nerve where it originates from brainstem (Fig. 5) and the end point at the cranial foramen where the nerve exits (Fig. 6). As a result, a purely landmark-based registration is not applicable in this case to achieve model to image registration due to an insufficient number of identifiable landmarks. We provide the two end points manually in the current approach, one each for the brainstem attachments and foramina. Instead of directly registering the reference model to the image, we compute the transformation using the Minimal Path, as described below.

A point-set to point-set registration technique is implemented between the reference average shape  $\mu$  and the Minimal Path (MP) computed from user-identified start and end points in test MRI data. The MP computation method is the same as described in Section 4.1.2. There are two assumptions considered for this registration technique:

- (1) the point correspondences are already established between the sets of points and
- (2) the two sets of points are relatively close to each other, based on an approximate putative transformation.

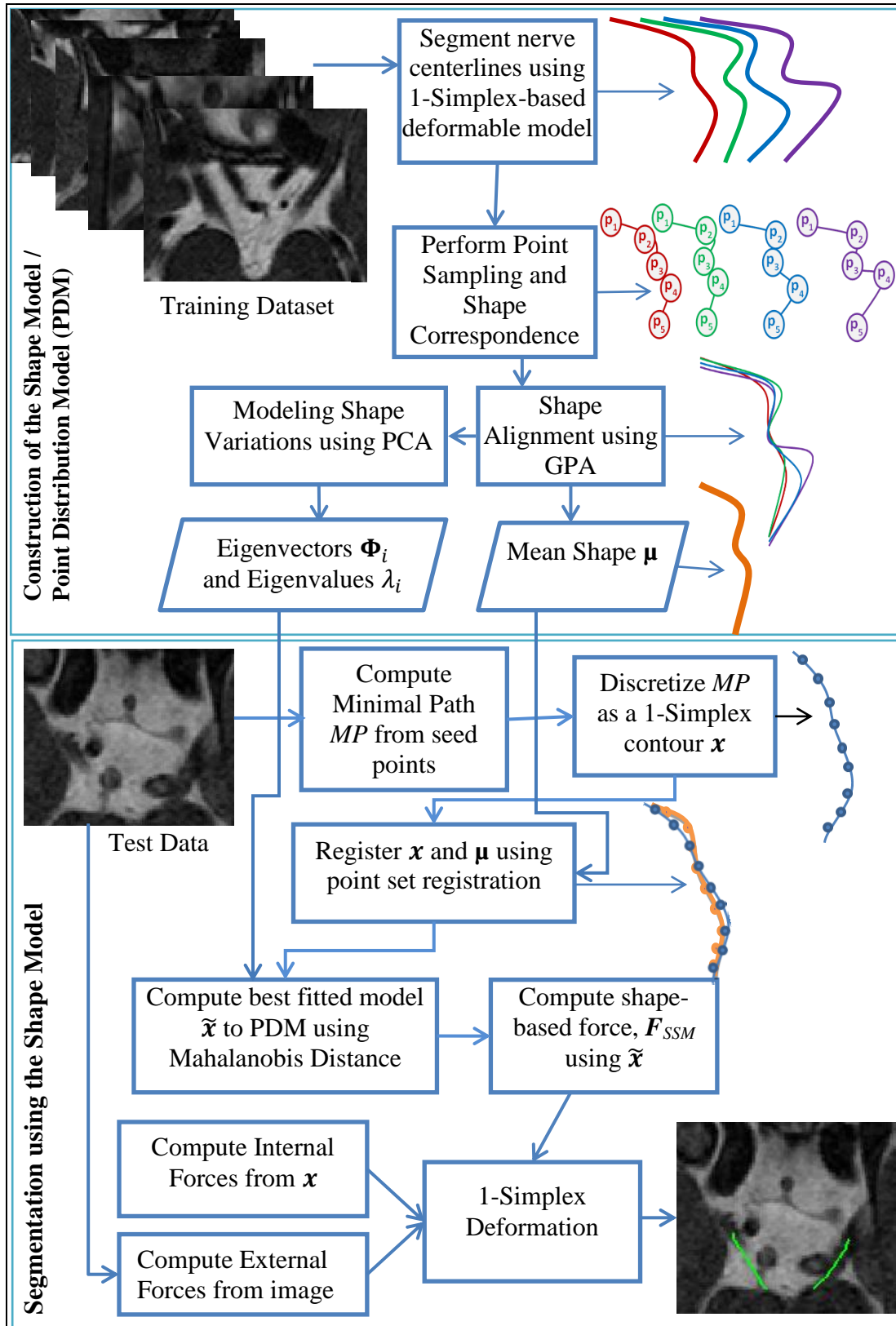


Fig. 34. Flow chart of SSM construction and SSM-based Segmentation.



The computed MP is then converted into a discrete 1-Simplex model. The mapping between the MP and the reference shape is performed using 3D similarity transform by applying a rotation, translation and isotropic scaling. The registration is achieved by iteratively minimizing Euclidian distances between mutually closest points using a Levenberg-Marquardt (LM) based optimizer. LM is a nonlinear least squares minimizer used for fitting a set of observation with a model by combining the advantages of gradient descent and Gauss-Newton methods [138].

#### 5.4.2 Computation of SSM-based Force

In this work, any Simplex-based force has the form of a spring force as expressed in (60):

$$\mathbf{f}_i = \alpha(\mathbf{P}_i - \widetilde{\mathbf{P}}_i), \quad (60)$$

where  $\alpha$  is the stiffness parameter that controls the force weight. In order to approximate the solution of the system equation of (5) using implicit Euler method, these forces need to be defined with respect to the position of the points of a Simplex mesh.

The integration of the SSM into the 1-Simplex model is performed by introducing a SSM-based internal force  $\mathbf{F}_{SSM}$  which is integrated into the equilibrium expression of (5). The idea of computing  $\mathbf{F}_{SSM}$  is inspired by the ‘shape memory force’ used in [68, 139]. The purpose of this force is to move the point toward a predefined reference shape using the 1-Simplex parameters ( $\varepsilon, \varphi$  and  $\phi$ ). The reference Simplex mesh is computed using the mean shape of the SSM. The force is defined as:

$$\mathbf{F}_{SSM} = \tilde{\varepsilon}_{1i}\mathbf{P}_{N_1(i)} + \tilde{\varepsilon}_{2i}\mathbf{P}_{N_2(i)} + h(\tilde{\phi}_i)n(\tilde{\psi}_i) - \mathbf{P}_i. \quad (61)$$

Here  $\mathbf{P}_i$  is the  $i^{\text{th}}$  point of the 1-Simplex model that is being deformed;  $\mathbf{P}_{N_1(i)}$  and  $\mathbf{P}_{N_2(i)}$  are the two neighbors of  $\mathbf{P}_i$ . The shape parameters ( $\tilde{\varepsilon}_{ji}, \tilde{\psi}_i$  and  $\tilde{\phi}_i$ ) are computed from the reference

shape  $\tilde{\mathbf{x}}$ . Essentially, the SSM-based force deforms the current shape  $\mathbf{x}$  towards its closest match  $\tilde{\mathbf{x}}$  which is determined from the Point Distribution Model (PDM).

## 5.5 Evaluation of SSM

There is no general agreement for choosing an appropriate correspondence method for shapes, specifically for biological shapes. Even though there are several measures to assess the quality of correspondence such as in [140], [141] and [142], we have chosen three evaluation criteria, *compactness*, *generality* and *specificity*, which are considered as benchmarks for comparing correspondence quality, as described in [143]. These three measures are defined in terms of the number of principal modes  $m$  of the PDM constructed from the training dataset.

**Compactness** is the ability to capture the amount of shape variance within the training dataset using as few parameters as possible. It is calculated using equation (62):

$$C(m) = \sum_{i=1}^m \lambda_i, \quad (62)$$

where  $\lambda_i$  is the  $i^{th}$  eigenvalue representing the shape variance using mode  $i$  and  $C(m)$  is the cumulative variance of  $m^{th}$  mode.

**Generality** is the capability of the SSM to represent an unseen new shape outside the training dataset. It can be quantified using the “leave-one-out” cross-validation method. The method builds the statistical model using all the shapes in the training dataset excluding one shape, which is then approximated using the model parameters. The approximation error is calculated using a squared Euclidian distance, which is averaged over all the shapes of the training dataset. Generality is computed as follows:

$$G(m) = \frac{1}{N} \sum_{i=1}^N \epsilon_i^2(m), \quad (63)$$

where  $\epsilon_i^2(m)$  is the sum of squared approximation error defined as:

$$\epsilon_i^2(m) = |x_i - x'_i(m)|^2. \quad (64)$$

In (64),  $x_i$  is the left-out shape and  $x'_i(m)$  is the approximation of  $x_i$  computed from the PDM using  $m$  modes.

**Specificity** is the ability of generating valid shapes that are similar to the shapes of training dataset. This measure is accessed by generating a population of shapes using the PCA and comparing them with the shapes of the training dataset. It is computed quantitatively using the expression of (65). This measure is computed using  $m$  modes:

$$S(m) = \frac{1}{N} \sum_{i=1}^N |x_i(m) - x'_i(m)|^2, \quad (65)$$

where  $x_i(m)$  is a randomly generated shape using the PDM which has the form of (66) and  $x'_i(m)$  are the nearest member of the training set to  $x_i(m)$  which is computed as (66):

$$x'_i(m) = \bar{x} + \sum_{i=1}^N b_i \Phi_i, \quad (66)$$

where  $b_i$  are independently sampled parameter from a 1D Gaussian distribution  $\mathcal{N}(\mathbf{0}, \lambda_i)$  of the PDM and  $\Phi_i$  are the eigenvectors.

## 5.6 Validation using Synthetic Data

To verify the efficiency and robustness of the SSM-based segmentation algorithm, we conducted an experiment using a family of 52 synthetic parametric curves having a helical shape. The family of shapes constitutes the synthetic training dataset where the shapes vary primarily in height, in the number of spirals in the helix and in the radius of the spiral. Shape heights range from 20 mm to 50 mm, the radii of cycles range from 5 mm to 20 mm and the number of helix cycles for each of the shape is kept to either 2 or 3.

### 5.6.1 SSM Construction

Shape alignment of the helical SSM is performed using the GPA method as described in Section 0. The resulting aligned shapes are shown in Fig. 35(a). The point sampling and correspondence method described in Sections 5.2.1 and 5.2.2 is applied to the synthetic training dataset. For each shape, 50 points are sampled as control points. The point correspondence is depicted in Fig. 35(b) where each of the control point of a shape is shown with a specific color ball.

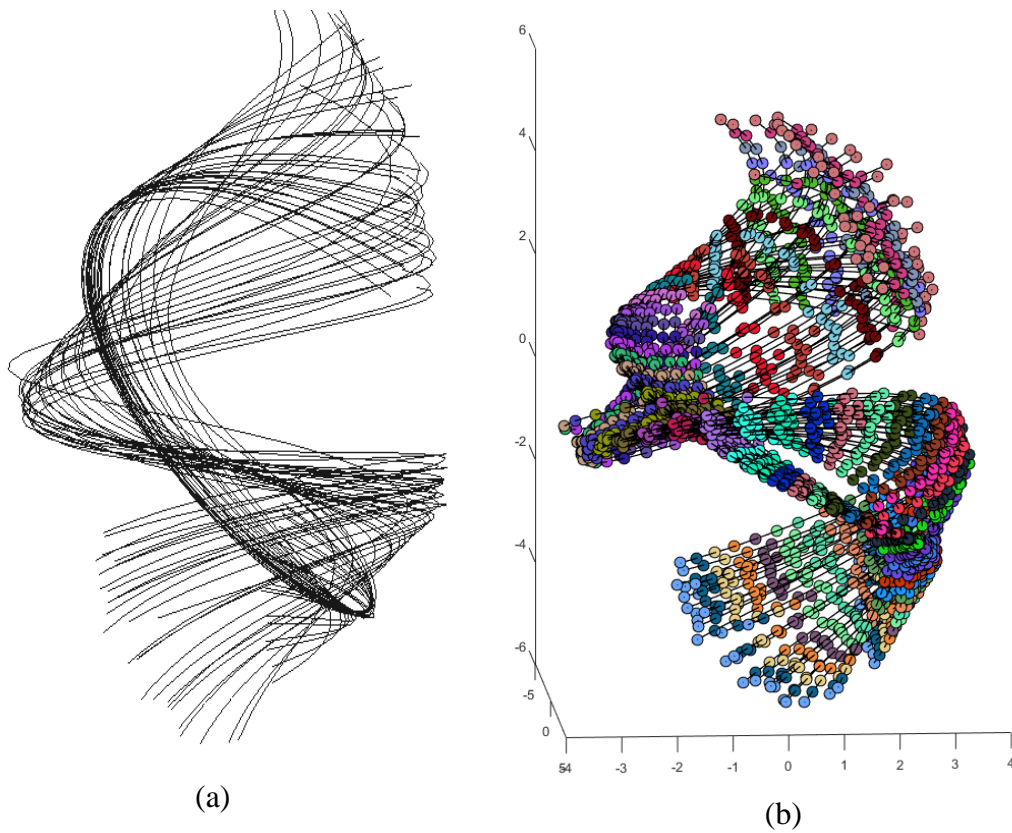
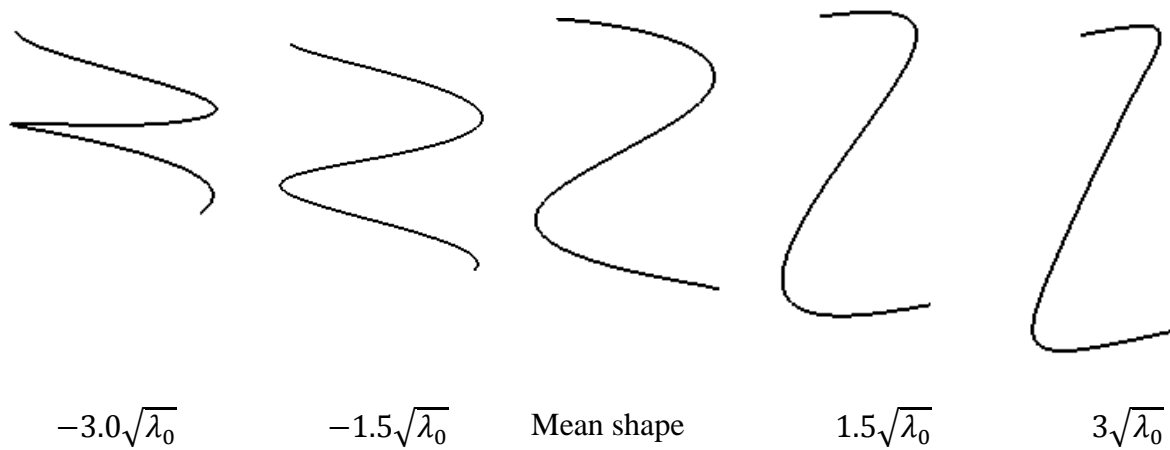


Fig. 35. (a) Shape Alignment and (b) Shape Correspondence of the Helix model.

Thus, all the points of a specific color are in correspondence. The SSM is built by retaining 99% of the total variance where only four modes of variation are used to capture the

variance. The first four principal modes of variation within  $\pm 3$  standard deviation are shown in Fig. 36 where each row corresponds to a mode of variation. The first mode mainly captures the effect of the number of cycles and the scaling of radius in the training dataset. The second mode illustrates the variability in shape length. The third and fourth modes compensate minor differences in the curvature of spiral radii. The constructed SSM can capture 69.14% of variations within the first mode, 96.08% within the second mode, 98.18% within the third mode and 99% within fourth mode.

The correspondence quality is assessed in terms of compactness, specificity and generality as reported in Fig. 37. The specificity curve is generated involving one hundred samples which are created by varying the value of  $b$  parameters using first 25 modes; however, it stables only after first 4 modes. The generality curve is produced using the first 30 modes. However, the curve converges after first few modes. The distance error in the vertical axis of specificity and generality is computed as the Root Mean Squared (RMS) error with the unit in millimeters



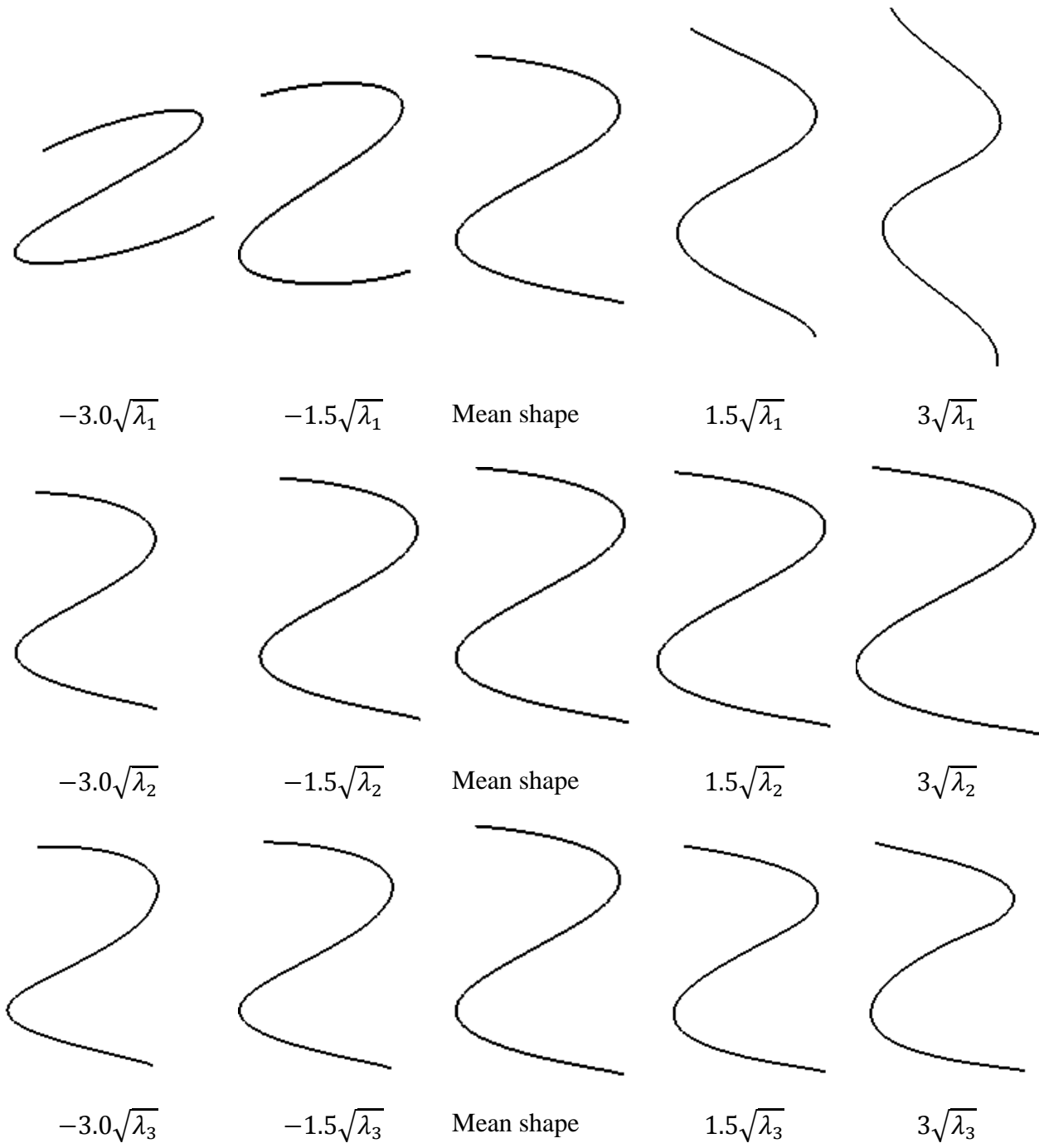
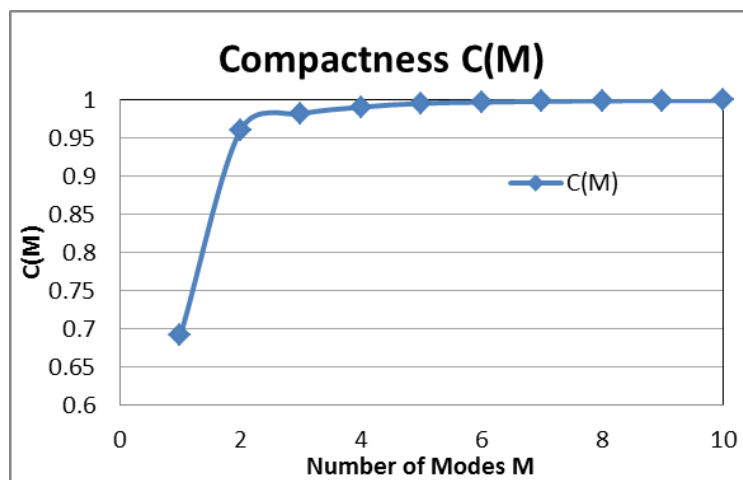
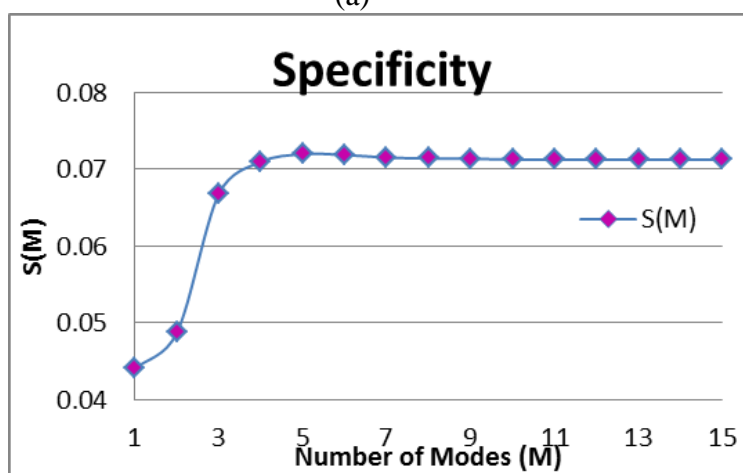


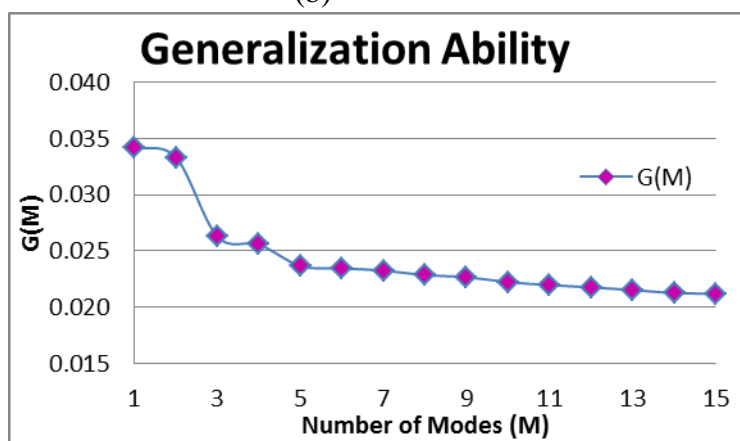
Fig. 36. First four modes of variation of the helix SSM.



(a)



(b)



(c)

Fig. 37. (a) Compactness (b) Specificity and (c) Generality of the helix SSM.

### 5.6.2 Segmentation using the Helix SSM

The performance of image segmentation using the constructed helix SSM is evaluated using a couple of synthetic test volumes: 1) an artificially corrupted volume and 2) a volume with additive Gaussian noise. Both volumes have a spacing of  $0.3 \times 0.3 \times 0.3 \text{ mm}^3$  and dimension of  $115 \times 113 \times 113 \text{ mm}^3$ , containing a helix image whose length is 20 mm, tube radius is 0.5 mm, cycle radius of 10 mm and number of cycles being 2. The intensities of the helix image range between  $[0, 255]$ . The corrupted volume is created by eroding the helix image intensities in some of the slices while keeping the rest of the slices unchanged, as shown in Fig. 38(a). The noisy volume is generated using additive Gaussian white noise with the mean  $\mu = 0$  and the standard deviation  $\sigma = 30$  as shown in Fig. 38 (b). The segmentation results of the noisy image with and without SSM are shown Fig. 39 (a). The centerline extraction of the corrupted volume is depicted in Fig. 39 (b) and (c).

The quantitative validation of these volumes is reported in Table 6. In the case of the volume with noise, the incorporation of SSM into the deformable segmentation shows a slight improvement in terms of MASD:  $0.192 \pm 0.131 \text{ mm}$  without SSM vs.  $0.177 \pm 0.091 \text{ mm}$  with SSM, as well as the HD error decreasing by 6%. For the corrupted volume, the segmentation using SSM outperforms the segmentation without SSM by decreasing the MASD error by 60% and the HD error dropping from 0.506 mm to 0.251 mm. The improvement of SSM-based identification in terms of HD is shown graphically in . 40.



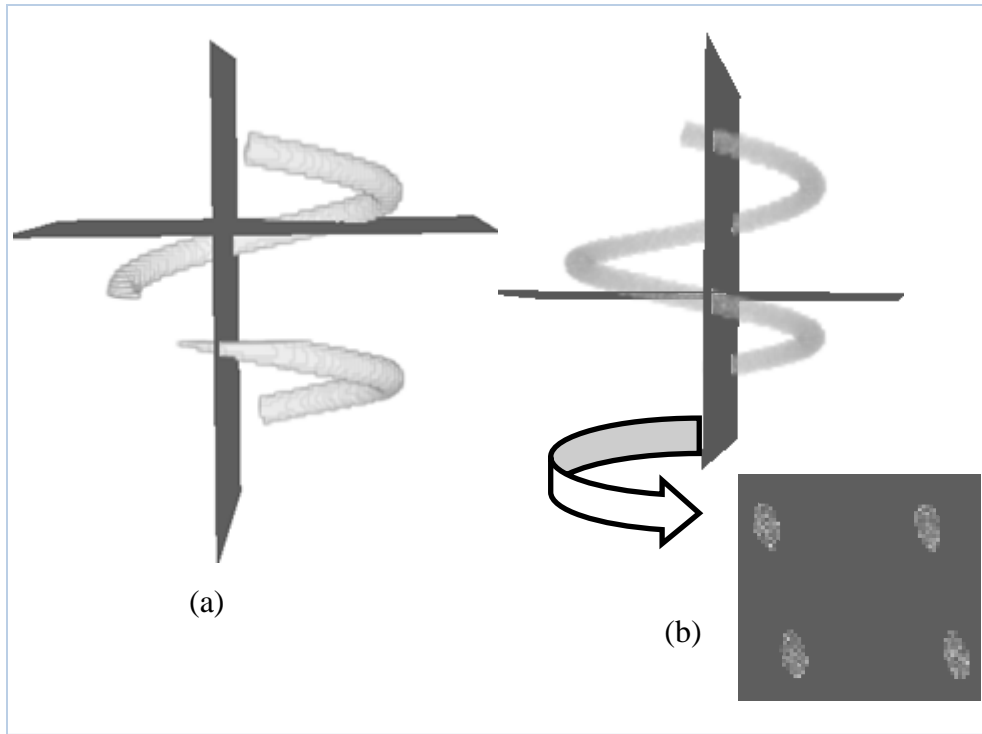


Fig. 38. Volume rendering of the Synthetic images. (a) corrupted volume where some of the slices' information is eroded (b) noisy volume.

Table 6. Quantitative validation of Segmentation using helix SSM

Volume	Shape Prior	Housdorff Distance Error	Mean Absolute Distance Error (MASD)	Std. Deviation
Noisy Volume	No	0.283	0.192	0.131
	Yes	0.265	0.177	0.091
Corrupted Volume	No	0.506	0.467	0.292
	Yes	0.251	0.1636	0.112

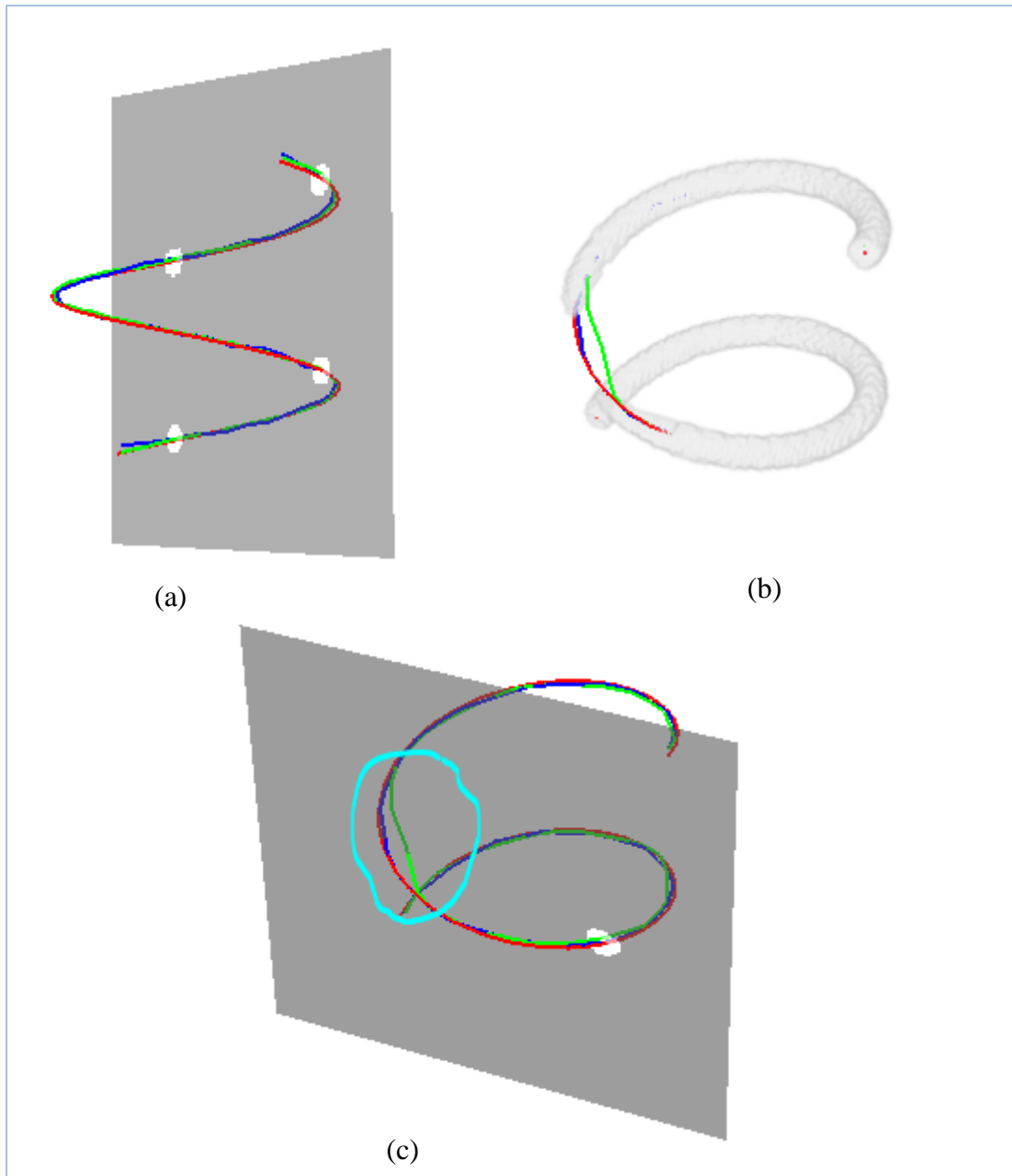


Fig. 39. Centerline Segmentation with and without shape priors of (a) noisy volume (b) and (c) corrupted volume.

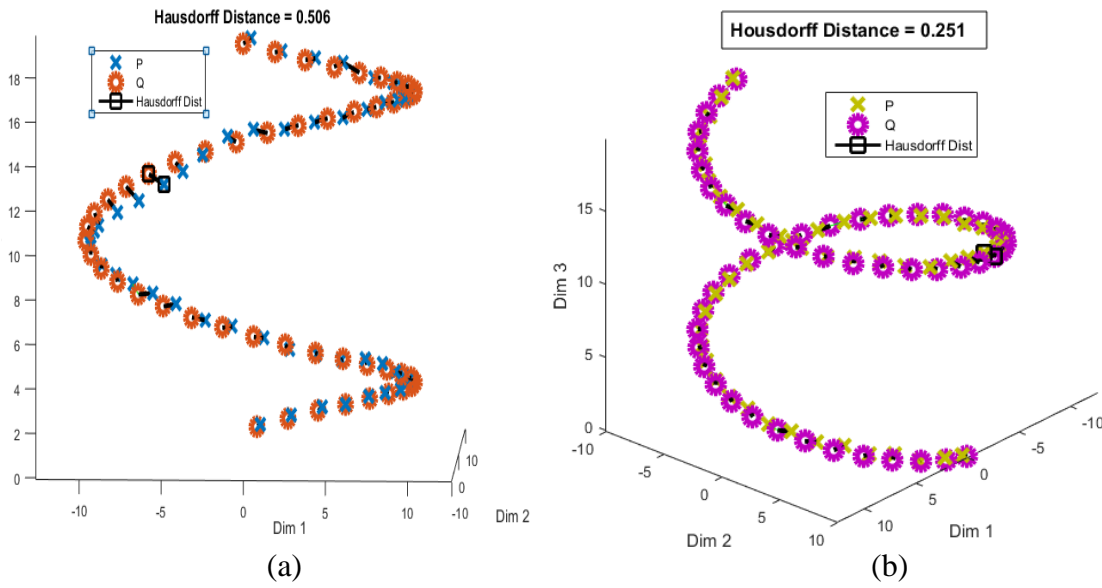


Fig. 40. Depiction of the Housdorff Distance (HD) for the corrupted volume,  $P$  is the segmented contour and  $Q$  is the ground truth (a) Segmentation without shape prior, HD is 0.506 mm. (b) Segmentation with shape prior, HD is 0.251mm.

## 5.7 Validation Using Patient Data

In this section, a validation of the proposed SSM-based segmentation is performed using patient  $T_2$ -weighted MRI data.

### 5.7.1 SSM Construction of Cranial Nerves

SSMs are constructed for the ten pairs (CNIII to CNXII) of brainstem cranial nerves. The training dataset for each of the nerves consists of 10 non-pathological samples, each of which is comprised of left and right centerline shapes of the nerve. Each training shape is extracted using the centerline tracking algorithm which is then manually corrected under the expert's supervision. SSMs are built by retaining 99% of total variance. In the ideal situation, the left and

right paths of a nerve centerline should be mirror images of each other, however in almost all cases they vary due to the presence of surrounding anatomical structures. The left centerline of a nerve extracted from a healthy patient can be considered as a variation of the right centerline, thus for each nerve, the left and right pools of training datasets are combined to construct a single SSM per nerve, offering two advantages: (1) the combination increases the training size from 10 to 20, and (2) the combined SSMs are unbiased regardless of left or right side of a nerve. In following sections, for each of the nerve SSMs, we show the point correspondence after GPA transform where each of the corresponding pointset are shown using different color balls. In addition to that, the modes of variation of the generated SSMs are shown.

The qualities of the constructed 10 SSMs are measured in terms of compactness, specificity and generality as described in Section 5.5. Specificity and generality are measures of error distances which are assessed in millimeters using Root Mean Square (RMS) method.

#### **5.7.1.1 CNIII**

For CNIII, separate SSMs are created for both left and right centerlines of the nerve to observe how much the two SSMs might vary from each other. The results are reported in Fig. 41. Both of the SSMs can capture 99% of shape variations using only 4 principal modes. Forty random shapes were used to compute the specificity measure. Both the compactness and specificity curves show similar characteristics while the generality of left CNIII SSM outperforms the SSM for the right CNIII by 0.02 mm.

The results of the combined left and right CNIII SSM is shown in Fig. 42. We have 20 segmented training shapes where 18 control points are used for each shape to establish the correspondence. For the combined training shapes, the first 5 modes were able to capture 99% of

the variations. The average specificity error is 0.28 mm with  $\pm 0.02$  mm standard deviation. We sampled 80 random shapes for the specificity measure. The generalization error converges to 0.18 mm with the worst mean error of 0.216 mm where the standard deviation is found negligible ( $\pm 0.009$  mm).

Shape variations for the combined CNIII along with the first three principal modes by  $\pm 3\sigma$  are shown in Fig. 43. Even though there are shape changes with respect to the mean shape in each of the mode, it is difficult to find meaningful differences because the centerline paths are open ended curves.

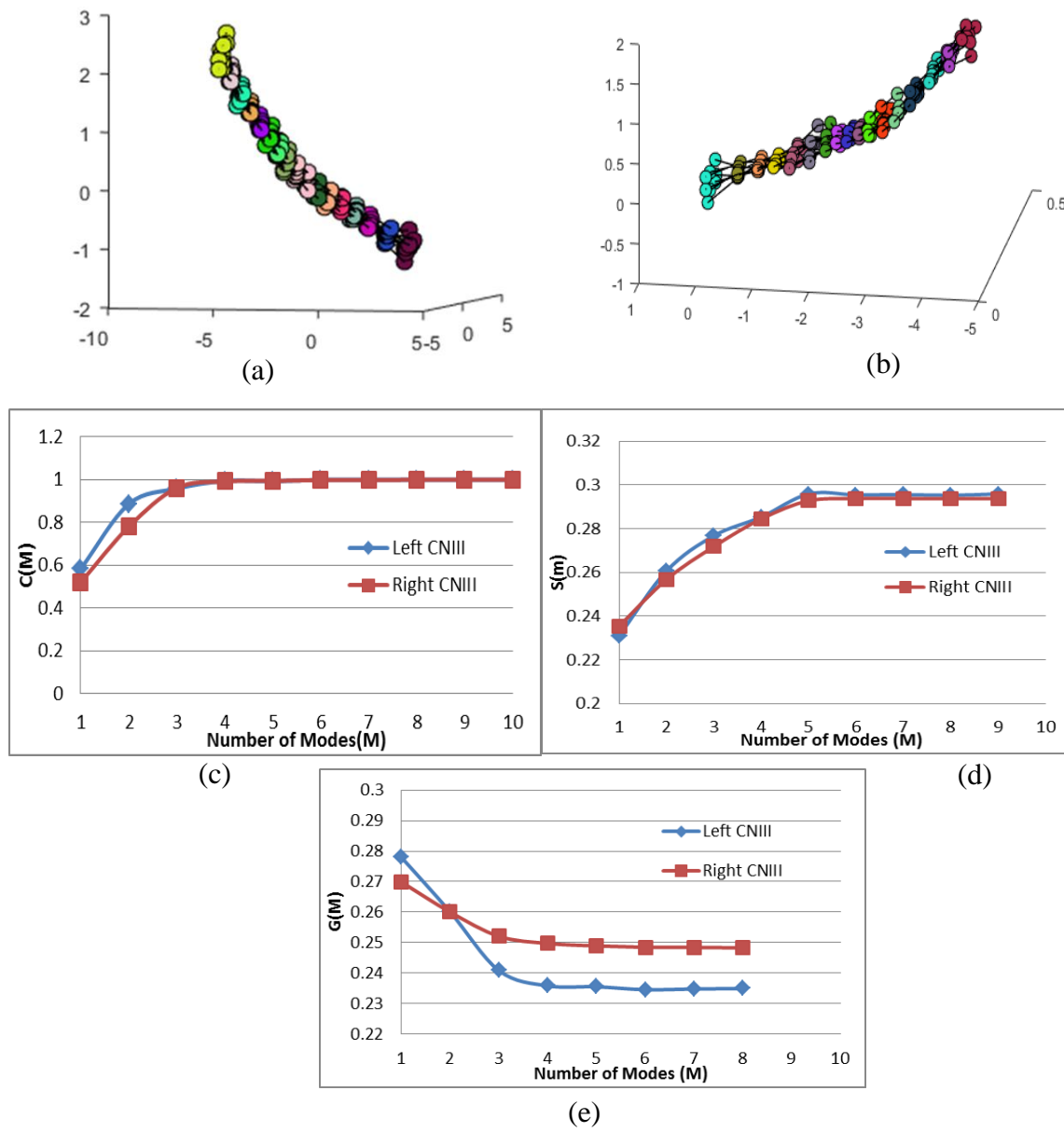


Fig. 41. SSM of left and right CNIII; (a) Shape correspondence of left CNIII; (b) Shape correspondence of right CNIII; (c) Compactness ; (d) Specificity ; (e) Generalization.

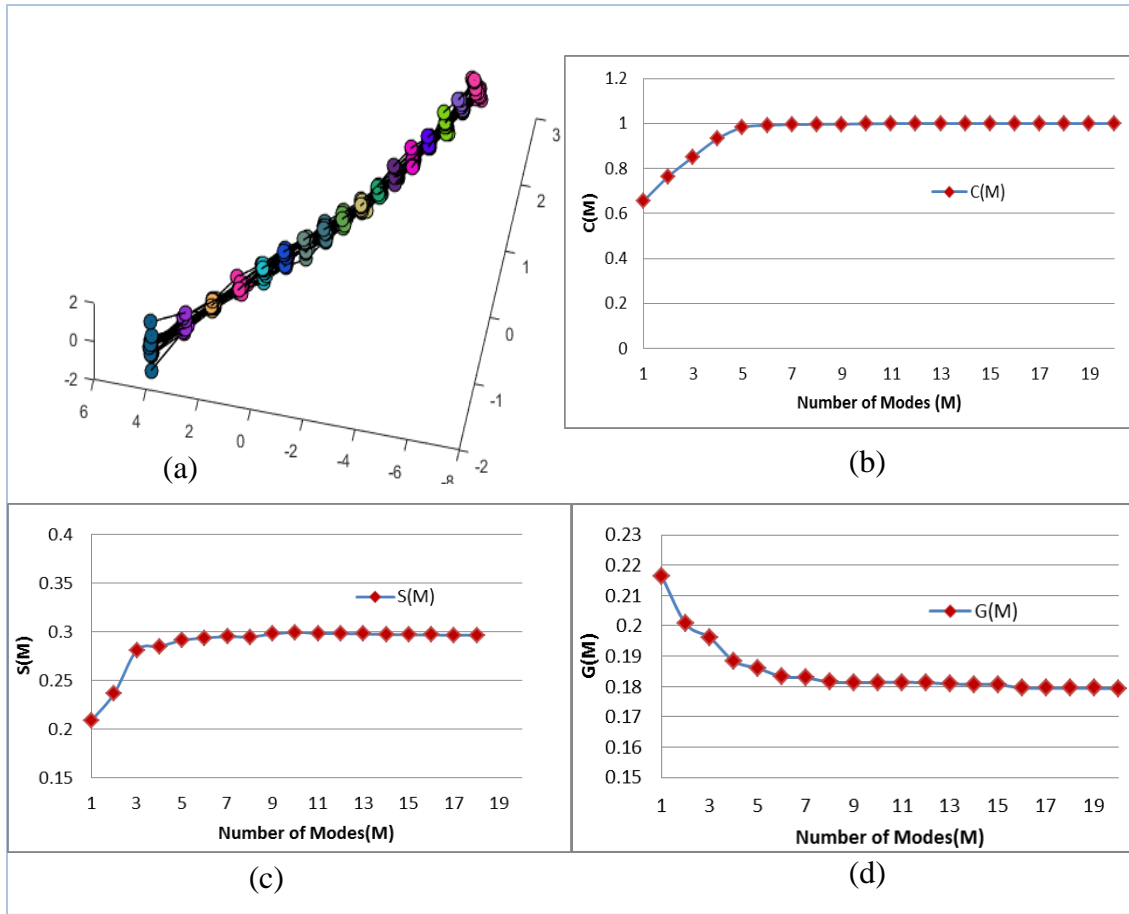


Fig. 42. SSM of the combined CNIII; SSM of the combined CNIII; (a) Shape correspondence; (b) Compactness; (d) Specificity; (d) Generalization.

### 5.7.1.2 CNIV

The trochlear nerve (CNIV) is the smallest nerve, which in turn contains the smallest number of axons [144]. Because of its size, a segmentation of this nerve can be quite challenging, even for neuroradiologists. Out of the ten patient datasets, CNIV was clearly visible in only seven datasets. Therefore, we had only seven pairs of segmented training shapes for this nerve. The point correspondence and measures of the SSM quality are shown in Fig. 44. The SSM for CNIV required six modes to capture 99% of variations of the training dataset. The

average generalization error is 0.18 mm with a standard deviation of 0.02, and the average specificity error is 0.28 mm with a standard deviation of 0.035.

Modes of variation for CNIV are depicted in Fig. 45. A variety in shapes has been observed for CNIV due to the close proximity of the vertebral artery. The tortuosity of the nerve might change when it is veered around the vertebral artery. The first mode captures the change of tortuosity of the nerve.

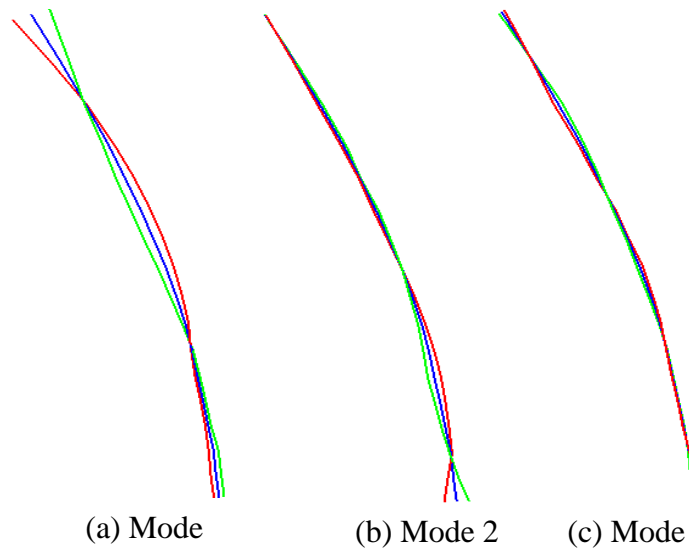


Fig. 43. Modes of Variation of Combined CNIII. Color code: Blue: mean shape; green: (mean +  $3\sigma$ ); red : (mean -  $3\sigma$ ).



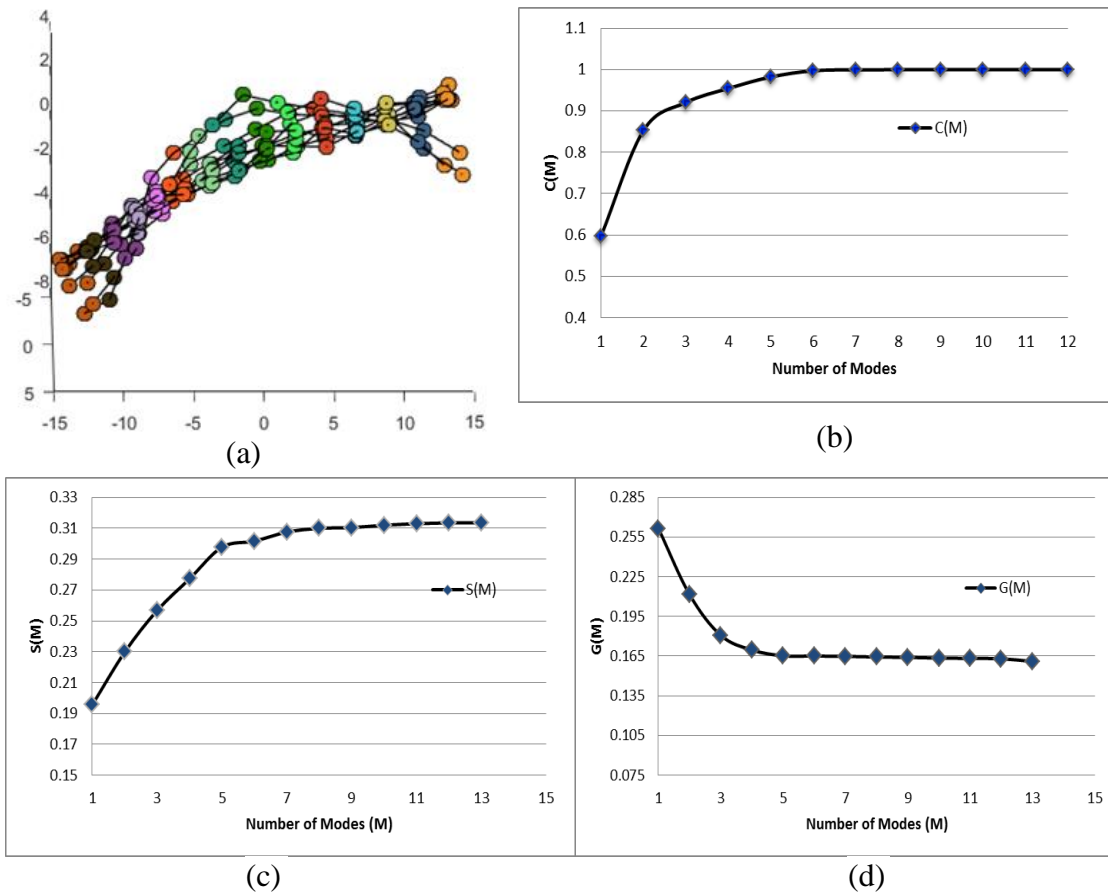


Fig. 44. SSM of CNIV. (a) Point correspondence (b) Compactness (c) Specificity and (d) Generality of the SSM.

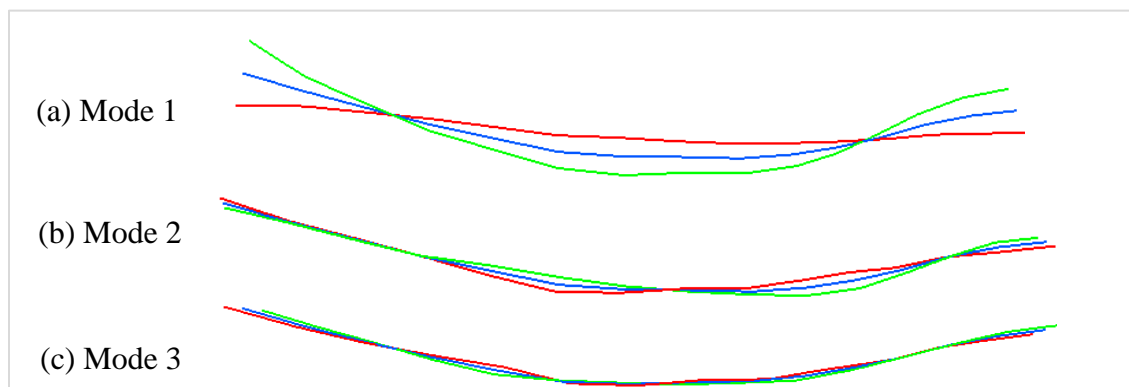


Fig. 45. Modes of Variation of CNIV. Blue: mean shape; green: (mean  $+3\sigma$ ); red: (mean  $-3\sigma$ ).

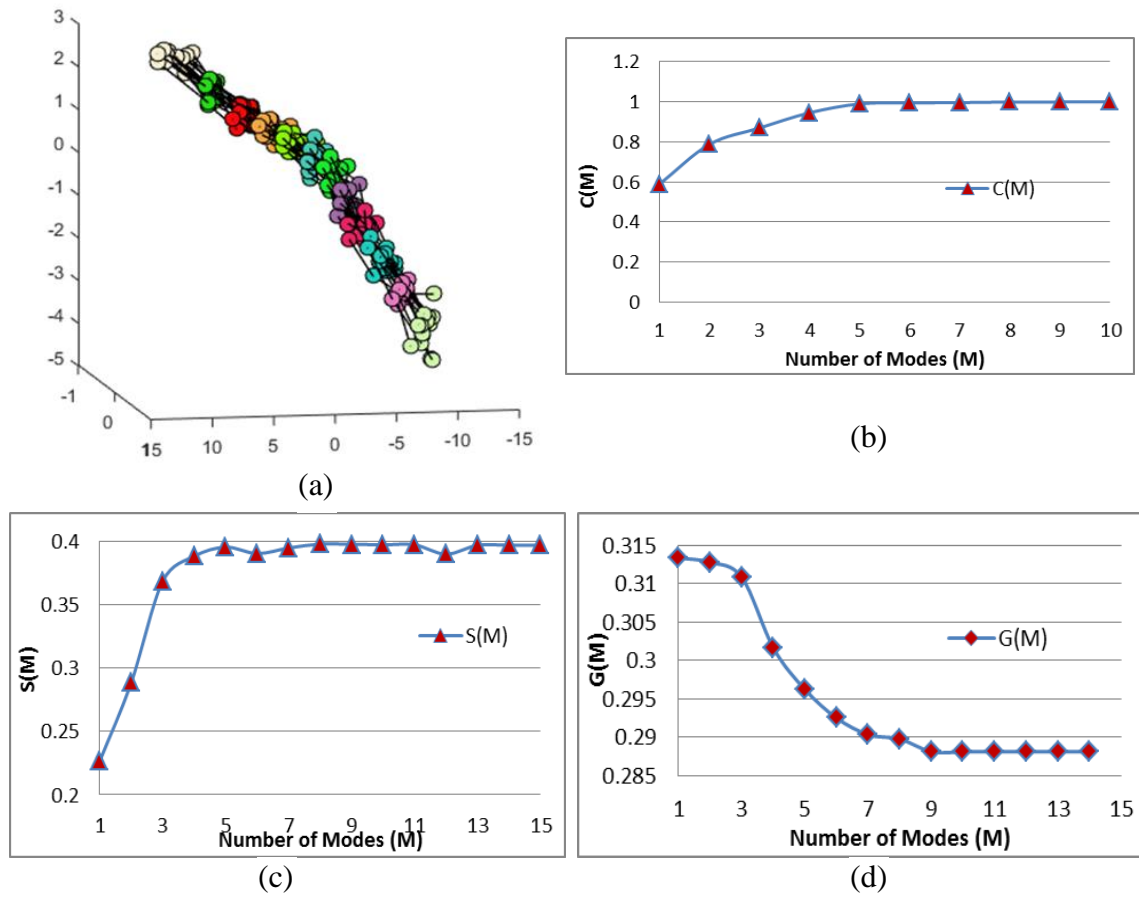


Fig. 46. SSM of CNV. (a) Point correspondence (b) Compactness (c) Specificity and (d) Generality of the SSM.

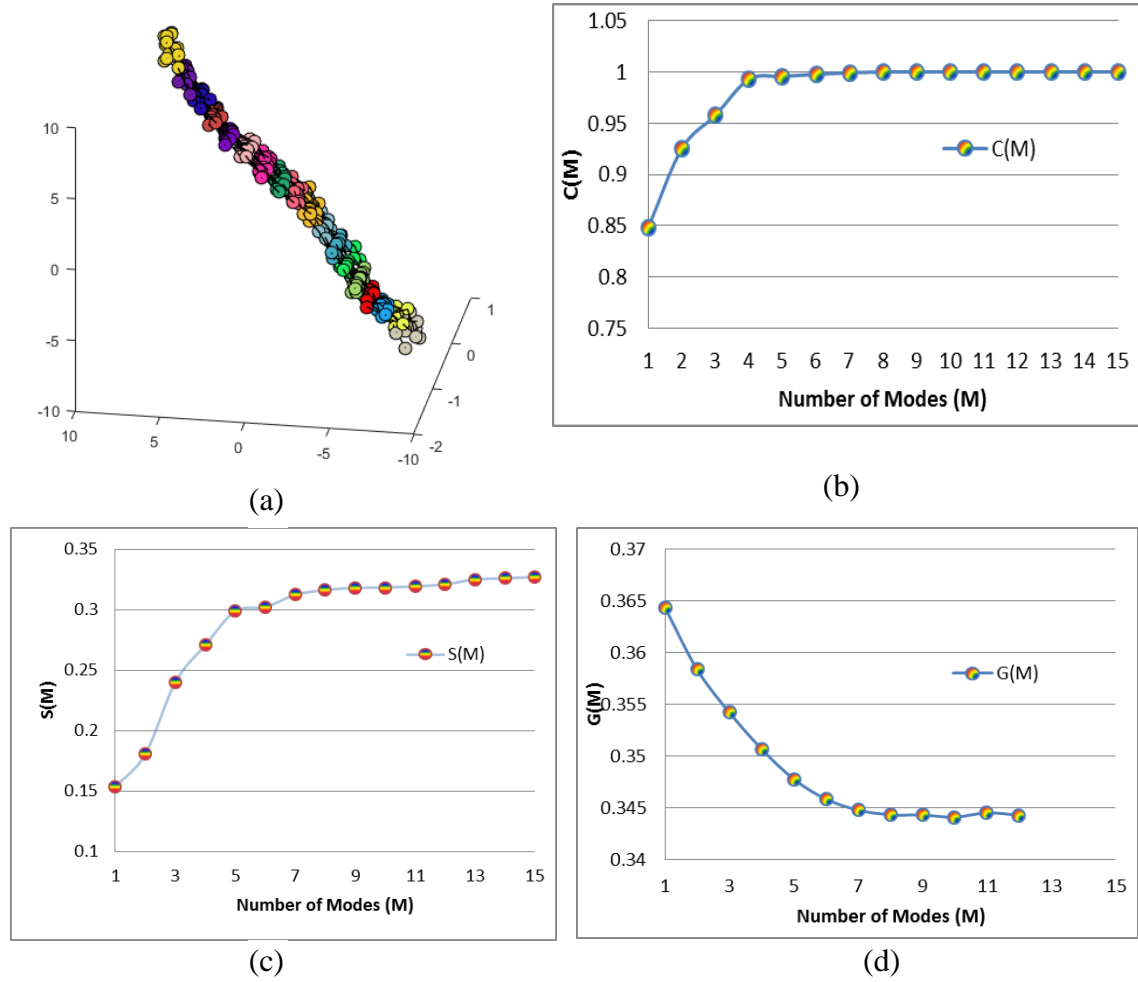


Fig. 47. SSM of CNVI. (a) Point correspondence (b) Compactness (c) Specificity and (d) Generality of the SSM.

### 5.7.1.3 CNV, CNVI, CNVII and CNVIII

SSMs for CNV, CNVI, CNVII and CNVIII are shown in Fig. 46, Fig. 47, Fig. 49 and Fig. 50 respectively. In these cases, five modes of variation are used to retain 99% variance of the training dataset, except for CNVIII which required four modes to sufficiently capture the same amount of variance. For this group of SSMs, the specificity measures were performed using 80 samples. Table 7 reports the specificity and generalization error for this group of nerves.

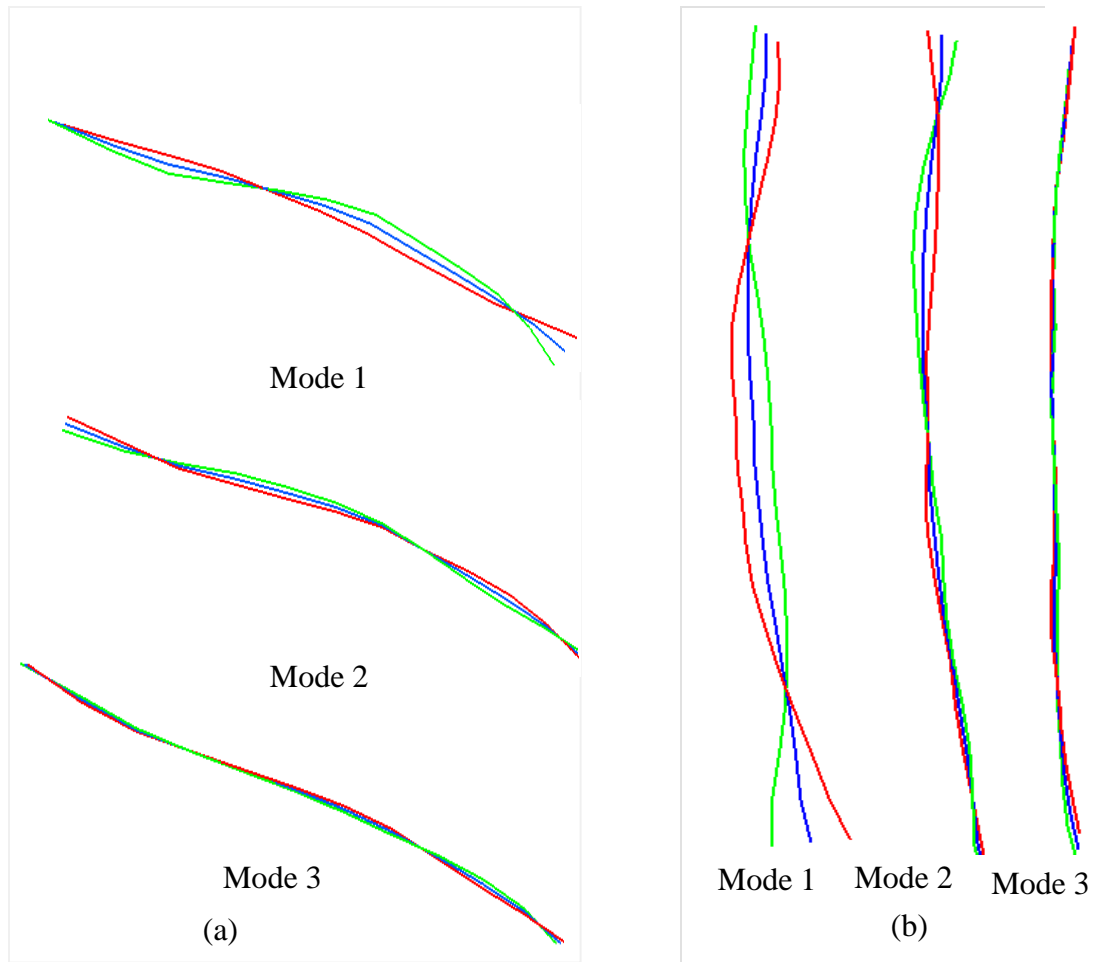


Fig. 48. Modes of Variation of (a) CNV and (b) CNVI.

Table 7. Generality and Specificity error for CNV to CNVIII

Nerves	S(M)	G(M)
CNV	$0.374 \pm 0.04$	$0.294 \pm 0.009$
CNVI	$0.287 \pm 0.03$	$0.176 \pm 0.02$
CNVII	$0.293 \pm 0.024$	$0.139 \pm 0.02$
CNVIII	$0.315 \pm 0.05$	$0.210 \pm 0.02$
<b>Average</b>	<b><math>0.32 \pm 0.04</math></b>	<b><math>0.247 \pm 0.02</math></b>

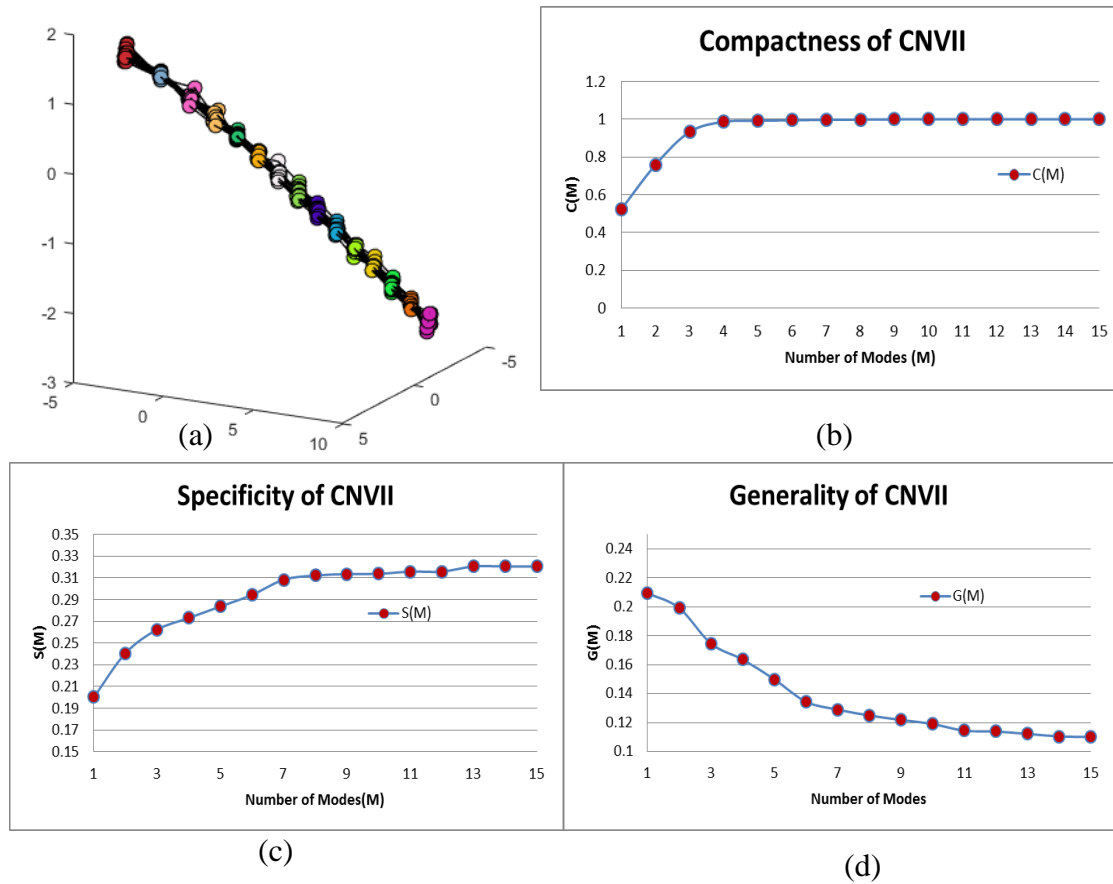


Fig. 49. SSM of CNVII. (a) Point correspondence (b) Compactness (c) Specificity and (d) Generality of the SSM.

The mean specificity error of this group is 0.32 mm with a confidence interval of 0.04 mm, the mean generalization error is  $0.24 \text{ mm} \pm 0.001$ , and the worst error of 0.34 mm in case of nerve CNVI. Shape variations along the first three modes within  $\pm 3\sigma$  of this group are shown Fig. 48, Fig. 51 and Fig. 52.

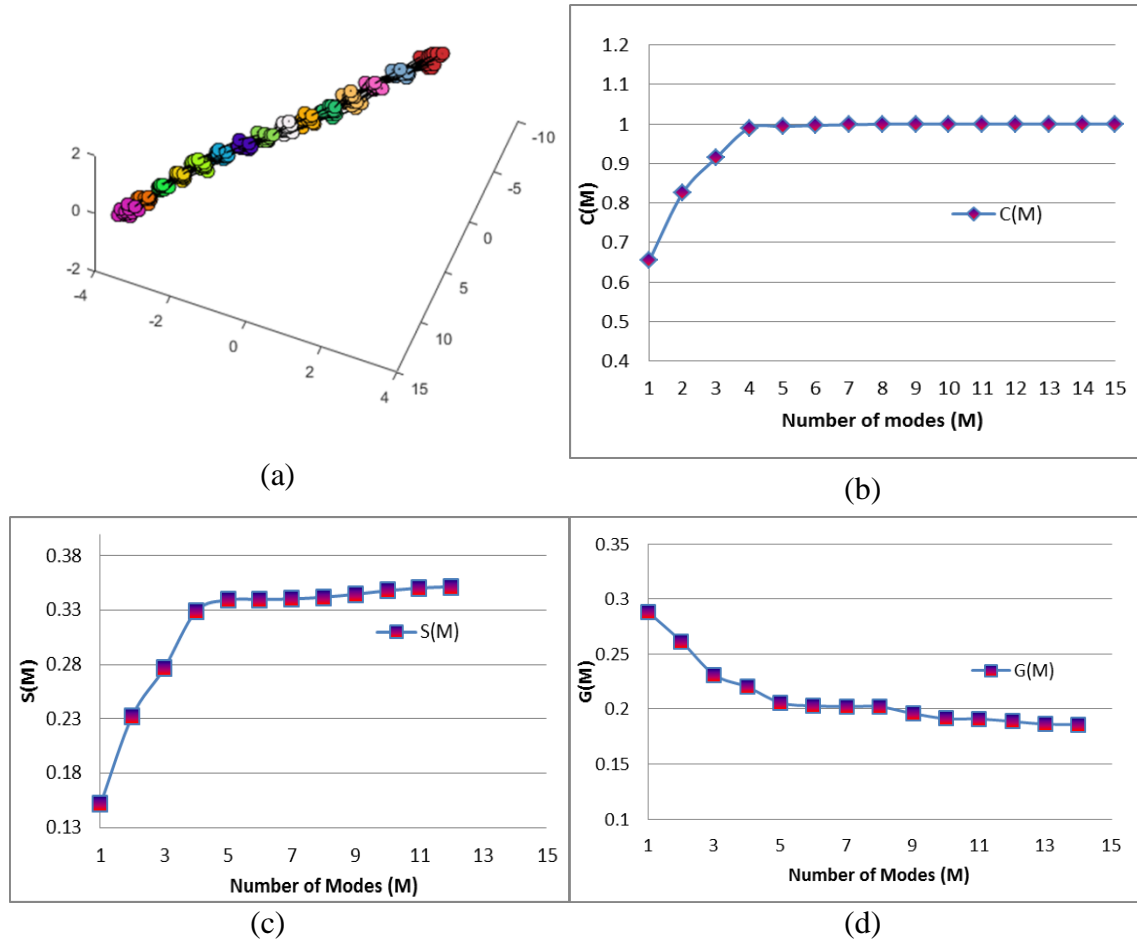


Fig. 50. SSM of CNVIII. (a) Point correspondence (b) Compactness (c) Specificity and (d) Generality of the SSM.

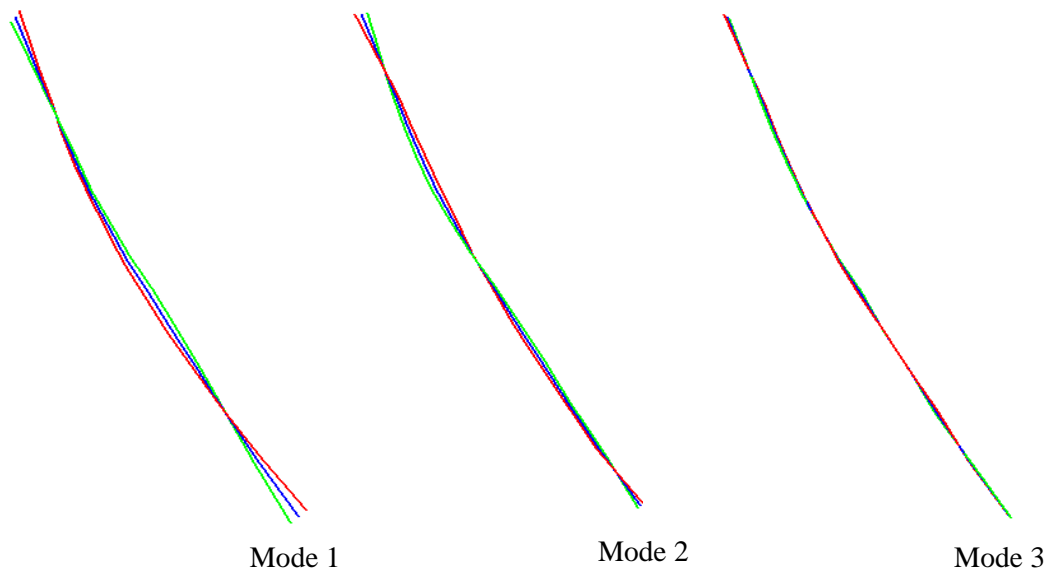


Fig. 51. Modes of Variation of CNVII.

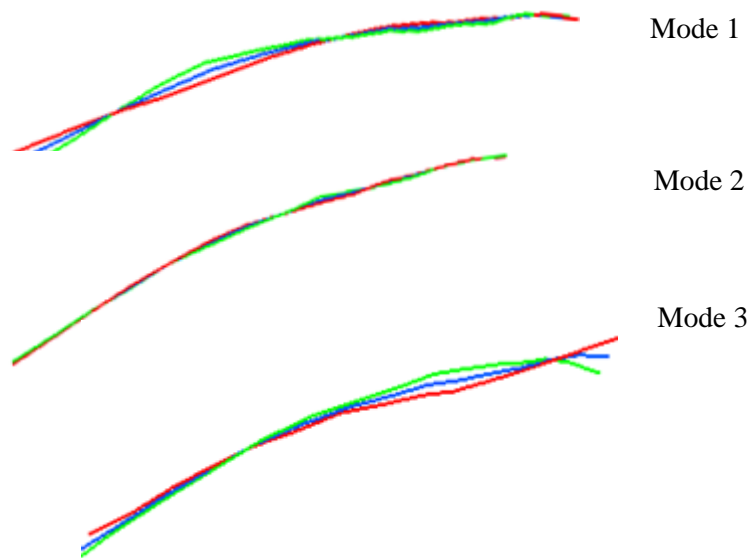


Fig. 52. Modes of Variation of CNVIII.

#### 5.7.1.4 CNIX, CNX, CNXI and CNXII

The lower cranial nerves include CNIX, CNX, CNXI and CNXII. This group has much smaller nerve radii which make it more challenging to segment from MRI data. For CNIX and CNX we were able to segment seven datasets, for a total of 14 shapes in the training dataset.

Similarly, we were not able to segment all the ten patient datasets for CNXI and CNXII. The training dataset of CNXI contains 16 shapes and CNXII contains 12 shapes. The measures of the SSMs are shown in Fig. 53, Fig. 55, Fig. 57, and Fig. 60 , with their shape variations Fig. 54, Fig. 56, and Fig. 58 and Fig. 61. The specificity and generality errors are summarized in Table 8. The specificity error is 0.356 mm with standard deviation 0.03, and the generalization error is 0.277 mm with standard deviation of 0.015 mm.

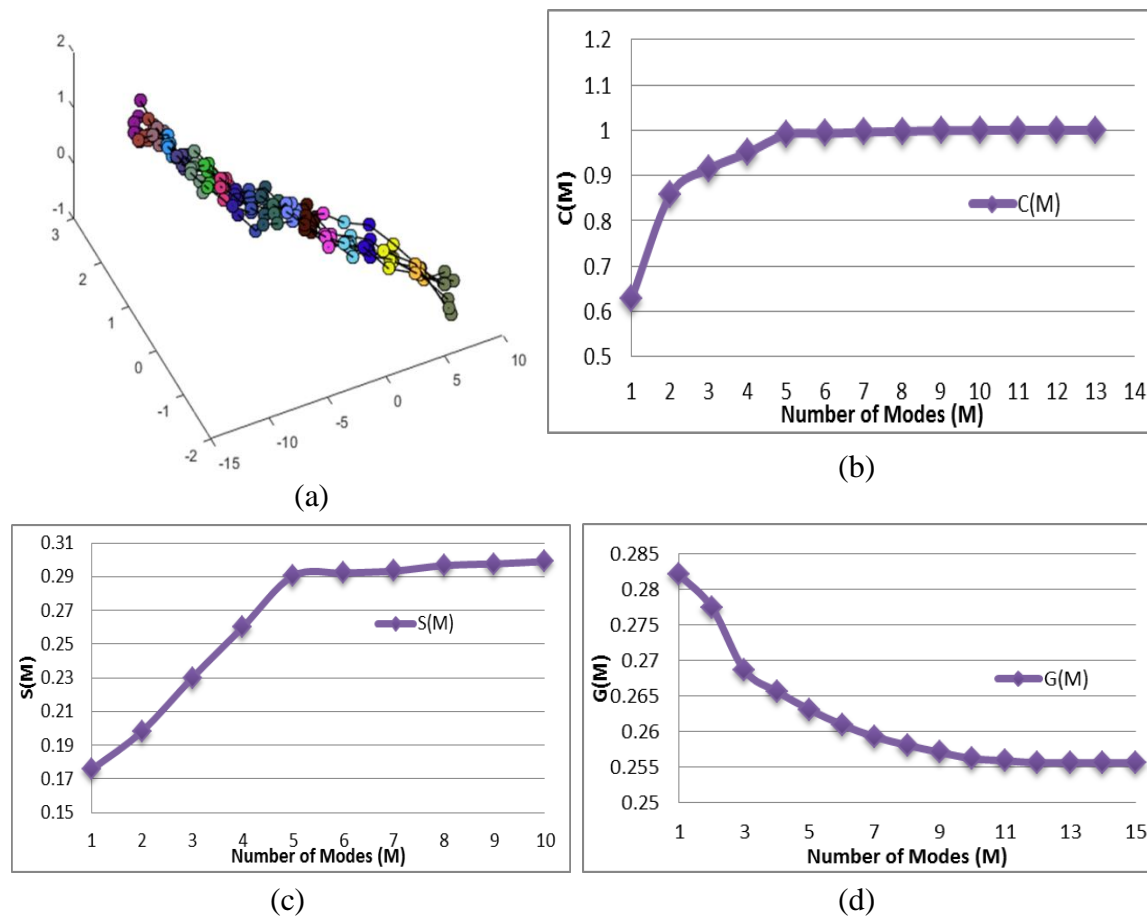


Fig. 53. SSM of CNIX. (a) Point correspondence (b) Compactness (c) Specificity and (d) Generality of the SSM.



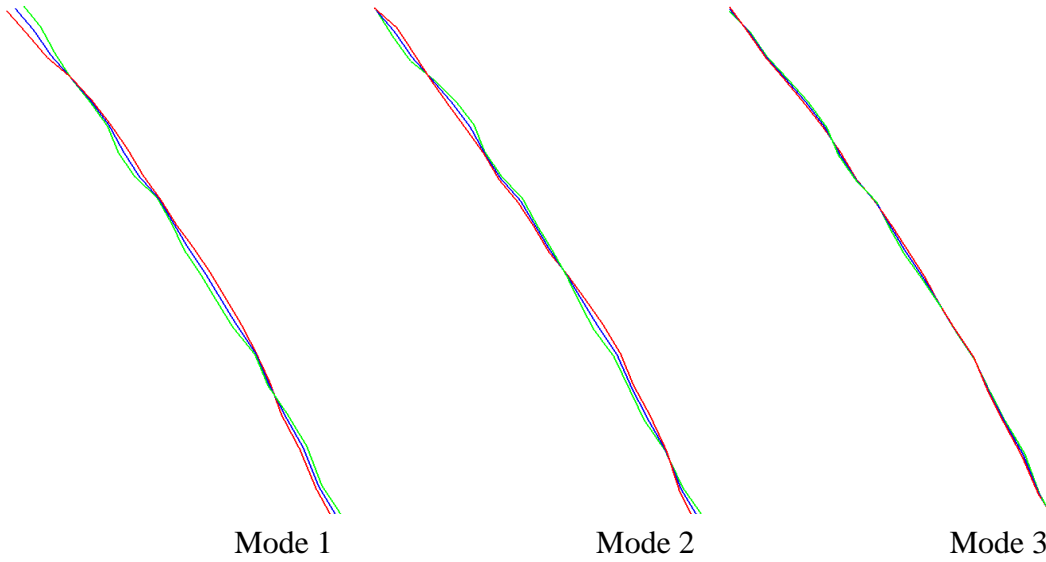


Fig. 54. Modes of Variation of CNIX.

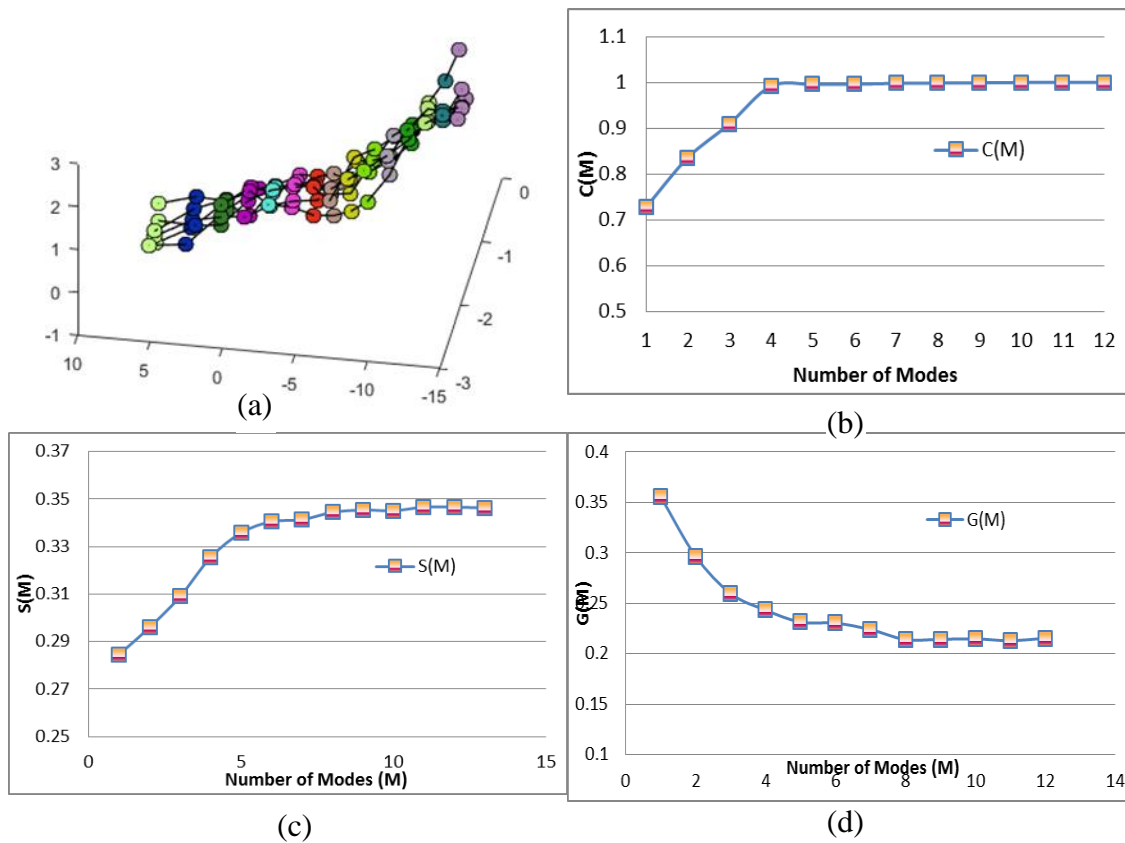


Fig. 55. SSM of CNX. (a) Point correspondence (b) Compactness (c) Specificity and (d) Generality of the SSM.

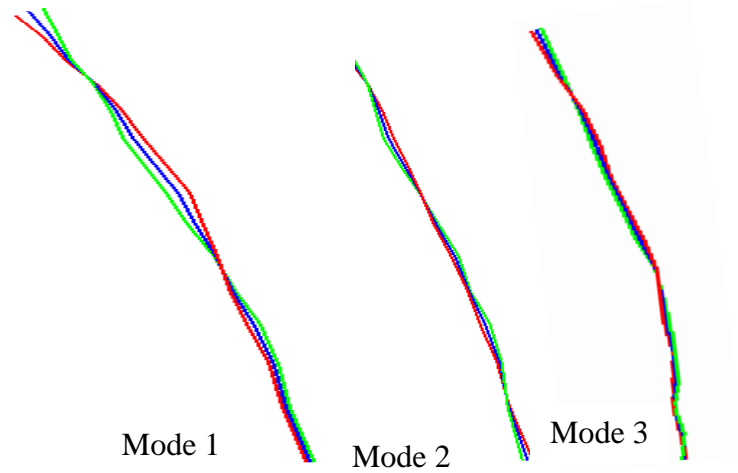


Fig. 56. Modes of Variation of CNX.

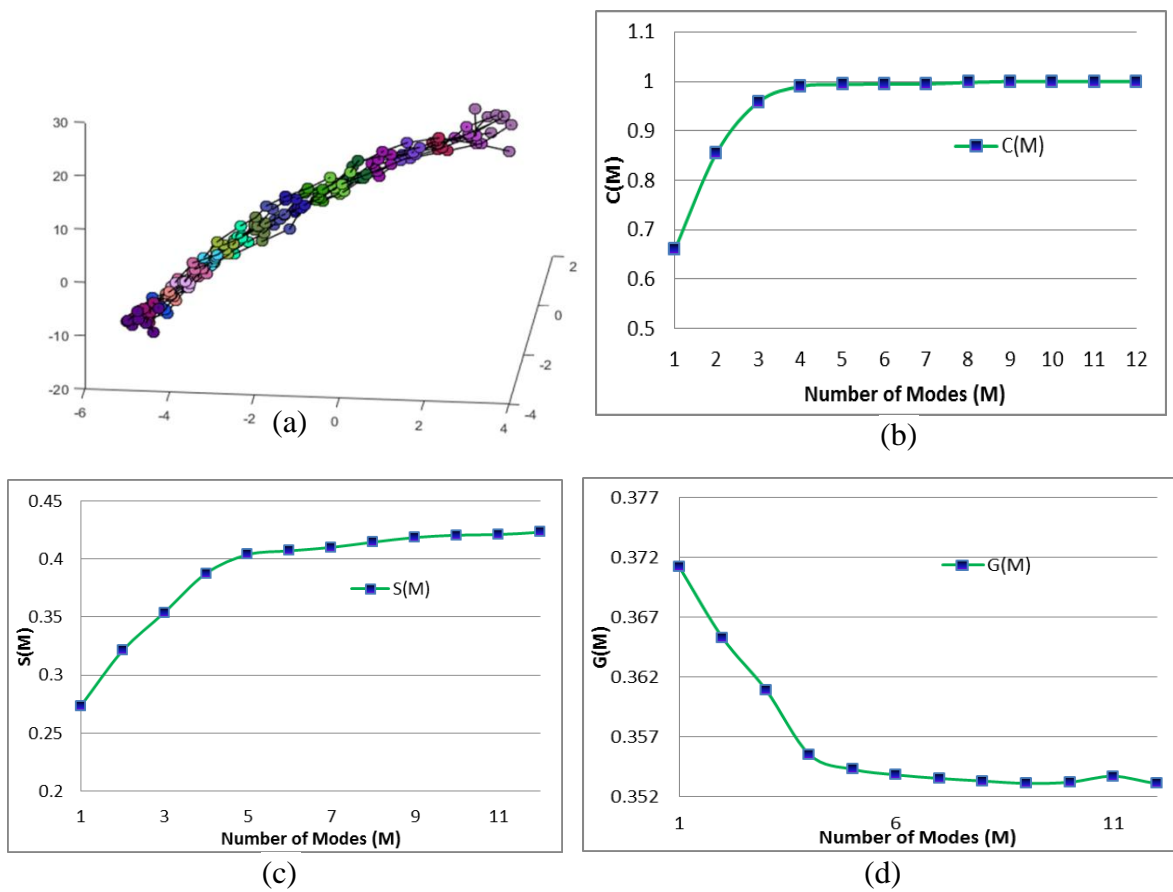


Fig. 57. SSM of CNXI. (a) Point correspondence (b) Compactness (c) Specificity and (d) Generality of the SSM

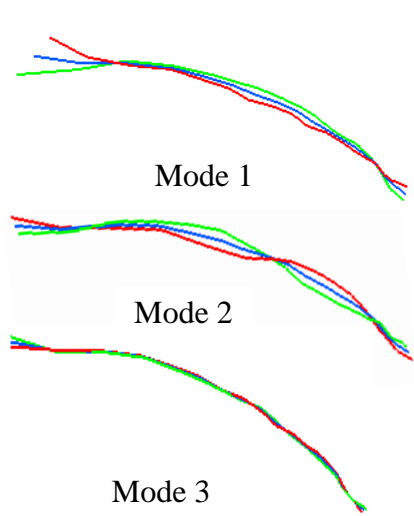


Fig. 58. Modes of Variation CNXI.

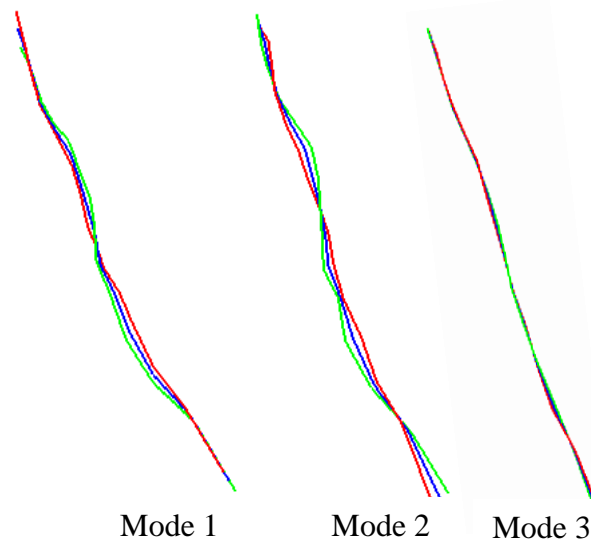


Fig. 59. Modes of Variation of CNX.

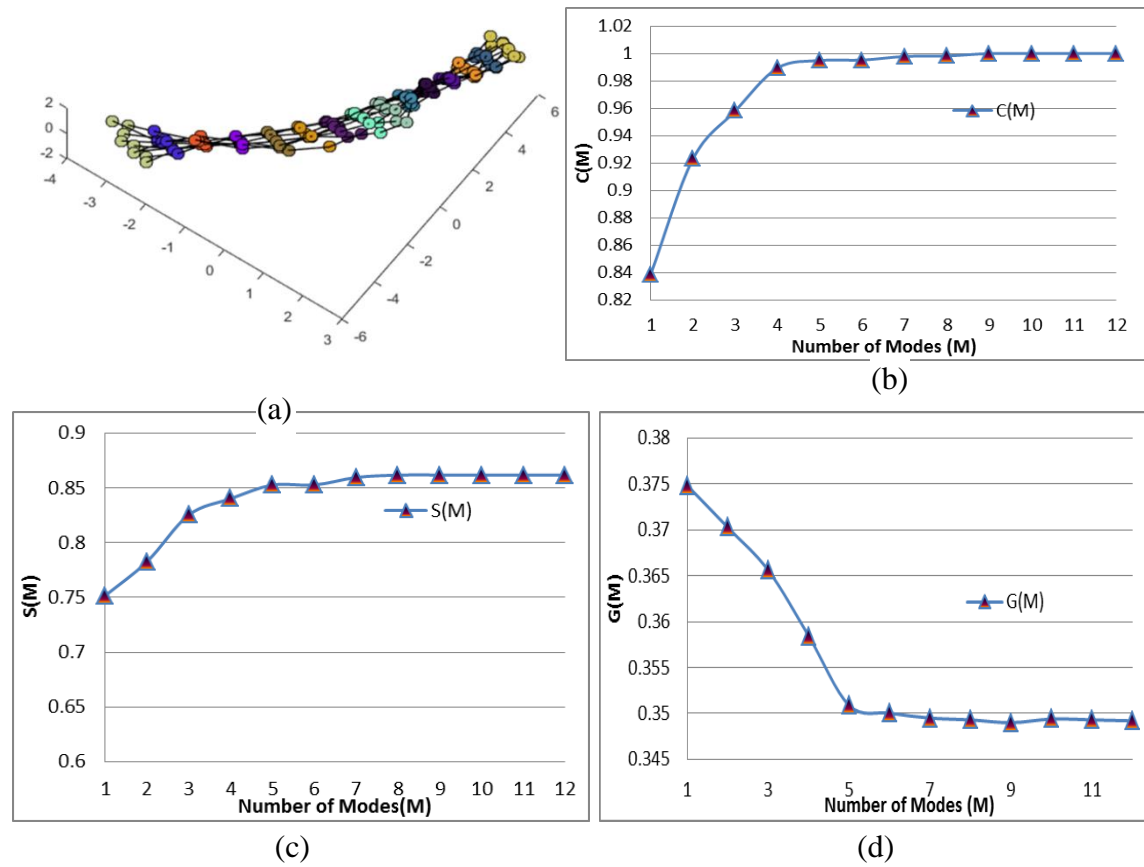


Fig. 60. SSM of CNXII. (a) Point correspondence (b) Compactness (c) Specificity and (d) Generality of the SSM.

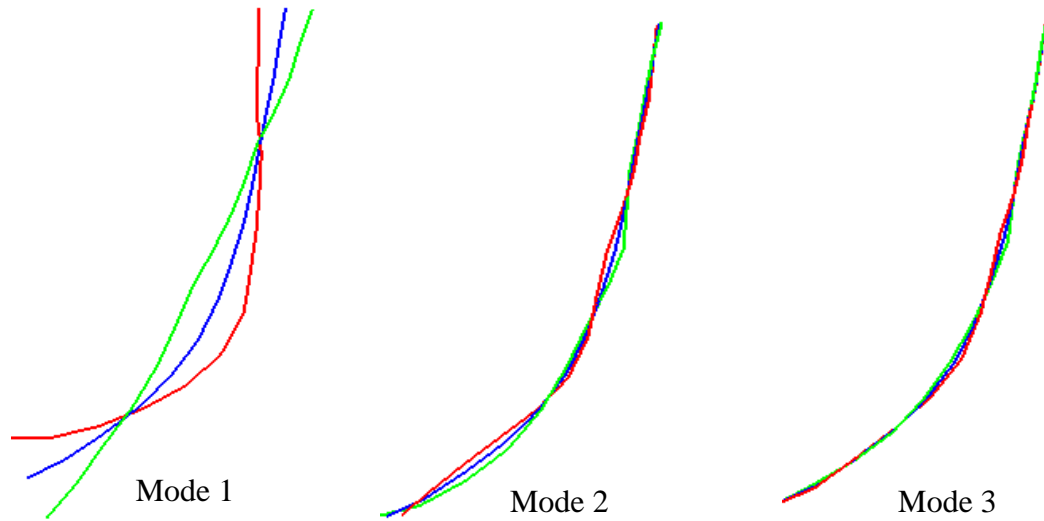


Fig. 61. Modes of Variation of CNXII.

Table 8. Specificity and Generality errors of lower cranial nerves.

Nerve	Specificity	Generality
CNIX	$0.263 \pm 0.04$	$0.264 \pm 0.007$
CNX	$0.331 \pm 0.02$	$0.240 \pm 0.04$
CNXI	$0.390 \pm 0.04$	$0.356 \pm 0.005$
CNXII	$0.439 \pm 0.03$	$0.249 \pm 0.009$
<b>Average</b>	<b><math>0.356 \pm 0.03</math></b>	<b><math>0.277 \pm 0.015</math></b>

### 5.7.2 Segmentation Using SSM Atlas

We assessed the performance of the SSM-based nerve segmentation algorithm using the collection of ten datasets. Segmentation was performed using the shape-based nerve atlas as well as without using the shape-based atlas to observe the differences. The segmentation of datasets is performed using leave-one-out procedure: first, a test image is selected from the pool and the

remaining images are used to build the SSM. Then the test image is segmented using the SSM to evaluate its performance. The process is iterated over all the 10 datasets.

We wish to observe the performance of the shape-based segmentation with respect to the ground-truth as well as with respect to the segmentation without shape information. To serve this purpose, we have performed the deformable model segmentation of all the ten datasets for the ten pairs of nerves without shape information. A non-normalized vesselness force is used as the external image force whereas the tangential and Laplacian forces are used as internal forces. Table 9 presents the results of the segmentation without shape-based force with respect to the ground-truth. The ground truth for each nerve is a piecewise-linear path computed by linear interpolation through a set of landmarks provided by an expert. From Table 9, it can be inferred that the average nerve segmentation error is  $0.28 \pm 0.16$  mm, which is less than the image voxel size. However, the deformable algorithm fails to ensure sub-voxel accurate centerline path for CNIV and CNXII, which are two of the smallest nerves and the two most difficult to segment. The mean distance of CNIV is  $0.582 \pm 0.34$  mm with the average HD of 0.601 mm and for CNXII the mean distance is  $0.805 \pm 0.405$  mm with an average HD of 0.752 mm. The main reason behind these poor results is that the vesselness image is unable to produce consistent external forces for all the voxels, especially in low resolution. One such situation is illustrated in Fig. 62. In this case, the vesselness filtering fails to capture the information of the very faint nerve line of the left CNXII. Thus, the segmentation produces an erroneous centerline as shown in Fig. 62(d): the black curve is the ground truth whereas the green curve is the 1-Simplex nerve centerline.

Table 9. Segmentation Results without shape information of fully visible dataset with respect to ground truth

Nerves	Mean Absolute Shape Distance (MASD)	Std. Deviation (SD)	Average Housdorff Distance (HD)
CNIII	0.198	0.10	0.3101
CNIV	0.582	0.340	0.601
CNV	0.186	0.129	0.293
CNVI	0.191	0.100	0.160
CNVII	0.225	0.110	0.190
CNVIII	0.130	0.095	0.243
CNIX	0.221	0.118	0.183
CNX	0.288	0.15	0.220
CNXI	0.141	0.118	0.183
CNXII	0.605	0.405	0.752
<b>Average</b>	<b>0.276</b>	<b>0.1665</b>	<b>0.313</b>
<b>Average excluding CNIV and CNXII</b>	<b>0.197</b>	<b>0.115</b>	<b>0.222</b>

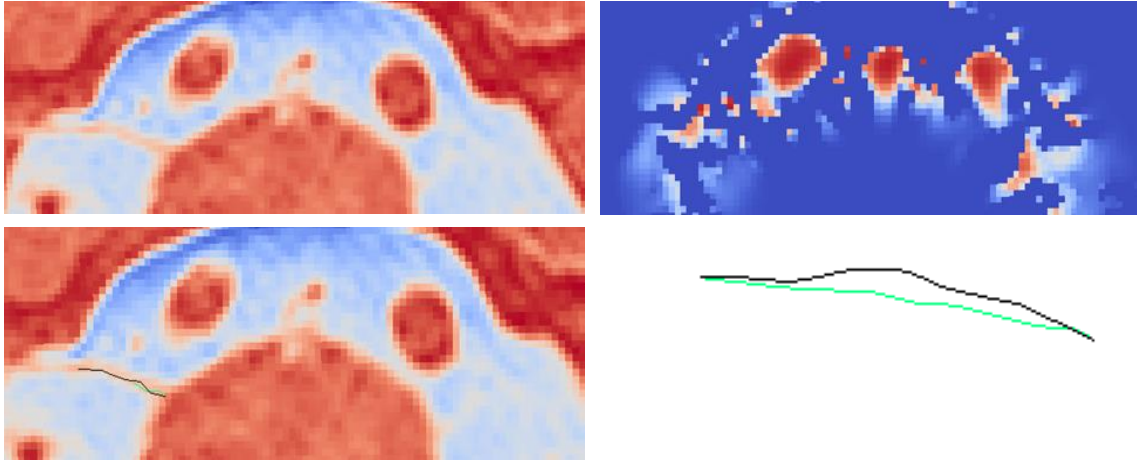


Fig. 62. Centerline computation of CNXII where vesselness filtering fails to capture tubularity information properly.

Table 10 summarizes the segmentation results using the shape-based atlas. The average MASD error for CNIV is decreased from  $0.582 \pm 0.340$  to  $0.212 \pm 0.112$ . The incorporation of SSMs also improved the segmentation of CNXII by decreasing the MASD error from  $0.605 \pm 0.405$  to  $0.223 \pm 0.115$ . The MASD error without SSM over all the nerves is  $0.197 \pm 0.11$  excluding the two nerves difficult to segment (CNIV and CNXII) as shown in Table 9, whereas the average MASD error with SSM is  $0.196 \pm 0.12$ . Therefore, no significant difference could be established between the two approaches in the case of all nerves excluding CNIV and CNXII. However, from an overall performance point of view ( $0.27 \pm 0.16$  vs.  $0.19 \pm 0.12$ ), we can infer that the segmentation error (the average MASD) decreased by 29% while using SSM. In terms of average HD, the SSM-based segmentation outperforms the segmentation without using SSM by improving HD by 32% (0.31 mm vs. 0.21 mm).

Table 10. Segmentation Results using shape-based atlas of fully visible dataset

Nerves	Mean Absolute Shape Distance (MASD)	Std. Deviation (SD)	Average Housdorff Distance (HD)
CNIII	0.202	0.121	0.176
CNIV	0.212	0.112	0.195
CNV	0.145	0.166	0.19
CNVI	0.186	0.148	0.281
CNVII	0.22	0.13	0.206
CNVIII	0.197	0.12	0.223
CNIX	0.171	0.131	0.233
CNX	0.223	0.07	0.125
CNXI	0.185	0.132	0.271
CNXII	0.223	0.115	0.27
<b>Average</b>	<b>0.196</b>	<b>0.124</b>	<b>0.211</b>

### 5.7.3 Segmentation of Corrupted/Noisy/Partially Visible Dataset

To assess the robustness of the SSM-based segmentation, we applied the method in a dataset where nerves are not fully visible due to image noise and partial volume effects. Table 11 shows the quantitative segmentation results of the dataset w.r.t. the ground-truth. We compute The MASD error in millimeter unit. In most of the cases, the generated ground-truth centerlines are not smooth because only a few points could be manually selected from the slices that show the nerve. The average segmentation error without SSM is 0.32 mm, which decreased to 0.28 mm with SSM. Therefore, we can conclude that the overall segmentation error is improved by 13% for this specific dataset. The improvement in segmentation is observed for all the cranial nerves (CNIII to CNXII), as shown in Fig. 63. For instance, the SSM-based segmentation of



CNIV has a huge improvement from 0.45 mm to 0.31 mm as shown in Fig. 64. The cropped volume containing CNIV is shown in Fig. 64 (a), the nerve area is magnified in Fig. 64 (b) and the segmented nerves are shown in Fig. 64 (c). The segmentation error is improved by 30% when using shape-based forces.

Table 11. Segmentation Results of the partially visible dataset

Nerves	Segmentation error without SSM	Segmentation error using SSM
CNIII	0.31	0.28
CNIV	0.45	0.31
CNV	0.27	0.25
CNVI	0.30	0.27
CNVII	0.23	0.20
CNVIII	0.28	0.26
CNIX	0.38	0.32
CNX	0.35	0.31
CNXI	0.31	0.29
CNXII	0.33	0.31
<b>Average</b>	<b>0.32</b>	<b>0.28</b>

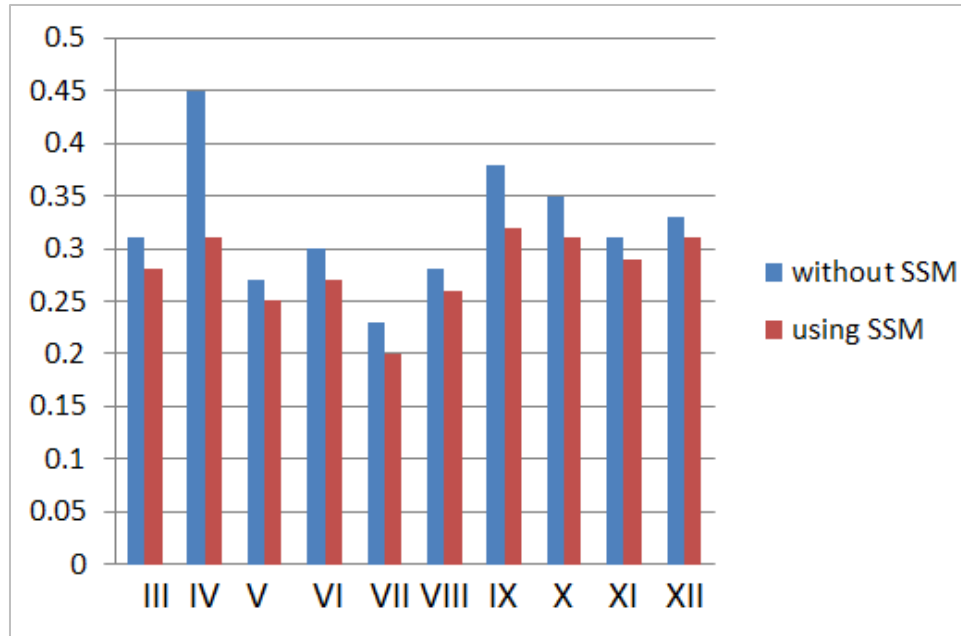


Fig. 63. Graphical comparison of segmentation algorithms with and without SSM using partially visible dataset.

In the case of CNX, for this specific dataset, the slices containing the right side of the nerve have partial volume effects that mix nerves with cerebellar peduncles as shown in Fig. 65. As a result, the right CNX cannot be clearly detected in the dataset. The segmentation error decreases by 8% after incorporating shape-based forces. For the left CNX, segmentations with and without an SSM force performs almost similarly because of the clear gradient around the nerve even though the image is noisy.

The most challenging nerve to segment is CNXII which can barely be seen in this specific dataset as depicted in Fig. 66. In addition, a deformity on the left CNXII has been observed due to the difference in the size of the vertebral artery. The left vertebral artery is much bigger than the right one which pushes the nerve in the downward direction as shown in Fig. 66 (a).

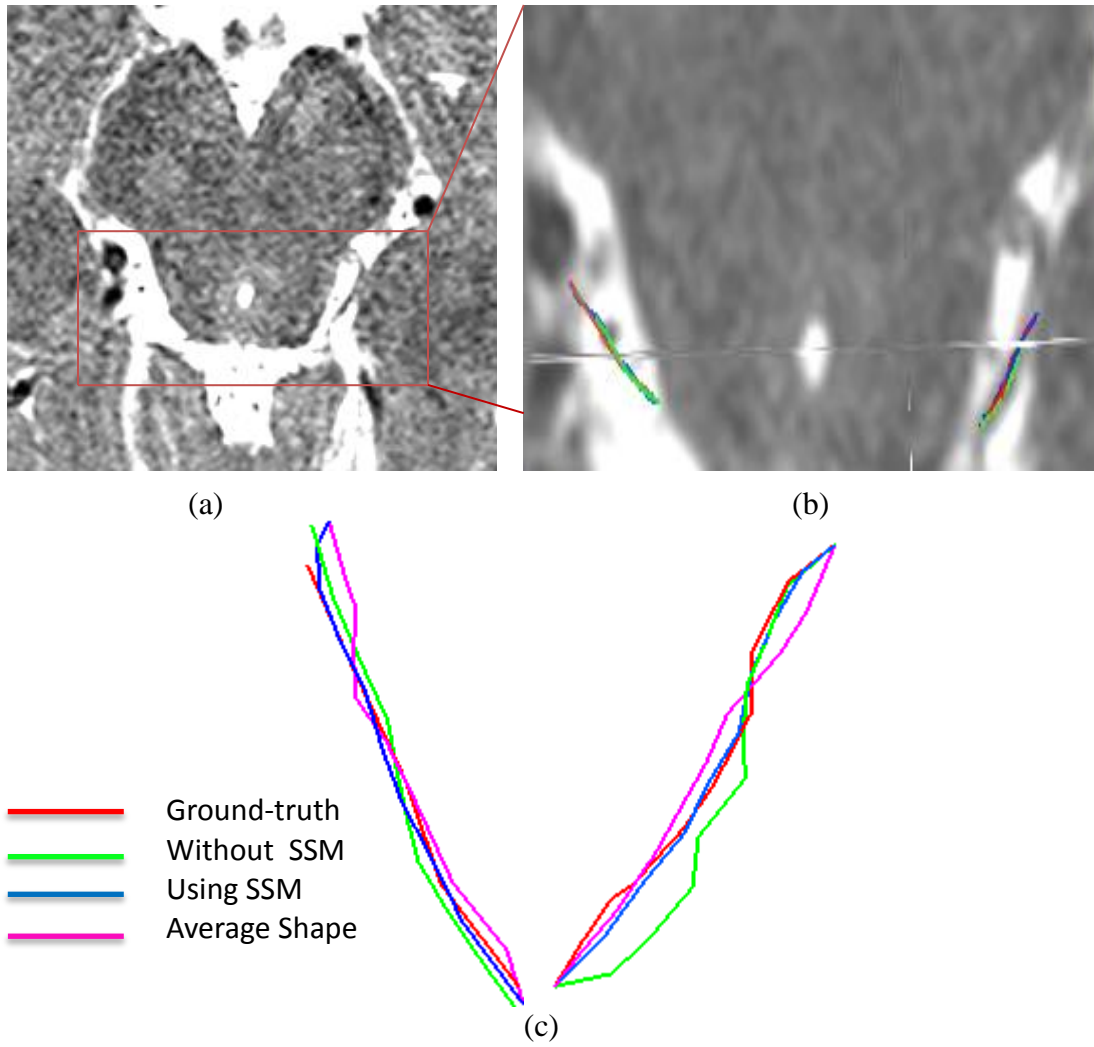


Fig. 64. Centerline segmentation of CNIV from the corrupted dataset. (a) Axial slice containing CNIV; (b) Extracted centerlines superimposed on the slice of (a); (c) extracted centerline path – red is the ground-truth, blue is SSM-based segmentation, green is without SSM segmentation, purple is the average shape.

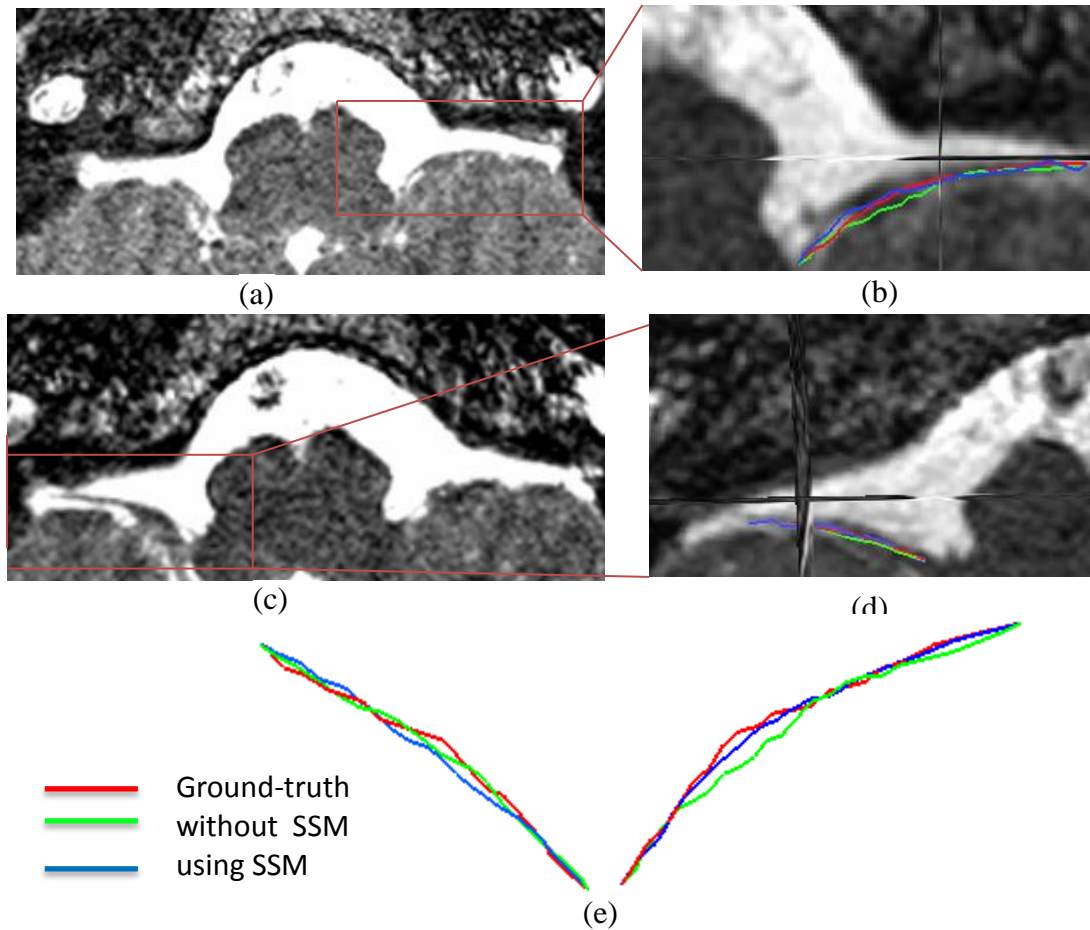


Fig. 65. Centerline segmentation of CNX from the noisy dataset. (a) Axial slice containing right CNX; (b) Extracted centerlines superimposed on the magnified slice of (a); (c) Axial slice containing left CNX; (d) Extracted centerlines superimposed on the magnified slice of (c); red is the ground-truth, blue is SSM-based segmentation, green is without SSM segmentation.

An exception is observed in the left-side of CNXII. The computed average shape model for left CNXII is offset from the ground-truth nerve resulting in an incorrect nerve centerline as shown in Fig. 66 (b) and Fig. 66 (d). In this case, the average shape which we use for initial model registration is closer to the vertebral artery (which is also a tubular structure) than the nerve. As a result, the strong gradient of the artery pulls the initial average model towards the

artery during the model deformation. The reason behind this situation is that our SSM is built using a very limited number of training shapes while not considering this large variation. In this scenario, we decided to turn off the SSM-based forces and then allow the model to deform without shape priors.

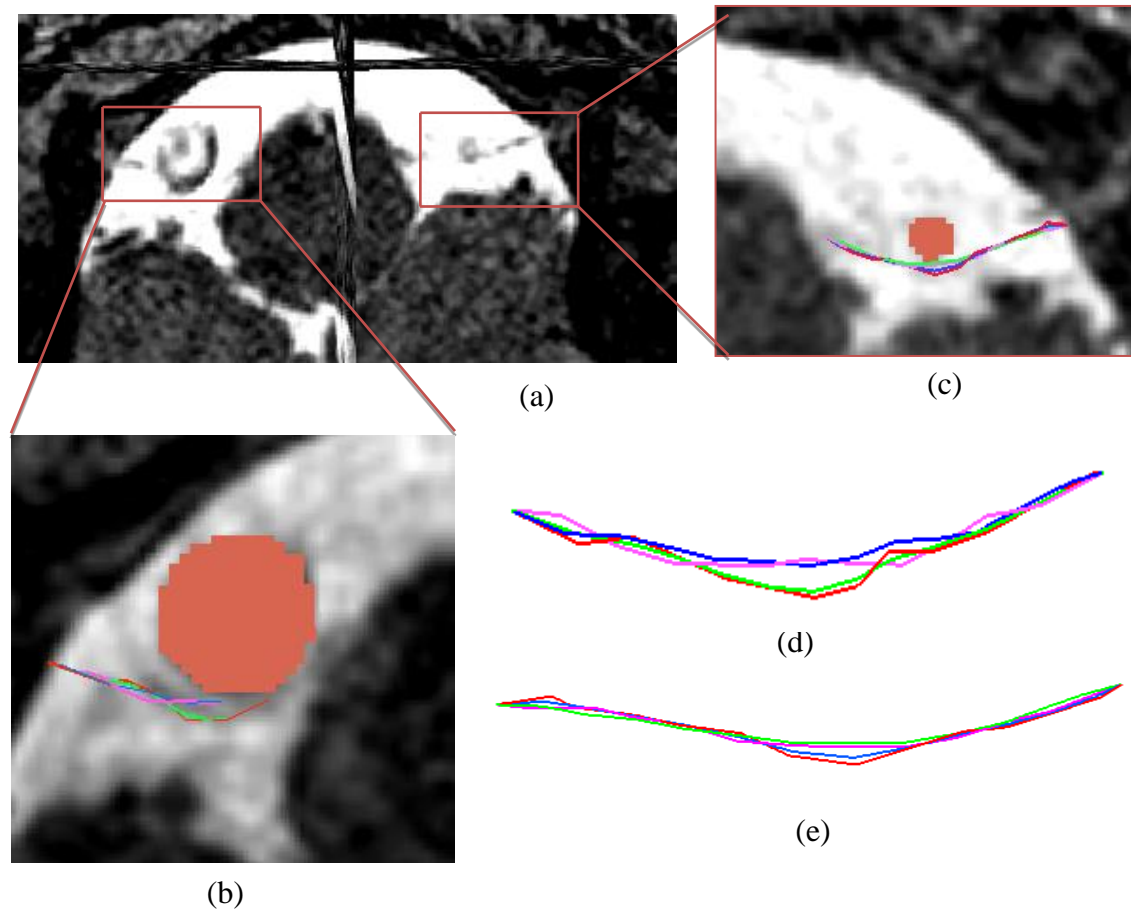


Fig. 66. Segmentation of CNXII from noisy data. (a) Axial slice containing CNXII; (b) Extracted left centerlines superimposed on the magnified slice of (a); (c) extracted right centerline paths superimposed on the magnified slice of (a); (d) left and (e) right centerline models. Color code: red - ground-truth, blue - SSM-based segmentation, green: without SSM segmentation and purple: average shape.

The deformation results of the left CNXII shows an average error of 0.35 mm with respect to the ground-truth centerline as shown in Fig. 66 (b) and Fig. 66 (d). On the other hand, the right CNXII has the usual shape that falls within our training shapes. Therefore, the SSM-based segmentation generated the centerline with 75% accuracy (average error is 0.25 mm) with respect to the ground-truth centerline.

## 5.8 Conclusion

To improve the accuracy and robustness of segmentation results, shape information is incorporated as a prior knowledge into the discrete deformable 1-Simplex model. Shape information is encoded within a Statistical Shape Model. Correct and meaningful shape correspondence is vital for the construction of any shape model. Dense point correspondence is feasible for sparse 2D shapes. However, it is almost impossible for 3D structures because of high overhead, poor repeatability and image artefacts of MRI data. A non-parametric particle-based dense point correspondence method is chosen which has the advantage of performing homologous point distribution automatically over the contour shapes. An average shape as a first order statistics and covariance matrix of the training dataset as a second order statistics are computed and integrated with the 1-Simplex deformable model to derive an internal shape-based force. This shape-based force along with other internal and external force is used for final centerline deformation.

A through validation is performed using both synthetic and patient MRI data. SSM models constructed for all the 10 cranial nerves by combining their corresponding left and right side models. SSM of each nerve is shown using three benchmark evaluation criteria: compactness, generalization and specificity. Cranial nerves can be divided into two groups based

on their attachment to the brainstem: upper cranial nerves (CNIII to CNVIII) and lower cranial nerves (CNIX to CNXII). Upper cranial nerves are comparatively bigger and easy to trace than lower cranial nerves, only exceptional is CNIV. The average Generalization error for upper cranial nerves' SSM is slightly better than the lower cranial nerves ( $0.247 \pm 0.02$  mm compared to  $0.277 \pm 0.015$ mm). Similarly, the specificity error is slightly increased in lower cranial nerves ( $0.32 \pm 0.04$  mm vs.  $0.356 \pm 0.03$ mm).

The performance of the SSM-based deformable atlas is assessed using fully visible and partially visible datasets. In case of fully visible datasets, both the average MASD and Housdorff distance decreased by 8% and 10% respectively, over the segmentation without SSM atlas. However, a noticeable improvement was found in case of critical nerves such as CNIV and CNXII. On the other hand, in case of partially visible datasets, an improvement is observed for the 10 pairs of nerves. The segmentation error i.e. average MASD improved by 12% when the SSM-based atlas is incorporated.

## CHAPTER 6

### CONCLUSIONS AND FUTURE WORKS

There is a critical need in neurosurgical planning and simulations for accurate and robust 3D patient-specific models of critical tissues including cranial nerves. In this work, we have developed a segmentation method for the ten pairs of brainstem cranial nerves from CNIII (the oculomotor nerve) to CNXII (the Hypoglossal nerve) in MRI data using a deformable digital atlas of cranial nerves.

#### 6.1 Discussion

The *first* contribution of this research is a novel nerve medial axis extraction technique using a 1-Simplex based discrete deformable model where we combine the 3D contour model to achieve a robust medial axis identification, starting from an initialization based on tubularity detection featuring multiscale Hessian-based vesselness and Minimal Path computation. Because of its discrete nature, it is easier for a 1-Simplex curve to adapt locally and to find an accurate fit to a particular shape in comparison with a parametric representation that is implicitly regularized. Therefore, a discrete representation of a nerve ensures subvoxel-accurate results even at the thinnest nerve, which has a diameter of less than two voxels in the MR image.

Our *second* contribution is to employ the 2-Simplex deformable surface model, using the centerline as initialization, into a highly accurate nerve boundary segmentation technique.

The *Third* contribution is to develop a probabilistic digital atlas of the ten cranial nerve pairs by incorporating a Statistical Shape Model with the 1-Simplex deformable contour model by introducing a SSM-based force. The integration of shape information as *a priori* knowledge results in robust and accurate centerline segmentations from even low-resolution MRI data.



A thorough quantitative validation was performed for the medial axis extraction technique using synthetic and patient MRI data. Also, the surface segmentation method was validated using MRI data against expert ground-truth segmentation. The following conclusions can be inferred from the validation point of view:

- The 1-Simplex deformable model-based segmentation technique can identify nerve centerlines in high-resolution MRI data with an average error of 0.19 mm, thereby ensuring sub-voxel accuracy.
- The surface segmentation approach using 2-Simplex-based refinement shows significant improvement with average 82% spatial overlapping over all the nerves between manual and automatic segmentation.
- The SSM-aware contour model-based segmentation i.e. segmentation using shape priors, improves segmentation accuracy over the segmentation without shape priors, while segmenting even corrupted or low-resolution MRI data.

This proposed method has been applied to identify cranial nerves; however, it can readily be applied to other tubular structures such as blood vessels in MRI data.

## **6.2 Limitations and Future Works**

We make two simplifying assumptions in this work, both of which support the notion of a simple curve to represent the intracranial portion of the central axis of each cranial nerve, which is in part justified by the intracranial focus of this model.

The first simplifying assumption is that each nerve can be idealized as a single curve within the cranium; obviously, this assumption becomes invalid outside the cranium, such as is the case with the trigeminal nerve, and it is apparent that our contour model will need to be

supplemented with a second framework that can describe tree-like anatomical structures, such as tree space models [145].

Second, we make an abstraction for now of the rootlets that terminate some of the nerves. Particularly, nerves XI and XII do not arise from the brainstem as a single nerve fiber, but rather as a collection of several tiny rootlets that gradually coalesce to form the nerve. In the future, this structure can be modeled as a triangle whose base coincides with the length along the brainstem that spans the rootlet terminations of a given nerve and whose height models their point of convergence.

Moreover, we plan to develop and integrate digital atlases of the cranium and foramina as well as brainstem [146], to automate the estimation of attachment and exit points. The development of these digital atlases is underway. The basic idea is encapsulated in the clothesline metaphor: if one knows the position of the two poles of the clothesline, and its typical tortuosity, one can estimate its path.

The work closest to ours is the Diffusion Tensor MRI (DT-MRI) tractography applied to cranial nerves [147]; however, there is a far larger preponderance of  $T_2$ -weighted imaging in the clinical imaging community than diffusion imaging, particularly at the base of the brain. Moreover, the proposed algorithm can and will be extended to DT-MRI. We will integrate a blood vessel model while ensuring that combined nerve and blood vessel models do not overlap spatially, which motivated our choice of an explicit contour model.

The accuracy of an SSM is dependent on the size of the training dataset utilized to construct the SSM. In this work, we had a limited number of dataset for training and testing shape models. The performance of the SSMs can be further improved by increasing the size of training datasets which allow the SSMs to capture a wide range of variations within the training

population. Along with the SSM-based centerline models, SSM-based radius incorporation might further improve the results of 3D nerve surface segmentation.

Finally, this research will also be extended to identifying and modeling the nerves of the spine, of the peripheral nervous system, and of the enteric nervous system, once the fusion with tree shape analysis is achieved. The combination of 3D contour model and SSM is broadly usable, which will lead to a variety of neurological applications of this digital atlas methodology, particularly given the interest in therapeutic nerve stimulation.

## REFERENCES

- [1] Cancer.org. (2014). *Cancer Facts and Figures* Available: <http://www.cancer.org/research/cancerfactsstatistics/cancerfactsfigures2014/>
- [2] R. A. Patchell, "The management of brain metastases," *Cancer treatment reviews*, vol. 29, pp. 533-540, 2003.
- [3] CBTRUS. (2015). *Central Brain Tumor Registry of the United States*. Available: <http://www.cbtrus.org/factsheet/factsheet.html>
- [4] M. Samii and V. M. Gerganov, "Surgery of Extra-Axial Tumors of the Cerebral Base," *Neurosurgery*, vol. 62, pp. SHC1153-SHC1168, 2008.
- [5] A. Borges and J. Casselman, "Imaging the cranial nerves: Part I: Methodology, infectious and inflammatory, traumatic and congenital lesions," *European radiology*, vol. 17, pp. 2112-2125, 2007.
- [6] K. Vonck, V. De Herdt, and P. Boon, "Vagal nerve stimulation—A 15-year survey of an established treatment modality in epilepsy surgery," in *Advances and technical standards in neurosurgery*, ed: Springer, 2009, pp. 111-146.
- [7] M. Sindou, J. Leston, C. Le Guerinel, and Y. Keravel, "[Treatment of trigeminal neuralgia with microvascular decompression]," *Neuro-chirurgie*, vol. 55, pp. 185-196, 2009.
- [8] R. M. Stuart and C. J. Winfree, "Neurostimulation techniques for painful peripheral nerve disorders," *Neurosurgery Clinics of North America*, vol. 20, pp. 111-120, 2009.
- [9] E. Britannica. *Cranial Nerve*. Available: <http://www.britannica.com/>
- [10] J. Siegfried. (2014). *Microsurgical Decompression of Trigeminal Neuralgia*. Available: <http://www.brain-surgery.com/microsurgical-decompression-of-trigeminal-neuralgia/>
- [11] G. Antoniadis, T. Kretschmer, M. T. Pedro, R. W. König, C. P. Heinen, and H.-P. Richter, "Iatrogenic Nerve Injuries: Prevalence, Diagnosis and Treatment," *Deutsches Ärzteblatt International*, vol. 111, p. 273, 2014.
- [12] K. Adachi, T. Kawase, K. Yoshida, T. Yazaki, and S. Onozuka, "ABC Surgical Risk Scale for skull base meningioma: a new scoring system for predicting the extent of tumor removal and neurological outcome: Clinical article," *Journal of neurosurgery*, vol. 111, pp. 1053-1061, 2009.
- [13] A. Dubey, W.-S. Sung, M. Shaya, R. Patwardhan, B. Willis, D. Smith, *et al.*, "Complications of posterior cranial fossa surgery—an institutional experience of 500 patients," *Surgical neurology*, vol. 72, pp. 369-375, 2009.

- [14] P. J. Jannetta, M. R. McLaughlin, F. Raymond, J. Sekula, and P. Jannetta, "Microvascular decompression," *Trigeminal Neuralgia*, vol. 1, pp. 192-213, 2010.
- [15] P. R. L. Leal, M. Hermier, J. C. Froment, M. A. Souza, G. Cristino-Filho, and M. Sindou, "Preoperative demonstration of the neurovascular compression characteristics with special emphasis on the degree of compression, using high-resolution magnetic resonance imaging: a prospective study, with comparison to surgical findings, in 100 consecutive patients who underwent microvascular decompression for trigeminal neuralgia," *Acta neurochirurgica*, vol. 152, pp. 817-825, 2010.
- [16] G. Cruccu, T. Aziz, L. Garcia-Larrea, P. Hansson, T. Jensen, J. P. Lefaucheur, *et al.*, "Neurostimulation Therapy for Neuropathic Pain," *European Handbook of Neurological Management, Volume 2, Second Edition*, pp. 11-29, 2012.
- [17] K. V. Slavin, S. Al-Nafi, and S. Y. Rasskazoff, "Peripheral Nerve Stimulation in Pain of the Body and Extremities," *Neurostimulation: Principles and Practice*, pp. 210-218, 2013.
- [18] S. Eljamel and K. Slavin, *Neurostimulation: Principles and Practice*: John Wiley & Sons, 2013.
- [19] H.-P. Schlake, R. H. Goldbrunner, C. Milewski, J. Krauss, H. Trautner, R. Behr, *et al.*, "Intra-operative electromyographic monitoring of the lower cranial motor nerves (LCN IX–XII) in skull base surgery," *Clinical neurology and neurosurgery*, vol. 103, pp. 72-82, 2001.
- [20] M. Kawaguchi, H. Ohnishi, T. Sakamoto, K. Shimizu, H. Touho, T. Monobe, *et al.*, "Intraoperative electrophysiologic monitoring of cranial motor nerves in skull base surgery," *Surgical neurology*, vol. 43, pp. 177-181, 1995.
- [21] A. S. Youssef and A. E. Downes, "Intraoperative neurophysiological monitoring in vestibular schwannoma surgery: advances and clinical implications," *Neurosurgical focus*, vol. 27, p. E9, 2009.
- [22] S. Delorme, D. Laroche, R. DiRaddo, and R. F. Del Maestro, "NeuroTouch: a physics-based virtual simulator for cranial microneurosurgery training," *Neurosurgery*, vol. 71, pp. ons32-ons42, 2012.
- [23] B. Fischl, D. H. Salat, E. Busa, M. Albert, M. Dieterich, C. Haselgrove, *et al.*, "Whole brain segmentation: automated labeling of neuroanatomical structures in the human brain," *Neuron*, vol. 33, pp. 341-355, 2002.
- [24] K. A. Ganser, H. Dickhaus, R. Metzner, and C. R. Wirtz, "A deformable digital brain atlas system according to Talairach and Tournoux," *Medical Image Analysis*, vol. 8, pp. 3-22, 2004.

- [25] R. Kikinis, M. E. Shenton, D. V. Iosifescu, R. W. McCarley, P. Saiviroonporn, H. H. Hokama, *et al.*, "A digital brain atlas for surgical planning, model-driven segmentation, and teaching," *Visualization and Computer Graphics, IEEE Transactions on*, vol. 2, pp. 232-241, 1996.
- [26] W. L. Nowinski, A. Johnson, B. C. Chua, and N. G. Nowinska, "Three-dimensional interactive and stereotactic atlas of the cranial nerves and their nuclei correlated with surface neuroanatomy, vasculature and magnetic resonance imaging," *Journal of neuroscience methods*, vol. 206, pp. 205-216, 2012.
- [27] W. L. Nowinski, *The Human Brain in 1969 Pieces: Structure, Vasculature, Tracts, Cranial Nerves, and Systems; Explore the Universe of Neuroanatomy!*: Thieme, 2012.
- [28] W. Nowinski, B. Chua, G. Qian, and N. Nowinska, "The human brain in 1700 pieces: Design and development of a three-dimensional, interactive and reference atlas," *Journal of neuroscience methods*, vol. 204, pp. 44-60, 2012.
- [29] H. Delingette, "General object reconstruction based on simplex meshes," *International Journal of Computer Vision*, vol. 32, pp. 111-146, 1999.
- [30] J. A. Sethian, *Level set methods and fast marching methods: evolving interfaces in computational geometry, fluid mechanics, computer vision, and materials science* vol. 3: Cambridge university press, 1999.
- [31] J. A. Sethian, "A fast marching level set method for monotonically advancing fronts," *Proceedings of the National Academy of Sciences*, vol. 93, pp. 1591-1595, 1996.
- [32] G. Behiels, F. Maes, D. Vandermeulen, and P. Suetens, "Evaluation of image features and search strategies for segmentation of bone structures in radiographs using active shape models," *Medical Image Analysis*, vol. 6, pp. 47-62, 2002.
- [33] D. Purves, G. J. Augustine, D. Fitzpatrick, L. C. Katz, A.-S. LaMantia, J. O. McNamara, *et al.*, "The auditory system," 2001.
- [34] R. Drake, A. W. Vogl, and A. W. Mitchell, *Gray's anatomy for students*: Elsevier Health Sciences, 2009.
- [35] K. D. Toennies, "Guide to Medical Image Analysis," 2012.
- [36] J. Kiernan and R. Rajakumar, *Barr's The human nervous system: an anatomical viewpoint*: Lippincott Williams & Wilkins, 2013.
- [37] Imaios. <http://www.imaios.com/en/e-Courses/e-MRI/NMR>.

- [38] J. Casselman, K. Mermuys, J. Delanote, J. Ghekiere, and K. Coenegrachts, "MRI of the cranial nerves—more than meets the eye: technical considerations and advanced anatomy," *Neuroimaging Clinics of North America*, vol. 18, pp. 197-231, 2008.
- [39] F. J. Laine and W. Smoker, "Anatomy of the cranial nerves," *Neuroimaging clinics of North America*, vol. 8, pp. 69-100, 1998.
- [40] A. Borges and J. Casselman, "Imaging the cranial nerves: part II: primary and secondary neoplastic conditions and neurovascular conflicts," *European radiology*, vol. 17, pp. 2332-2344, 2007.
- [41] B. Hargreaves, "Rapid gradient-echo imaging," *Journal of Magnetic Resonance Imaging*, vol. 36, pp. 1300-1313, 2012.
- [42] H. Aydın, E. Altın, A. Dilli, S. Sipahioğlu, and B. Hekimoğlu, "Evaluation of jugular foramen nerves by using b-FFE, T2-weighted DRIVE, T2-weighted FSE and post-contrast T1-weighted MRI sequences," *Diagn Interv Radiol*, vol. 17, pp. 3-9, 2011.
- [43] K. Tsuchiya, C. Aoki, and J. Hachiya, "Evaluation of MR cisternography of the cerebellopontine angle using a balanced fast-field-echo sequence: preliminary findings," *European radiology*, vol. 14, pp. 239-242, 2004.
- [44] I. Yousry, S. Camelio, U. Schmid, M. Horsfield, M. Wiesmann, H. Brückmann, *et al.*, "Visualization of cranial nerves I–XII: value of 3D CISS and T2-weighted FSE sequences," *European radiology*, vol. 10, pp. 1061-1067, 2000.
- [45] H. G. Hatipoğlu, T. Durakoğlugil, D. Ciliz, and E. Yüksel, "Comparison of FSE T2W and 3D FIESTA sequences in the evaluation of posterior fossa cranial nerves with MR cisternography," *Diagn Interv Radiol*, vol. 13, pp. 56-60, 2007.
- [46] T. Mikami, Y. Minamida, T. Yamaki, I. Koyanagi, T. Nonaka, and K. Houkin, "Cranial nerve assessment in posterior fossa tumors with fast imaging employing steady-state acquisition (FIESTA)," *Neurosurgical review*, vol. 28, pp. 261-266, 2005.
- [47] Y. Okumura, M. Suzuki, A. Takemura, H. Tsujii, K. Kawahara, Y. Matsuura, *et al.*, "[Visualization of the lower cranial nerves by 3D-FIESTA]," *Nihon Hoshasen Gijutsu Gakkai zasshi*, vol. 61, pp. 291-297, 2005.
- [48] S. Sheth, B. F. Branstetter IV, and E. J. Escott, "Appearance of Normal Cranial Nerves on Steady-State Free Precession MR Images 1," *Radiographics*, vol. 29, pp. 1045-1055, 2009.
- [49] M. Hodaie, J. Quan, and D. Q. Chen, "In Vivo Visualization of Cranial Nerve Pathways in Humans Using Diffusion-Based Tractography," *Neurosurgery*, vol. 66, pp. 788-796, 2010.

- [50] V. J. Wedeen, R. Wang, J. D. Schmahmann, T. Benner, W. Tseng, G. Dai, *et al.*, "Diffusion spectrum magnetic resonance imaging (DSI) tractography of crossing fibers," *Neuroimage*, vol. 41, pp. 1267-1277, 2008.
- [51] D. S. Tuch, T. G. Reese, M. R. Wiegell, N. Makris, J. W. Belliveau, and V. J. Wedeen, "High angular resolution diffusion imaging reveals intravoxel white matter fiber heterogeneity," *Magnetic Resonance in Medicine*, vol. 48, pp. 577-582, 2002.
- [52] H. Kabasawa, Y. Masutani, S. Aoki, O. Abe, T. Masumoto, N. Hayashi, *et al.*, "3T PROPELLER diffusion tensor fiber tractography: a feasibility study for cranial nerve fiber tracking," *Radiation medicine*, vol. 25, pp. 462-466, 2007.
- [53] M. Kass, A. Witkin, and D. Terzopoulos, "Snakes: Active contour models," *International journal of computer vision*, vol. 1, pp. 321-331, 1988.
- [54] D. Terzopoulos, J. Platt, A. Barr, and K. Fleischer, "Elastically deformable models," in *ACM Siggraph Computer Graphics*, 1987, pp. 205-214.
- [55] J. Montagnat, H. Delingette, and N. Ayache, "A review of deformable surfaces: topology, geometry and deformation," *Image and vision computing*, vol. 19, pp. 1023-1040, 2001.
- [56] T. McInerney and D. Terzopoulos, "Deformable models in medical image analysis: a survey," *Medical image analysis*, vol. 1, pp. 91-108, 1996.
- [57] C. Xu, D. L. Pham, and J. L. Prince, "Image segmentation using deformable models," *Handbook of medical imaging*, vol. 2, pp. 129-174, 2000.
- [58] T. McInerney and D. Terzopoulos, "T-snakes: Topology adaptive snakes," *Medical image analysis*, vol. 4, pp. 73-91, 2000.
- [59] J. Mille, R. Boné, and L. D. Cohen, "Region-based 2D deformable generalized cylinder for narrow structures segmentation," in *Computer Vision—ECCV 2008*, ed: Springer, 2008, pp. 392-404.
- [60] S. Osher and N. Paragios, *Geometric level set methods in imaging, vision, and graphics*: Springer, 2003.
- [61] E. Angelini, Y. Jin, and A. Laine, "State of the art of level set methods in segmentation and registration of medical imaging modalities," in *Handbook of Biomedical Image Analysis*, ed: Springer, 2005, pp. 47-101.
- [62] F. K. Quek and C. Kirbas, "Vessel extraction in medical images by wave-propagation and traceback," *Medical Imaging, IEEE Transactions on*, vol. 20, pp. 117-131, 2001.



- [63] T. Deschamps and L. D. Cohen, "Fast extraction of tubular and tree 3D surfaces with front propagation methods," in *Pattern Recognition, 2002. Proceedings. 16th International Conference on*, 2002, pp. 731-734.
- [64] J.-Y. Park, T. McInerney, D. Terzopoulos, and M.-H. Kim, "A non-self-intersecting adaptive deformable surface for complex boundary extraction from volumetric images," *Computers & Graphics*, vol. 25, pp. 421-440, 2001.
- [65] J. Lötjönen and T. Mäkelä, "Segmentation of MR images using deformable models: Application to cardiac images," *International Journal of Bioelectromagnetism*, vol. 3, pp. 37-45, 2001.
- [66] M. Vasilescu and D. Terzopoulos, "Adaptive meshes and shells," in *IEEE Conference on Computer Vision and Pattern Recognition*, 1992, pp. 829-832.
- [67] J. Montagnat and H. Delingette, "4D deformable models with temporal constraints: application to 4D cardiac image segmentation," *Medical Image Analysis*, vol. 9, pp. 87-100, 2005.
- [68] B. Gilles and N. Magnenat-Thalmann, "Musculoskeletal MRI segmentation using multi-resolution simplex meshes with medial representations," *Medical image analysis*, vol. 14, pp. 291-302, 2010.
- [69] Y. Sato, S. Nakajima, N. Shiraga, H. Atsumi, S. Yoshida, T. Koller, *et al.*, "Three-dimensional multi-scale line filter for segmentation and visualization of curvilinear structures in medical images," *Medical image analysis*, vol. 2, pp. 143-168, 1998.
- [70] A. F. Frangi, W. J. Niessen, K. L. Vincken, and M. A. Viergever, "Multiscale vessel enhancement filtering," in *Medical Image Computing and Computer-Assisted Intervention—MICCAI'98*, ed: Springer, 1998, pp. 130-137.
- [71] A. F. Frangi, W. J. Niessen, R. M. Hoogeveen, T. Van Walsum, and M. A. Viergever, "Model-based quantitation of 3-D magnetic resonance angiographic images," *Medical Imaging, IEEE Transactions on*, vol. 18, pp. 946-956, 1999.
- [72] K. Krissian, G. Malandain, N. Ayache, R. Vaillant, and Y. Troussset, "Model-based detection of tubular structures in 3D images," *Computer vision and image understanding*, vol. 80, pp. 130-171, 2000.
- [73] O. Wink, W. J. Niessen, and M. A. Viergever, "Multiscale vessel tracking," *Medical Imaging, IEEE Transactions on*, vol. 23, pp. 130-133, 2004.
- [74] H. Shikata, E. A. Hoffman, and M. Sonka, "Automated segmentation of pulmonary vascular tree from 3D CT images," *Medical Imaging 2004: Physiology, Function, and Structure from Medical Images*, vol. 5369, pp. 107-116, 2004.

- [75] M. Descoteaux, "High angular resolution diffusion MRI: from local estimation to segmentation and tractography," Max Planck Institute, Germany, 2010.
- [76] S. R. Aylward and E. Bullitt, "Initialization, noise, singularities, and scale in height ridge traversal for tubular object centerline extraction," *Medical Imaging, IEEE Transactions on*, vol. 21, pp. 61-75, 2002.
- [77] E. W. Dijkstra, "A note on two problems in connexion with graphs," *Numerische mathematik*, vol. 1, pp. 269-271, 1959.
- [78] M. Gulsun and H. Tek, "3d construction of coronary arteries," in *International Workshop on Computer Vision for Intravascular and Intracardiac Imaging, MICCAI*, 2006.
- [79] J. H. Noble and B. M. Dawant, "An atlas-navigated optimal medial axis and deformable model algorithm (NOMAD) for the segmentation of the optic nerves and chiasm in MR and CT images," *Medical image analysis*, vol. 15, pp. 877-884, 2011.
- [80] T. Deschamps and L. D. Cohen, "Fast extraction of minimal paths in 3D images and applications to virtual endoscopy," *Medical image analysis*, vol. 5, pp. 281-299, 2001.
- [81] L. D. Cohen and R. Kimmel, "Global minimum for active contour models: A minimal path approach," *International journal of computer vision*, vol. 24, pp. 57-78, 1997.
- [82] H. Li and A. Yezzi, "Vessels as 4-D curves: Global minimal 4-D paths to extract 3-D tubular surfaces and centerlines," *Medical Imaging, IEEE Transactions on*, vol. 26, pp. 1213-1223, 2007.
- [83] F. Benmansour and L. D. Cohen, "Tubular structure segmentation based on minimal path method and anisotropic enhancement," *International Journal of Computer Vision*, vol. 92, pp. 192-210, 2011.
- [84] M. Gensheimer, A. Cmelak, K. Niermann, and B. M. Dawant, "Automatic delineation of the optic nerves and chiasm on CT images," in *Medical Imaging*, 2007, pp. 651216-651216-10.
- [85] V. Fortunati, R. F. Verhaart, F. van der Lijn, W. J. Niessen, J. F. Veenland, M. M. Paulides, *et al.*, "Tissue segmentation of head and neck CT images for treatment planning: A multiatlas approach combined with intensity modeling," *Medical physics*, vol. 40, p. 071905, 2013.
- [86] G. Bekes, E. Máté, L. G. Nyúl, A. Kuba, and M. Fidrich, "Geometrical model-based segmentation of the organs of sight on CT images," *Medical physics*, vol. 35, pp. 735-743, 2008.

- [87] S. Panda, A. J. Asman, M. P. DeLisi, L. A. Mawn, R. L. Galloway, and B. A. Landman, "Robust optic nerve segmentation on clinically acquired CT," in *SPIE Medical Imaging*, 2014, pp. 90341G-90341G-10.
- [88] M. Descoteaux and C. Poupon, "Diffusion-weighted MRI," *Comprehensive Biomedical Physics. Elsevier*, vol. 2, p. 3, 2012.
- [89] P. J. Basser, J. Mattiello, and D. LeBihan, "Estimation of the Effective Self-Diffusion Tensor from the NMR Spin Echo," *Journal of Magnetic Resonance, Series B*, vol. 103, pp. 247-254, 1994.
- [90] C. Pierpaoli and P. J. Basser, "Toward a quantitative assessment of diffusion anisotropy," *Magnetic resonance in medicine*, vol. 36, pp. 893-906, 1996.
- [91] V. Wedeen, T. Reese, D. Tuch, M. Weigel, J. Dou, R. Weiskoff, *et al.*, "Mapping fiber orientation spectra in cerebral white matter with Fourier-transform diffusion MRI," in *Proceedings of the 8th Annual Meeting of ISMRM, Denver*, 2000, p. 82.
- [92] D. S. Tuch, "Diffusion MRI of complex tissue structure," Citeseer, 2002.
- [93] M. Descoteaux, R. Deriche, D. Le Bihan, J.-F. Mangin, and C. Poupon, "Multiple q-shell diffusion propagator imaging," *Medical image analysis*, vol. 15, pp. 603-621, 2011.
- [94] M. B. Stegmann and D. D. Gomez, "A brief introduction to statistical shape analysis," *Informatics and Mathematical Modelling, Technical University of Denmark, DTU*, vol. 15, 2002.
- [95] T. F. Cootes, C. J. Taylor, D. H. Cooper, and J. Graham, "Active shape models-their training and application," *Computer vision and image understanding*, vol. 61, pp. 38-59, 1995.
- [96] T. F. Cootes, G. J. Edwards, and C. J. Taylor, "Active appearance models," *IEEE Transactions on pattern analysis and machine intelligence*, vol. 23, pp. 681-685, 2001.
- [97] D. Cremers, T. Kohlberger, and C. Schnörr, "Shape statistics in kernel space for variational image segmentation," *Pattern Recognition*, vol. 36, pp. 1929-1943, 2003.
- [98] T. Heimann and H.-P. Meinzer, "Statistical shape models for 3D medical image segmentation: A review," *Medical image analysis*, vol. 13, pp. 543-563, 2009.
- [99] D. Nain, A. Yezzi, and G. Turk, "Vessel segmentation using a shape driven flow," in *Medical Image Computing and Computer-Assisted Intervention—MICCAI 2004*, ed: Springer, 2004, pp. 51-59.

- [100] C. Tejos, P. Irarrazaval, and A. Cárdenas-Blanco, "Simplex mesh diffusion snakes: integrating 2D and 3D deformable models and statistical shape knowledge in a variational framework," *International journal of computer vision*, vol. 85, pp. 19-34, 2009.
- [101] J. Schmid, J. Kim, and N. Magnenat-Thalmann, "Robust statistical shape models for MRI bone segmentation in presence of small field of view," *Medical image analysis*, vol. 15, pp. 155-168, 2011.
- [102] T. F. Cootes, C. J. Taylor, D. H. Cooper, and J. Graham, "Training models of shape from sets of examples," in *BMVC92*, ed: Springer, 1992, pp. 9-18.
- [103] S. M. Pizer, P. T. Fletcher, S. Joshi, A. Thall, J. Z. Chen, Y. Fridman, *et al.*, "Deformable m-reps for 3D medical image segmentation," *International Journal of Computer Vision*, vol. 55, pp. 85-106, 2003.
- [104] P. A. Yushkevich, H. Zhang, and J. C. Gee, "Continuous medial representation for anatomical structures," *Medical Imaging, IEEE Transactions on*, vol. 25, pp. 1547-1564, 2006.
- [105] J. C. Gower, "Generalized procrustes analysis," *Psychometrika*, vol. 40, pp. 33-51, 1975.
- [106] M. A. Audette, F. P. Ferrie, and T. M. Peters, "An algorithmic overview of surface registration techniques for medical imaging," *Medical Image Analysis*, vol. 4, pp. 201-217, 2000.
- [107] F. L. Bookstein, "Principal warps: Thin-plate splines and the decomposition of deformations," *IEEE Transactions on pattern analysis and machine intelligence*, vol. 11, pp. 567-585, 1989.
- [108] P. Dierckx, "On calculating normalized Powell-Sabin B-splines," *Computer Aided Geometric Design*, vol. 15, pp. 61-78, 1997.
- [109] W. R. Crum, T. Hartkens, and D. Hill, "Non-rigid image registration: theory and practice," 2014.
- [110] P. J. Besl and N. D. McKay, "Method for registration of 3-D shapes," in *Robotics-DL tentative*, 1992, pp. 586-606.
- [111] J. M. Balter, C. A. Pelizzari, and G. T. Chen, "Correlation of projection radiographs in radiation therapy using open curve segments and points," *Medical physics*, vol. 19, pp. 329-334, 1992.
- [112] P. Wen, "Medical image registration based-on points, contour and curves," in *BioMedical Engineering and Informatics, 2008. BMEI 2008. International Conference on*, 2008, pp. 132-136.

- [113] G. Subsol, N. Roberts, M. Doran, J.-P. Thirion, and G. H. Whitehouse, "Automatic analysis of cerebral atrophy," *Magnetic resonance imaging*, vol. 15, pp. 917-927, 1997.
- [114] N. Ayache, A. P. Gueziec, J.-P. Thirion, A. Gourdon, and J. Knoploch, "Evaluating 3D registration of CT-scan images using crest lines," in *SPIE's 1993 International Symposium on Optics, Imaging, and Instrumentation*, 1993, pp. 60-71.
- [115] J. P. Pluim, J. A. Maintz, and M. A. Viergever, "Mutual-information-based registration of medical images: a survey," *Medical Imaging, IEEE Transactions on*, vol. 22, pp. 986-1004, 2003.
- [116] W. H. Press, S. A. Teukolsky, W. T. Vetterling, and B. P. Flannery, "Numerical Recipes in C+," 2002.
- [117] A. Sotiras, C. Davatzikos, and N. Paragios, "Deformable medical image registration: A survey," *Medical Imaging, IEEE Transactions on*, vol. 32, pp. 1153-1190, 2013.
- [118] D. Rueckert, L. I. Sonoda, C. Hayes, D. L. Hill, M. O. Leach, and D. J. Hawkes, "Non-rigid registration using free-form deformations: application to breast MR images," *Medical Imaging, IEEE Transactions on*, vol. 18, pp. 712-721, 1999.
- [119] J. Wang and T. Jiang, "Non-rigid registration of brain MRI using NURBS," *Pattern Recognition Letters*, vol. 28, pp. 214-223, 2007.
- [120] S. K. Balci, P. Golland, M. Shenton, and W. M. Wells, "Free-form B-spline deformation model for groupwise registration," in *Medical image computing and computer-assisted intervention: MICCAI... International Conference on Medical Image Computing and Computer-Assisted Intervention*, 2007, p. 23.
- [121] S. Liao, H. Jia, G. Wu, D. Shen, and A. s. D. N. Initiative, "A novel framework for longitudinal atlas construction with groupwise registration of subject image sequences," *Neuroimage*, vol. 59, pp. 1275-1289, 2012.
- [122] S. Purwani, T. Cootes, and C. Twining, "Ensemble registration: Combining groupwise registration and segmentation," 2014.
- [123] S. R. Aylward, J. Jomier, S. Weeks, and E. Bullitt, "Registration and analysis of vascular images," *International Journal of Computer Vision*, vol. 55, pp. 123-138, 2003.
- [124] J. Jomier and S. R. Aylward, "Rigid and deformable vasculature-to-image registration: A hierarchical approach," in *Medical Image Computing and Computer-Assisted Intervention—MICCAI 2004*, ed: Springer, 2004, pp. 829-836.
- [125] B. Gilles, "Anatomical and kinematical modelling of the musculoskeletal system from MRI," PhD, Faculty of sciences, University of Geneva, 2007.

- [126] F. Litvin, *Gear Geometry and Applied Theory*. University of Illinois, Chicago. PTR Prentice Hall, Englewood Cliffs, New Jersey 0763: ISBN-13-211095-4, 1994.
- [127] N. W. Frangi AF, Hoogeveen RM, van Walsum T, Viergever MA., "Model-based quantitation of 3-D magnetic resonance angiographic images," *IEEE Trans Med Imaging*, vol. 18(10), pp. 946-56, 1999 Oct.
- [128] O. Van Kaick, H. Zhang, G. Hamarneh, and D. Cohen-Or, "A survey on shape correspondence," in *Computer Graphics Forum*, 2011, pp. 1681-1707.
- [129] C. Brechbühler, G. Gerig, and O. Kübler, "Parametrization of closed surfaces for 3-D shape description," *Computer vision and image understanding*, vol. 61, pp. 154-170, 1995.
- [130] L. Shen and F. Makedon, "Spherical mapping for processing of 3D closed surfaces," *Image and vision computing*, vol. 24, pp. 743-761, 2006.
- [131] R. H. Davies, C. J. Twining, T. F. Cootes, J. C. Waterton, and C. J. Taylor, "A minimum description length approach to statistical shape modeling," *IEEE Transactions on Medical Imaging*, vol. 21, pp. 525-537, 2002.
- [132] M. D. Meyer, P. Georgel, and R. T. Whitaker, "Robust particle systems for curvature dependent sampling of implicit surfaces," in *International Conference on Shape Modeling and Applications 2005 (SMI'05)*, 2005, pp. 124-133.
- [133] A. P. Witkin and P. S. Heckbert, "Using particles to sample and control implicit surfaces," in *Proceedings of the 21st annual conference on Computer graphics and interactive techniques*, 1994, pp. 269-277.
- [134] J. Cates, P. T. Fletcher, M. Styner, M. Shenton, and R. Whitaker, "Shape modeling and analysis with entropy-based particle systems," in *Biennial International Conference on Information Processing in Medical Imaging*, 2007, pp. 333-345.
- [135] S. Sultana, P. Agrawal, S. Y. Elhabian, R. T. Whitaker, T. Rashid, J. E. Blatt, *et al.*, "Towards a Statistical Shape-Aware Deformable Contour Model for Cranial Nerve Identification," in *Workshop on Clinical Image-Based Procedures*, 2016, pp. 68-76.
- [136] J. Schmid and N. Magnenat-Thalmann, "MRI bone segmentation using deformable models and shape priors," in *International conference on medical image computing and computer-assisted intervention*, 2008, pp. 119-126.
- [137] T. F. Cootes, A. Hill, C. J. Taylor, and J. Haslam, "Use of active shape models for locating structures in medical images," *Image and vision computing*, vol. 12, pp. 355-365, 1994.
- [138] S. Roweis, "Levenberg-marquardt optimization," *Notes, University Of Toronto*, 1996.

- [139] J. Schmid, "Knowledge-based deformable models for medical image analysis," University of Geneva, 2011.
- [140] M. A. Styner, K. T. Rajamani, L.-P. Nolte, G. Zsemlye, G. Székely, C. J. Taylor, *et al.*, "Evaluation of 3D correspondence methods for model building," in *Biennial International Conference on Information Processing in Medical Imaging*, 2003, pp. 63-75.
- [141] B. C. Munsell, P. Dalal, and S. Wang, "Evaluating shape correspondence for statistical shape analysis: A benchmark study," *IEEE Transactions on Pattern Analysis and Machine Intelligence*, vol. 30, pp. 2023-2039, 2008.
- [142] R. H. Davies, C. J. Twining, T. F. Cootes, J. C. Waterton, and C. J. Taylor, "3D statistical shape models using direct optimisation of description length," in *European conference on computer vision*, 2002, pp. 3-20.
- [143] R. H. Davies, *Learning shape: optimal models for analysing natural variability*: University of Manchester, 2002.
- [144] I. Yousry, B. Moriggl, M. Dieterich, T. P. Naidich, U. D. Schmid, and T. A. Yousry, "MR Anatomy of the Proximal Cisternal Segment of the Trochlear Nerve: Neurovascular Relationships and Landmarks 1," *Radiology*, vol. 223, pp. 31-38, 2002.
- [145] A. Feragen, P. Lo, M. de Bruijne, M. Nielsen, and F. Lauze, "Toward a theory of statistical tree-shape analysis," *IEEE transactions on pattern analysis and machine intelligence*, vol. 35, pp. 2008-2021, 2013.
- [146] N. Patel, S. Sultana, and M. A. Audette, "Contour Models for Descriptive Patient-Specific Neuro-Anatomical Modeling: Towards a Digital Brainstem Atlas," in *Recent Advances in Computational Methods and Clinical Applications for Spine Imaging*, ed: Springer, 2015, pp. 199-211.
- [147] D. J. Roundy N, Cetas JS., "Preoperative identification of the facial nerve in patients with large cerebellopontine angle tumors using high-density diffusion tensor imaging," *Journal of neurosurgery* vol. 116(4), pp. 697-702, 2012.

## VITA

SHARMIN SULTANA

Department of Modeling, Simulation and Visualization Engineering  
Old Dominion University  
Norfolk, VA 23529

### Education

**M.Sc.** August 2009, University of Dhaka, Bangladesh

Major: Computer Science and Engineering

**B.Sc.** August 2007, University of Dhaka, Bangladesh

Major: Computer Science and Engineering

### Publications:

- **Sultana, Sharmin**, Jason Blatt, Benjamin Gilles, Tanweer Rashid, and Michel Audette. "MRI-based Medial Axis Extraction and Boundary Segmentation of Cranial Nerves through Discrete Deformable 3D Contour and Surface Models." *IEEE Transactions on Medical Imaging* (2017).
- **Sultana, Sharmin**, Praful Agrawal, Shireen Y. Elhabian, Ross T. Whitaker, Tanweer Rashid, Jason E. Blatt, Justin S. Cetas, and Michel A. Audette. "Towards a Statistical Shape-Aware Deformable Contour Model for Cranial Nerve Identification." In *Workshop on Clinical Image-Based Procedures*, pp. 68-76. Springer International Publishing, 2016.
- Rashid, Tanweer, **Sharmin Sultana**, and Michel A. Audette. "2-manifold surface meshing using dual contouring with tetrahedral decomposition." *Advances in Engineering Software* 102 (2016): 83-96.
- **Sultana, Sharmin**, Jason E. Blatt, Yueh Lee, Matthew Ewend, Justin S. Cetas, Anthony Costa, and Michel A. Audette. "Patient-Specific Cranial Nerve Identification Using a Discrete Deformable Contour Model for Skull Base Neurosurgery Planning and Simulation." In *Workshop on Clinical Image-Based Procedures*, pp. 36-44. Springer International Publishing, 2015.
- **Sultana, Sharmin**, Salma Begum, Nazma Tara, and Ahsan Raja Chowdhury. "Enhanced-DSR: A New Approach to Improve Performance of DSR Algorithm." *International Journal of Computer Science and Information Technology* 2, no. 2 (2010): 113-123.